UNIVERSITY OF CALIFORNIA

Santa Barbara

Three-Dimensional Wafer Bonded Indium Phosphide Photonic Waveguide Devices

A Dissertation submitted in partial satisfaction of the
requirements for the degree Doctor of Philosophy
in Electrical and Computer Engineering

by

Maura Raburn

Committee in charge:
Professor John E. Bowers, Chair
Professor Nadir Dagli
Professor Evelyn L. Hu
Professor Daniel J. Blumenthal

September 2003

The dissertation of Maura Raburn is approved.

Nadir Dagli

Evelyn L. Hu

Daniel J. Blumenthal

John E. Bowers, Committee Chair

June 2003

Three-Dimensional Wafer Bonded Indium Phosphide Photonic Waveguide Devices

by

Maura Raburn

This dissertation is dedicated to

everyone

who provided a spark for

or fanned the flames of

another's

passion

for math and science.

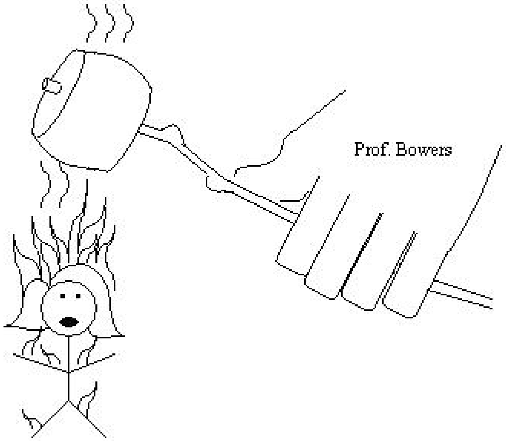

ACKNOWLEDGEMENTS

My years at UCSB have all been very happy ones thanks to the wonderful people I have had the opportunity to work with. I have truly enjoyed being advised by Professor John Bowers and consider myself lucky to have had the opportunity to interact with someone with so much experience both in and out of academia. Having an enthusiastic advisor with a management style so compatible with my work habits has been instrumental to my successes as a graduate student. My discussions with Professor Nadir Dagli provided a plethora of creative ideas, ranging from fine details such as mask layout to the overall direction of my thesis. I am thankful for his endless encouragement and excellent listening skills. My time spent with him complemented my experiences with John very well. Every graduate student should be so lucky as to work closely with more than one professor to gain perspective on her project and career. Professor Evelyn Hu made significant contributions to this thesis with her wealth of knowledge and clever suggestions, and was also an inspiration regarding my future after UCSB. I feel fortunate to have had the opportunity to interact with someone with such a positive outlook. Professor Dan Blumenthal provided me with useful criticism that challenged me to think about my results.

I have spent more time discussing my research with Kohl Gill than anyone else. I have found it a pleasure to explain the minute details of my research to him, and learn about the joys and struggles of work in condensed matter physics in return. His suggestions regarding my research have at times been so creative that I couldn’t tell

whether or not he was kidding, but many of his ideas were true gems. His unusual sense of humor and appetite for bizarre stories also helped me keep my work in perspective.

I am very grateful for my father's strong recommendation of the UCSB Ph.D. program, and his continuing encouragement of my love of math and physics. He has been the single most influential person with respect to my decision to pursue a Ph.D.

My many generous, helpful coworkers at UCSB include Bin Liu, Yae Okuno (who displayed amazing patience with my many marginally reasonable growth requests), Kathi Rauscher, Emily Burmeister, Adrian Keating, Patrick Abraham, Dan Cohen, Kian-Giap Gan, Rohit Grover (actually at U. Md.), Christina Loomis, Cem Ozturk and the rest of the Dagli group, Joachim Piprek, Bob Hill, Peter Allen, Sangyoun Gee, John Barton/Andrew Huntington/Jon Getty/Tal Margalit and the rest of the Coldren group, Neil Barker, Staffan Bjorlin, Alexis Black, Hillary Greenlee, Thomas Liljeberg, Sue Aldemar, Milan Masanovic and the rest of the Blumenthal group, Vickie Edwards,

Andreas Stonas/Elaine Haberer/Sarah Estrada and the rest of the Hu group, Kehl Sink, Raja Jindal, Jonathan Geske, Hsu-Feng Chou, Manish Mehta, Michelle Sinclair, Ali Shakouri, Donato Pasquariello, Valerie De Veyra, Yi-Jen Chiu, Courtney Wagner, Chris Labounty, Vijay Jayaraman, Brian Thibeaut, Adil Karim, Jack Whaley, Daniel Lasaosa, Gehong Zeng, Xiaofeng Fan, and Qi Chen.

My life outside of the lab was greatly enhanced by my experiences with the Santa Barbara Judo Club, Planned Parenthood's educational KCSB radio talk show, the UCSB Physics Circus, Women in Science and Engineering, Girls Inc., the Tri-County

Blood Bank, Women in Physics, and the UCSB Center for Entrepreneurship and Engineering Management. Since this is one of the only opportunities I'll ever have to thank my friends for being such wonderful people in print: I have lead a charmed life over the past several years through the help of many good and evil characters who include Jason Benkoski, Ed Etzkorn, Valerie Anderson, Bev Asoo, Matt Doty, Heather Walling, Regina Cortes, Bree, Dan, and Elizabeth Raburn, Corey Garza, Chris Jones, Lorena Guzman, Dan Rabinowitz, Mike Mattoni, Santosh Smith, Brian Griffin, Steve Hoyt, Kiran Shekar, Gurdit Singh, and my out-of-town landlord who had no idea that he was charging half the going rate for rent in Santa Barbara all 5 years.

CURRICULUM VITA

Maura Raburn
September 2003

EDUCATION

1994-1996	Santa Rosa Junior College A.S. Physics/Engineering
1996-1998	California Institute of Technology B.S. Applied Physics
1998-2000	U.C. Santa Barbara M.S. Electrical and Computer Engineering
2000-2003	U.C. Santa Barbara Ph.D. Electrical and Computer Engineering

PROFESSIONAL EMPLOYMENT

1996, 1997	Hewlett-Packard, Lightwave Technology Division Summer Internship
1997-1998	California Institute of Technology Teaching Assistant, Applied Physics Department
2000	U.C. Santa Barbara Teaching Assistant, Electrical and Computer Engineering Department

AWARDS

1996-1998	Barry Goldwater Fellow, essay topic “Quantum Computing”
1998-2002	U.C. Regents Fellow

PUBLICATIONS

First author journal papers

Raburn, M., Liu, B., Abraham, P., Bowers, J.E. Double-bonded InP-InGaAsP vertical coupler 1:8 beam splitter. IEEE Photonics Technology Letters, vol.12, (no.12), IEEE, Dec. 2000. p.1639-41.

Raburn, M., Liu, B., Okuno, Y., Bowers, J.E. InP-InGaAsP wafer-bonded vertically coupled X-crossing multiple channel optical add-drop multiplexer. IEEE Photonics Technology Letters, vol.13, (no.6), IEEE, June 2001. p.579-81.

Invited Paper

Raburn, M., Bin L., Rauscher, K., Okuno, Y., Dagli, N., Bowers, J.E**.** 3D Photonic Circuit Technology. IEEE Journ. Select. Topics Quant. Elec., vol.8, (no.4), IEEE, July/Aug. 2002 p.935-942.

First author presentations

Raburn, M., Liu, B., Bowers, J.E., Abraham, P., Double fused InP/InGaAsP vertical coupler beam splitter. Integrated Photonics Research. Vol.45. Quebec, Que., Canada, 12-15 July 2000, p.119-21.

Raburn, M.A., Liu, B., Okuno, Y., Bowers, J.E**.,** InP/InGaAsP wafer-bonded vertically coupled X-crossing multiple channel optical add-drop multiplexer. 2001 International Conference on Indium Phosphide and Related Materials. 13th IPRM, Nara, Japan, 14-18 May 2001, p.166-9.

Raburn, M.A., Rauscher, K., Okuno, Y., Dagli, N., Bowers, J.E. Optimization and assessment of Shape, Alignment, and Structure of InP/InGaAsP Waveguide Vertically Coupled Optical Add-Drop Multiplexers. 2002 International Conference on Indium Phosphide and Related Materials. 14th IPRM, Stockholm, Sweden, 12-16 May 2002, p.131-3.

ABSTRACT

Three-Dimensional Wafer Bonded Indium Phosphide Photonic Waveguide Devices

by

Maura Raburn

The development of 3D photonic integrated circuits (PICs) is critical for the optoelectronic IC industry to match the advances of the electronic IC industry. Traditional 2D PICs are limited by substrate size and the number of electrical and optical connections that can be made to the chip. This is a problem for the increasingly dense, complicated circuits developed today. By making the leap to multi-layer interconnects, more compact devices and further creativity in circuit design can be obtained. Also, because different types of devices (lasers, detectors, switches, etc.) are often best made with different materials, methods of integrating different materials onto a single chip must be addressed. 3D routing of signals will be very advantageous for significantly more compact and powerful PICs.

Through wafer bonding, vertically coupled semiconductor waveguide devices provide a means to obtain many of the above desired characteristics. Various novel filtering, add-drop multiplexing, and beam splitting devices of InP/InGaAsP for signals around 1550 nm have been realized.

A three-layer double-bonded waveguide vertical coupler 1:8 beam splitter is demonstrated. The strongly coupled waveguides allow a 580-micron device length, more than one hundred times shorter than that of the equivalent horizontal coupler.

A vertically coupled crossed-waveguide four-channel optical add-drop multiplexer (OADM) has been realized. It is one of the first optical vertically coupled devices with no horizontally coupled counterpart. OADMs of truncated gaussian layout have been fabricated based an investigation of optimal OADM waveguide layout shapes to reduce sidelobe levels and filter bandwidths. These devices illustrate the use of multiple vertical layer optical interconnects for 3D routing of optical signals. The design, processing, and measurement results of these devices are also presented in this dissertation. Wafer bonding is a powerful tool that may provide the future for complex multi-level, multiple material, densely integrated PICs.

TABLE OF CONTENTS

Chapter 1

Why Develop Advanced Photonic Integrated Circuits?

1.1 Electronics versus Photonics

Due to physical properties of electrons and photons, photonic integrated circuits (PICs) are generally superior to electronic ICs for switching data at high bit rates, and transmitting and receiving it over large distances. Optical routing is superior for high-bandwidth, high-density connections, signal propagation integrity, and electromagnetic interaction issues. On-chip photonic interconnects may eradicate the majority of difficulties with clock distribution and input/output connections of large, high-speed chips [1]. If the rapid advances witnessed by the electronic IC industry could be similarly achieved with PICs, it would revolutionize the way information is handled. One may wonder why progress has been slower for optoelectronics.

The semiconductor laser was invented in 1962 [2], but the dawn of the optoelectronics communication era was not until the availability of low-loss fiber in 1979 [3]. By contrast, the bipolar transistor was realized in 1947 [4], the electronic integrated circuit followed in 1958 [5], and development took off rapidly. Electronic IC development had been taking place for over 20 years before optoelectronics began to be widely researched.

The materials used to make photonic and electronic devices have played a role in the progress of the respective fields as well. Silicon, widely used for electronic ICs, is inexpensive and pure relative to other semiconductors [6]. However, it cannot be used for many optoelectronic devices because it has an indirect bandgap. Materials that are suitable for photonic devices at desirable wavelengths (such as GaAs and InP) are much more expensive and less pure than silicon. Thus, material differences have also been a hindrance to the development of PICs.

		Electronic ICs	**Photonic ICs**
Components	**Basic Element**	Simple and similar	Many and complicated
	Dimension	μm×μm	100μm×100μm to cm×cm
	Substrate	One (Si), often can be polycrystalline	≥ One (InP, GaAs, Si, etc.), usually crystalline only
Interconnects	**Coupling Losses**	Low	Can be high
	Connectors	Wires	Waveguides
	Number of 3D Multi-Layer Interconnects	>7 layers	1 (>1 strongly needed)
	Enabling Technology	Thin film technology Flip-chip bonding	None yet (**Wafer bonding**)

Table 1.1 Comparison of electronic and photonic ICs [7].

The nature of routing electrical versus optical signals has also created a bias in favor of electronic ICs (Table 1.1) [7]. In these ICs, electrical signals traverse wires and contacts of metal or other materials with sufficiently low resistivities to allow currents to pass. There are typically no bending loss problems for routing in any direction. The size of the conducting path is usually not critical unless the dimensions are very small or the frequency very high. Wires need only be aligned to the bond pad and can usually contact the chip at any angle that prevents shorting. Moderate surface non-uniformities do not necessarily cause deleterious effects, and the semiconductor can usually be in polycrystalline form, or sputtered on. Isolation is easily achieved with dielectric media.

Optical signals, however, require waveguide dimensions within restrictive boundaries. Otherwise the light will not be guided, or multiple modes traveling at different speeds will result. Optical fibers are usually at least 100μm in width and are difficult to fit to chips in large numbers. They not only need to be placed within a micron of where the light is to be centered, but must also be at the correct angle within a degree relative to the chip to avoid losses. The quality of the interfaces across which light traverses is critical and may require anti-reflection coatings. PIC materials generally must be of crystalline form as well.

Transistors, the basic elements of electronic ICs, are simple and similar. On the other hand, the elements of PICs, such as lasers, detectors, and switches are dissimilar and complex. Typically, only one semiconductor is needed for electronic ICs. Different materials are best used for different optoelectronic components. The laser may require InP for the correct wavelength, the fastest modulator may be of GaAs, and the optimal switch may be a Si product. Thus, means of assembling different materials on to a single chip must be addressed for PICs.

Very large scale integrated (VLSI) circuits are starting to be dominated by interconnects as a result of RC delays from decreasing wire pitch and increasing die size: interconnect delays are increasing concurrent with gate delay decreases. These interconnect delays, as well as chip power consumption and dissipation, chip area, and wiring lengths, are being reduced through 3D integration. The ability to integrate heterogeneous technologies and transistor packing densities are simultaneously being improved with multi-layer interconnections. For example, RC delays are significantly reduced when critical logic gates are placed very close together using multiple active layers. Superior noise performance and lower electromagnetic interference between circuit blocks can be achieved by placing digital, analog, and RF components in mixed-signal systems on separate layers. According to the International Technology Roadmap for Semiconductors, electronic ICs currently have as many as 7 to 8 vertically interconnected layers and will likely have 9 within the decade. The enabling technologies for vertical interconnects, flip-chip bonding and thin-film technology, are well established [8].

Photonic ICs, on the other hand, are still mostly limited to the 2-dimensional regime. There is no well-established enabling technology yet for multi-layer interconnects or assembling different materials on a chip. However, wafer bonding, the assembly without adhesives of clean wafers of various materials and patterning, holds much promise.

1.2 Trends in Integrated Circuit Technology

Electronic IC development is impressive with respect to other advances in related fields. Moore's Law has predicted a doubling in the number of transistors per unit IC area every 18 months since the mid-1960's.

Internet traffic also exhibits phenomenal growth; traffic has been doubling every eight months. This demand for more bandwidth, as well as the omnipresent drive for greater performance and complexity at lower cost, necessitates a similar rapid advancement of PICs capable of routing, adding, and dropping optical signals.

Optoelectronic components, however, suffer from many performance restrictions. 1.55 and 1.3-μm light is used for most data transmission due to properties of optical fiber. The speed and size of optoelectronic devices generally scale with the wavelength of light used, however, restricting further size improvements so long as the wavelength remains fixed.

The complexity of the present-day two-dimensional PICs is also limited by substrate size and the difficulty in connecting large numbers of fibers and electrical connections. By making the leap to multi-layer interconnects, the IC density can be increased greatly. Also, because fewer connections between chips are required, a higher net chip performance and lower losses result. Some devices, such as the ones discussed in this thesis, can actually be made smaller when integrated vertically rather than laterally, further contributing to performance. Smaller chips may allow more chips per wafer. Complete optoelectronic integration of devices of different materials onto a single substrate, rather than separate fiber and wire connections between chips, will achieve a dramatic cost and labor reduction as well. Novel combinations of materials or geometries may allow for devices far superior their in-plane counterparts. Extra creativity in system design, routing, and positioning will be afforded through a shift to 3D architectures. These factors have the potential to revolutionize the way PICs are produced and used.

The devices studied in this thesis address many of these challenges to the development of complex PICs. In particular, the limitation of chip complexity due to multiple fiber connections, substrate size restrictions, and the requirement of multiple materials per chip become much more manageable with wafer bonding technology. This technique for establishing interconnected multiple device layers allows for the chip complexity to extend in the vertical direction, providing much more powerful circuits for a chip of a given size. Wafer bonding is one of the most powerful tools available for combining non-lattice-matched materials while allowing current and light transmission across the material interface. Integrating more devices, especially those of different materials, onto a single chip eliminates the need for bulky fiber connections between those devices.

Most of the drawbacks to 3D PIC technology are becoming more manageable. The extra processing steps required by the wafer bond are a small price to pay for the powerful device creativity it affords. Advancements in IC cooling, heat-sinking, and packaging technology are underway to counterbalance thermal concerns from the higher power densities, greater separation of upper layers from heat sinks, and possible thermal insulation between layers in 3D PICs [9]. Careful placement of devices with high power dissipation will also alleviate thermal problems. Judicious circuit planning will also alleviate coupling between devices on adjacent layers. Reliability concerns from thermo-mechanical and electro-thermal effects between layers, and at layer interfaces, will require investigations of mechanical and thermal behavior of thin films and novel material interfaces [10]. The remaining obstacle to the wide-scale adoption of wafer bonding technology remains device yield. Several techniques for improving bonded area yield to allow larger devices and a higher fraction of successful devices are discussed in this thesis.

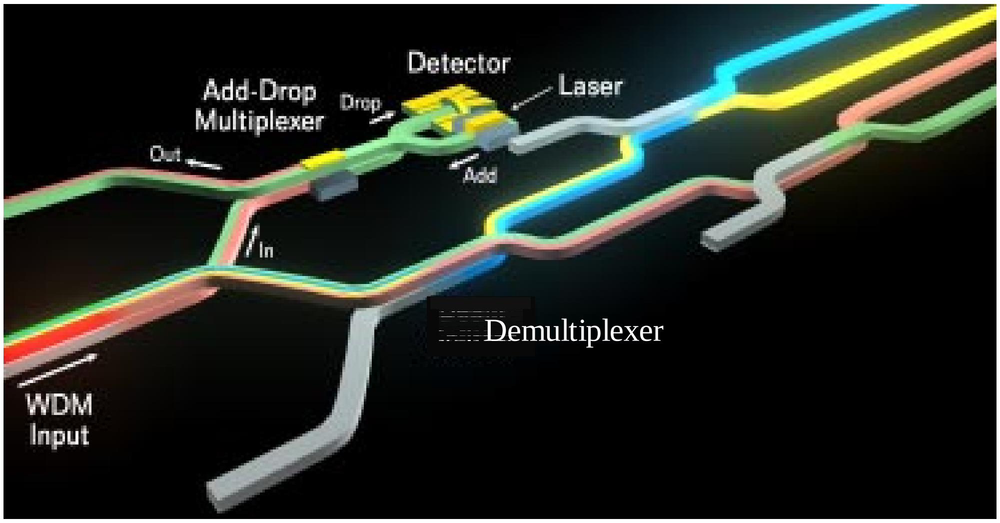

Figure 1.1 Three-dimensional PIC.

A potential three-dimensional PIC is show in Figure 1.1. It consists of multi-layer vertically coupled waveguide wavelength division multiplexed (WDM) routing devices coupled to detectors, lasers, and switches. For example, four channels input from the left side of the figure could be spatially separated into four waveguides on three vertical layers with the 3-layer demultiplexer. Two channels could be split off to an integrated add-drop multiplexer. One channel might be reflected by the grating of the add-drop multiplexer while another might be dropped to an integrated detector and added with an integrated laser. Switches, splitters, and amplifiers can also be integrated in a similar manner. Through vertically coupled PICs, integrated transmission, receiving, add/drop multiplexing, transceiving, and wavelength conversion are possible. This illustrates a possible future of bonded waveguide device technology.

1.3 Waveguide Routing of Light in Three Dimensions

The coupling of light in these waveguide devices is due to waveguide-mode evanescent field overlap. Light entering one waveguide will couple completely to another guide in close proximity if the speeds at which the modes travel in the two guides are matched. The device design and attributes can be very different when the light is coupled vertically rather than horizontally.

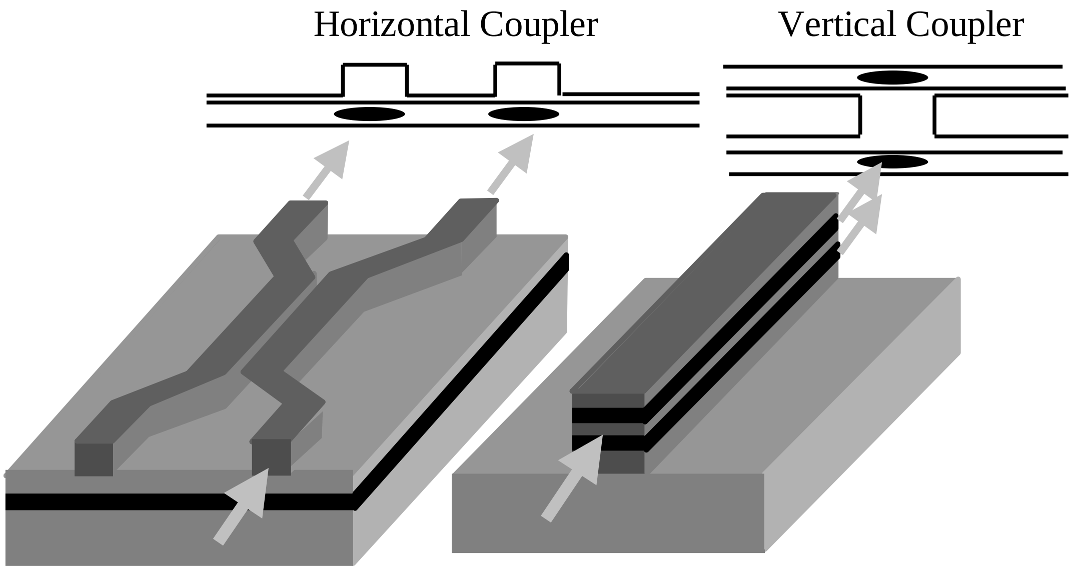

Figure 1.2 Traditional horizontal and vertical couplers [7].

Traditional vertical couplers couple light much more strongly than their horizontally coupled counterparts (Figure 1.2). Because the waveguide separation of vertical couplers is determined by growth thickness, it is much easier to achieve a very narrow, precise waveguide spacing than with horizontal couplers. Also, different materials and dimensions can be used for the top and bottom waveguide cores, allowing the exploitation of material and waveguide dispersion for narrower-bandwidth couplers.

However, because the waveguide cores are separated by growth and are at most a few microns apart, it is very difficult to separate the modes of the two guides. Wafer bonding is used to create vertically coupled waveguides with laterally separated inputs and outputs (Figure 1.3). Wafer bonding also allows the use of non-lattice-matched materials for the top and bottom waveguides, providing further design creativity. We have chosen to pursue vertical couplers in InP because of the ease of integration with other InP devices, such as 1550-nm lasers.

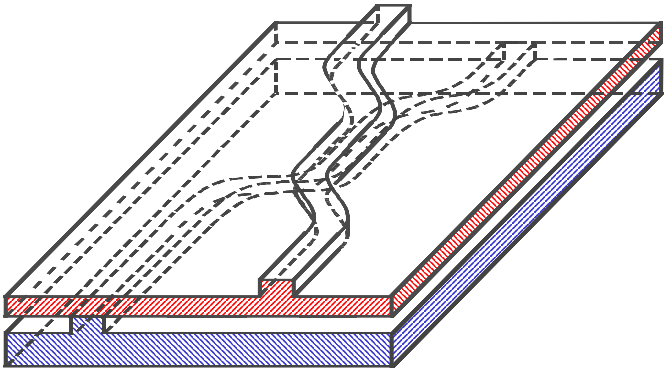

Figure 1.3. Vertical coupler with laterally separated inputs and outputs [7].

1.4 Bonded and 3-D PIC Devices

1.4.1 Noteworthy Bonded Devices

Wafer bonding is the enabling technology for the devices described in this thesis. Many wafer-bonded devices have been developed over the years with functionality and performance that far surpass their non-bonded counterparts.

Vertical-Cavity Surface-Emitting Lasers (VCSELs) have leveraged wafer bonding to combine InP-based active regions with GaAs-based mirrors that provide higher reflectivity and thermal conductivity than InP-based mirrors [11]. This effort had achieved 1550-nm light emission at higher temperatures than previously reported. InGaAs absorption layers have been combined with Si multiplication layers to develop avalanche photodetectors (APDs) with very high quantum efficiencies and the highest gain-bandwidth products ever previously reported [12]. Wafer bonding is also used with micro-electrical mechanical systems (MEMS) devices to allow proper electrical isolation and interconnection of complicated 3D structures that would not be possible without bonding technology [13]. Finally, bonding technology has been used for many years to mass-produce silicon-on-insulator (SOI) substrates for low-power, high-speed complimentary metal-oxide-semiconductor (CMOS) electronics [14].

1.4.2 Other Types of Bonding

There are many techniques for assembling different materials suitable for optoelectronic devices other than the direct-contact wafer bonding employed for this thesis or SOI bonding mentioned above. Polymers can be used as adhesives to allow access to both sides of a semiconductor epitaxial layer [15], and to provide lower-index cladding materials for semiconductor devices. Flip-chip bonding, in which metal or polymer bumps on a chip are connected to bond pads on a substrate, is used for the assembly of the majority of microprocessors. Glass and other optically transparent materials can be used as adhesives through which light propagation can occur. Direct-contact wafer bonding is preferred for 3D optical interconnect development because it is the only one of the above approaches to allow combinations of different semiconductor materials that provide optical and electrical transmission across the interface. Though electrical transmission across the bonded interface was not investigated in this thesis, it has proven successful and been investigated elsewhere [16], and is critical for the success of multi-layer PICs.

1.4.3 Introduction to Multi-Layer Photonic Integrated Circuits

Many types of devices have been developed recently that enable multi-level photonic integration. InP wafer bonding has been used to fabricate vertically coupled micro-disk resonators [17]. Three-dimensional photonic bandgap crystals have been developed from various materials for near-infrared wavelengths that allow routing of light out of the plane of the sample [18]. Slope waveguides are another method for bending light out of the plane of the substrate [19]. Arrays of MEMS mirrors that tilt in many directions have been used to route light in three dimensions [20] [21], and could potentially be used to direct light between devices on multiple levels. In this thesis, near-parallel waveguide couplers are investigated because they provide wide operating bandwidths, minimal waveguide bend losses, straightforward waveguide processing, lower losses than most 3D photonic crystal devices, and guiding of light to reduce diffraction losses.

1.4.4 Previous Three-Dimensional PIC Effort at UCSB

Wafer-bonded vertically coupled waveguide devices were first investigated at UCSB in 1998 [22]. First, straight vertically coupled waveguides with s-bend separated outputs were developed in InP [22]. Then, InP material was bonded out-of-phase to enable push-pull vertically coupled waveguide switches [23]. InP was bonded to GaAs to allow for a greater material dispersion difference for a narrow bandwidth waveguide filter [24]. Next, double-sided processing of waveguide couplers was developed to allow device creation with a single epitaxial growth [25].

Vertical coupler filters were cascaded to create 8-channel wavelength demultiplexers [26]. Finally, straight waveguides that crossed in the form of an “x” were used to make optical add-drop multiplexers (OADMs) [27]. This thesis continues the OADM efforts, and further builds on the endeavors taken above.

1.5 Scope of Thesis

This work is a continuation of the previous wafer-bonded vertically-coupled InP waveguide device effort at UCSB [7]. Specifically, the scaling and performance limits of these devices were investigated. Scaling limitations were examined with respect to number of vertical layers and number of add/drop channels. Performance limitations were examined with respect to optimizations of waveguide coupler shapes.

Various wafer-bonded InP/InGaAsP waveguide devices for 1550-nm light are examined in this thesis. All devices operate through the vertical coupling of light in one waveguide to another nearby waveguide above or below it. To show the potential for multi-layer interconnects of more than 2 levels, a 3-layer 1:8 beam splitter was created (Figure 1.4). To our knowledge, this was the first optical device of more than 2 vertically coupled waveguide layers ever created. To illustrate the possibility for the use of this technology in WDM systems, a 4-channel optical add-drop multiplexer (OADM) was developed (Figure 1.5). This was one of the first vertically coupled waveguide devices with no simple horizontally coupled counterpart ever fabricated. For improvements to OADM device length and performance, devices with more sophisticated waveguide layouts were engineered. Theoretical sidelobe levels of less than –32dB and filter bandwidths over 20% narrower than those of previous devices were possible with certain geometries. Processing non-idealities that exposed the resilience of vertically coupled waveguides to misalignments and vulnerability to incorrect material compositions or thicknesses were studied as well. Devices of different functionality were developed because of the breadth of novel device concepts that had yet to be explored. The field of multi-layer photonic waveguide devices is still in its infancy, and many exciting possibilities abound.

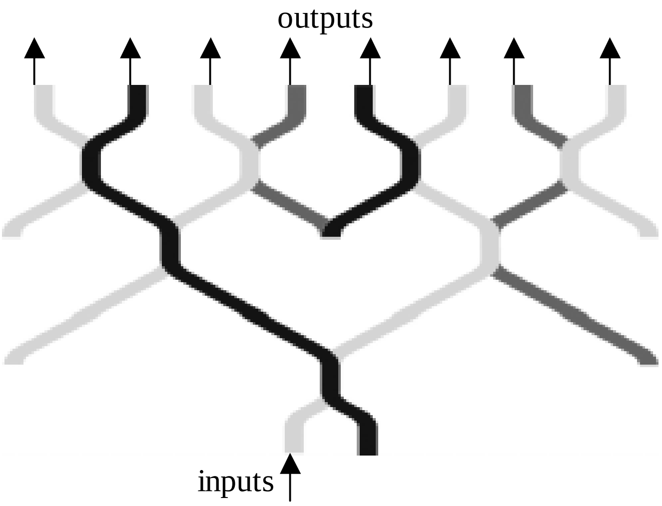

Figure 1.4. Waveguide layout of 3-level 1:8 beam splitter.

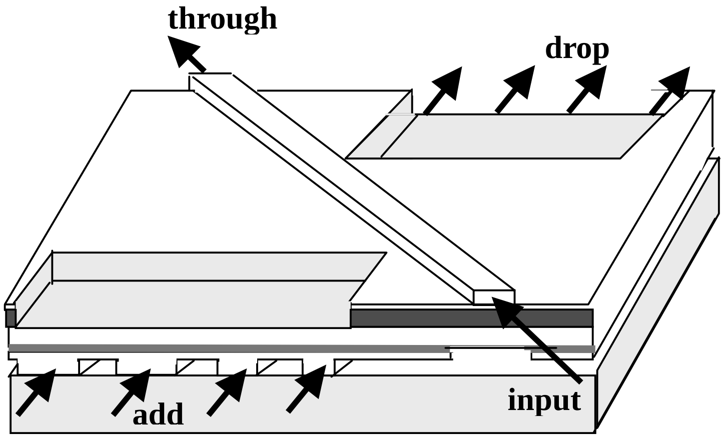

Figure 1.5. 4-channel OADM.

Chapter 2 will introduce the theory required to simulate device performance for device design. The transfer matrix method (TMM) and effective index method (EIM) were combined to quickly calculate waveguide effective index when designing material structure and waveguide widths. The finite difference technique (FDT) and coupled-mode theory (CMT) were used to simulate coupling of light along the length of the device for mask layout. The coupled-mode equation was also integrated to simulate the performance of waveguides of various shapes.

Chapter 3 discusses direct-contact wafer bonding and its advantages over other types of bonding. Over the course of this work, an improvement in bonded area yield from 55% to 95% was observed. The techniques used to achieve this improvement are explained in this chapter. Other bonding problems, such as damage of the host substrate by the bottom waveguides, and their solutions are also covered. The experimental setup is described as well.

Chapter 4 examines the advantages and disadvantages of multi-layer devices. The design and measurement results of the 3-level 1:8 beam splitter are explained in detail.

Chapter 5 covers three types of OADM devices. The behavior of the first device provided the impetus for the creation of the second; likewise, the second device gave rise to the third. The reasons for development, design, and measurement results of the 4-channel OADM, a dual-angle x-crossing OADM, and a gaussian layout OADM are provided. The performance of all devices deviated from the theory to some degree. The differences between experiment and theory are analyzed, and techniques to improve performance are discussed.

Chapter 6 provides a summary and conclusion to this work. The major advantages, such as the novelty allowed by wafer bonding, and disadvantages, such as growth challenges, of this research are discussed. Future device possibilities are also suggested. Recommended future work includes the incorporation of other materials or other types of devices such as micro-resonators and light emitters, detectors, and switches.

References:

[1] J. W. Goodwin, F. J. Leonberger, S. C. Kung, and R. A. Athale, "Optical interconnections for VLSI systems," *Proceedings of the IEEE*, vol. 72, pp. 850-866, 1984.

[2] P. Bhattacharya, *Semiconductor Optoelectronic Devices*, Second ed. Upper Saddle River: Prentice-Hall, 1997.

[3] G. P. Agrawal, *Fiber-Optic Communication Systems*, Second ed. New York: John Wiley & Sons, Inc., 1997.

[4] S. M. Sze, *Physics of Semiconductor Devices*, Second ed. New York: John Wiley & Sons, 1981.

[5] C. Zewe, "'Humble giant' hailed for inventing integrated circuit," *CNN Sci-Tech*, 1997.

[6] D. R. Lide, Dr., *CRC Handbook of Chemistry and Physics*, Third electronic ed. Boca Raton: CRC Press, 2000.

[7] B. Liu, "Three-Dimensional Photonic Devices and Circuits," in *Electrical and Computer Engineering*. Santa Barbara: U. C. Santa Barbara, 2000.

[8] K. Banerjee, S. J. Souri, P. Kapur, and K. C. Saraswat, "3-D ICs: A Novel Chip Design for Improving Deep-Submicrometer Interconnect Performance and Systems-on-Chip Integration," *Proceedings of the IEEE*, vol. 89, pp. 602-633, 2001.

[9] D. B. Tuckerman and R. F. W. Pease, "High-performance heat sinking for VLSI," *IEEE Electronic Device Letters*, vol. EDL-2, pp. 126-129, 1981.

[10] S. Im and K. Banerjee, "Full chip thermal analysis of planar (2-D) and vertically integrated (3-D) high performance ICs," *IEDM Technical Digest*, pp. 727-730, 2000.

[11] J. J. Dudley, D. I. Babic, R. Mirin, L. Yang, B. I. Miller, R. J. Ram, T. Reynolds, E. L. Hu, and J. E. Bowers, "Low threshold, wafer fused long wavelength vertical cavity lasers," *Applied Physics Letters*, vol. 64, pp. 1463-5, 1994.

[12] A. R. Hawkins, W. Weishu, P. Abraham, K. Streubel, and J. E. Bowers, "High gain-bandwidth-product silicon heterointerface photodetector," *Applied Physics Letters*, vol. 70, pp. 303-5, 1997.

[13] Y. Chang-Han and N. W. Cheung, "Fabrication of silicon and oxide membranes over cavities using ion-cut layer transfer," *Journal of Microelectromechanical Systems*, vol. 9, pp. 474-7, 2000.

[14] Q.-Y. Tong and U. M. Gosele, "Wafer bonding and layer splitting for microsystems," *Advanced Materials*, vol. 11, pp. 1409-25, 1999.

[15] S. R. Sakamoto, C. Ozturk, B. Young Tae, J. Ko, and N. Dagli, "Low-loss substrate-removed (SURE) optical waveguides in GaAs-AlGaAs epitaxial layers embedded in organic polymers," *IEEE Photonics Technology Letters*, vol. 10, pp. 985-7, 1998.

[16] K. A. Black, "Fused Long-Wavelength Vertical-Cavity Lasers," in *Electrical and Computer Engineering*. Santa Barbara: U.C. Santa Barbara, 2000.

[17] D. V. Tishinin, P. D. Dapkus, A. E. Bond, I. Kim, C. K. Lin, and J. O'Brien, "Vertical resonant couplers with precise coupling efficiency control fabricated by wafer bonding," *IEEE Photonics Technology Letters*, vol. 11, pp. 1003-5, 1999.

[18] S. Noda, K. Tomoda, N. Yamamoto, and A. Chutinan, "Full three-dimensional photonic bandgap crystals at near-infrared wavelengths," *Science*, vol. 289, pp. 604-6, 2000.

[19] S. M. Garner, L. Sang-Shin, V. Chuyanov, A. Chen, A. Yacoubian, W. H. Steier, and L. R. Dalton, "Three-dimensional integrated optics using polymers," *IEEE Journal of Quantum Electronics*, vol. 35, pp. 1146-55, 1999.

[20] V. A. Aksyuk, F. Pardo, C. A. Bolle, S. Arney, C. R. Giles, and D. J. Bishop, "Lucent Microstar micromirror array technology for large optical crossconnects," presented at SPIE-Int. Soc. Opt. Eng. Proceedings of Spie - the International Society for Optical Engineering, vol.4178, 2000, pp.320-4. USA.

[21] M. C. Wu, "Micromachining for optical and optoelectronic systems," *Proceedings of the IEEE*, vol. 85, pp. 1833-56, 1997.

[22] B. Liu, A. Shakouri, P. Abraham, K. Boo-Gyoun, A. W. Jackson, and J.E. Bowers, "Fused vertical couplers," *Applied Physics Letters*, vol. 72, pp. 2637-8, 1998.

[23] B. Liu, A. Shakouri, P. Abraham, and J. E. Bowers, "Push-pull fused vertical coupler switch," *IEEE Photonics Technology Letters*, vol. 11, pp. 662-4, 1999.

[24] B. Liu, A. Shakouri, P. Abraham, Y. J. Chiu, and J. E. Bowers, "Fused III-V vertical coupler filter with reduced polarisation sensitivity," *Electronics Letters*, vol. 35, pp. 481-2, 1999.

[25] B. Liu, A. Shakouri, P. Abraham, and J. E. Bowers, "Vertical coupler with separated inputs and outputs fabricated using double-sided process," *Electronics Letters*, vol. 35, pp. 1552-4, 1999.

[26] B. Liu, Shakouri, A., Abraham, P., Bowers, J. E., "A wavelength multiplexer using cascaded 3D vertical couplers," *Applied Physics Letters*, vol. 76, pp. 282-284, 2000.

[27] B. Liu, Shakouri, A., Abraham, P., Bowers, J. E., "Optical add/drop multiplexers based on X-crossing vertical coupler filters," *IEEE Photonics Technology Letters*, vol. 12, pp. 410-412, 2000.

Chapter 2

Simulations and Theory of Vertically Coupled Waveguide Devices

A thorough analysis of the coupling and mode behavior is critical to the design of these challenging devices. The transfer matrix method (TMM) and effective index technique (EIT) were used to quickly calculate the waveguide effective indices to determine the coupling wavelength. The more computation-intensive finite difference technique (FDT) and coupled-mode theory (CMT) were used to calculate coupling along the device length, and the device outputs at various wavelengths. The coupled-mode equation was numerically integrated as a fast approximation of device outputs for complex waveguide layouts, and to investigate processing difficulties.

2.1 Physics of Coupled-Waveguide Devices

2.1.1 Coupling of Light Between Waveguides

The vertical coupling of these devices is due to the waveguide mode evanescent field overlap. If the modes in the two guides are traveling at the same velocity, and the guides are close enough to allow significant evanescent field overlap between the top and bottom modes, the desired fraction of light will couple from one waveguide to the other after a specific length. The waveguides can be engineered to have modes that both travel at the same velocities and have matched effective refractive indices ($n_{\mathrm{eff}top}=n_{\mathrm{eff}bottom}$). Thus, the structures chosen for the guides are critical to device performance. Dissimilar materials (e.g. different refractive indices as a function of wavelength) and dimensions are also used for some coupled guides to provide a narrower bandwidth through material and waveguide dispersion effects.

The layout shape of the coupled guides can also dramatically affect the device performance. Many of the devices are designed to couple back and forth from one waveguide to the other multiple times to narrow the filter bandwidth.

2.1.2 Transfer Matrix Method and Effective Index Technique

The transfer matrix method (TMM) and effective index technique (EIT) were used together to determine the effective indices of the waveguides. This approach is only valid for weakly guided modes. It was used with all devices except the high index contrast beam splitter devices.

The TMM is outlined in [1] and [2]. It is a 2x2 matrix method to determine the effective index of planar multi-layer optical waveguides.

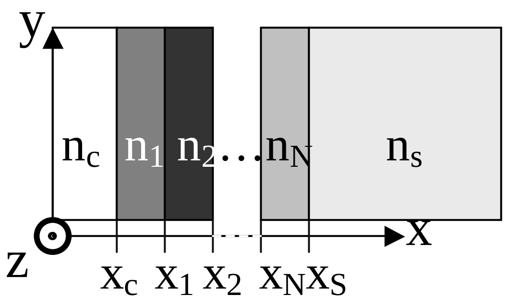

Fig. 2.1 Planar multi-layer optical waveguide.

Figure 2.1 shows a 1-D planar optical waveguide. For light propagation in the z direction, the general solution of the wave equation is given by:

$$E_{z,j} = A_j e^{k_j(x-x_j)} + B_j e^{-k_j(x-x_j)} \tag{2.1}$$

where

$$k_j = \sqrt{\beta^2 - k_o^2 n_j^2} \ . \tag{2.2}$$

A_j and B_j are the complex field coefficients, k_o is the free space wave number, β is the propagation constant, x_j is position of layer j, and n_j is the refractive index of layer j where j=C,1,2,…N,S. From the principle that the field and its derivative are continuous across layer boundaries, it can be derived that:

$$\begin{bmatrix} A_{j+1} \\ B_{j+1} \end{bmatrix} = \frac{1}{2} \begin{bmatrix} \left(1+\rho_j \dfrac{k_j}{k_{j+1}}\right) e^{k_j(x_j-x_{j-1})} & \left(1-\rho_j \dfrac{k_j}{k_{j+1}}\right) e^{-k_j(x_j-x_{j-1})} \\ \left(1-\rho_j \dfrac{k_j}{k_{j+1}}\right) e^{k_j(x_j-x_{j-1})} & \left(1+\rho_j \dfrac{k_j}{k_{j+1}}\right) e^{-k_j(x_j-x_{j-1})} \end{bmatrix} \begin{bmatrix} A_j \\ B_j \end{bmatrix} = T_j \begin{bmatrix} A_j \\ B_j \end{bmatrix} \tag{2.3}$$

where

$$\rho_j = \begin{cases} 1 & TE \\ \dfrac{n_{j+1}^2}{n_j^2} & TM \end{cases} \ . \tag{2.4}$$

This expression of the field coefficients of one layer in terms of those of the previous layer can be iterated multiple times to reach an expression for the complex field coefficients in the substrate layer in terms of those of the cladding layer:

$$\begin{bmatrix} A_S \\ B_S \end{bmatrix} = T_N \cdots T_1 T_C \begin{bmatrix} A_C \\ B_C \end{bmatrix} = \begin{bmatrix} t_{11} & t_{12} \\ t_{21} & t_{22} \end{bmatrix} \begin{bmatrix} A_C \\ B_C \end{bmatrix}. \qquad (2.5)$$

To have finite, guided modes, A_S and B_C must be equal to 0. Hence, t_{11} is equal to 0. The only unknown in the expression for t_{11} is $\beta = k_0 n_{eff}$ (n_{eff} is the effective index). Thus, the 1-D effective index can be found by solving for β given $t_{11}=0$.

To determine the waveguide effective index in 2 dimensions, the EIT is employed in conjunction with the above theory [3]. The TMM is first applied in the growth direction across the regions on either side of the waveguide ridge, and across the waveguide ridge region (regions 1,2, and 3 in Fig. 2.2a) to get three 1-D effective indices (Fig. 2.2b). Then the axes are rotated (exchanging TE and TM) and the TMM is applied again perpendicular to the growth direction using the three 1-D effective indices to get the overall 2-D effective index.

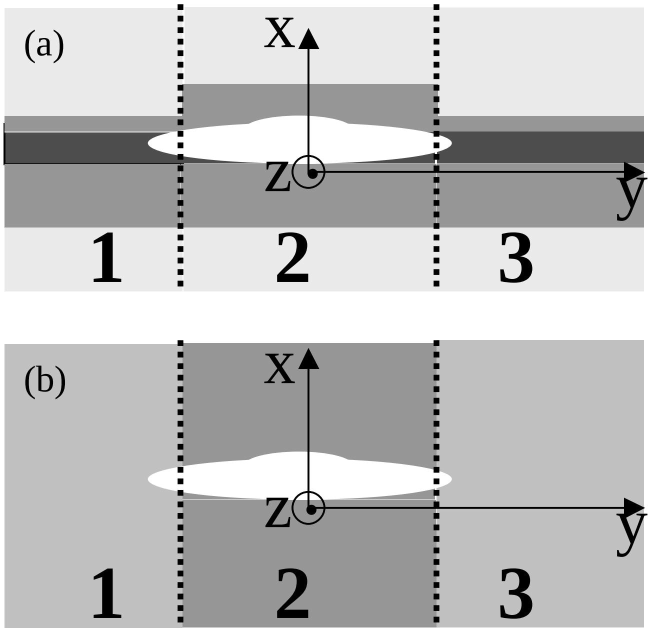

Fig. 2.2ab (a) Breakup of the 2-D waveguide profile into three slab waveguide regions, 1,2, and 3. (b) Color-coded effective index representation of each slab waveguide region. White region represents optical mode half-power contour.

2.1.3 Finite Difference Technique

The finite difference technique (FDT) is a method for calculating the waveguide mode profile and effective refractive index by imposing a grid on the waveguide profile and calculating the mode intensity of the TE mode at every grid point [3].

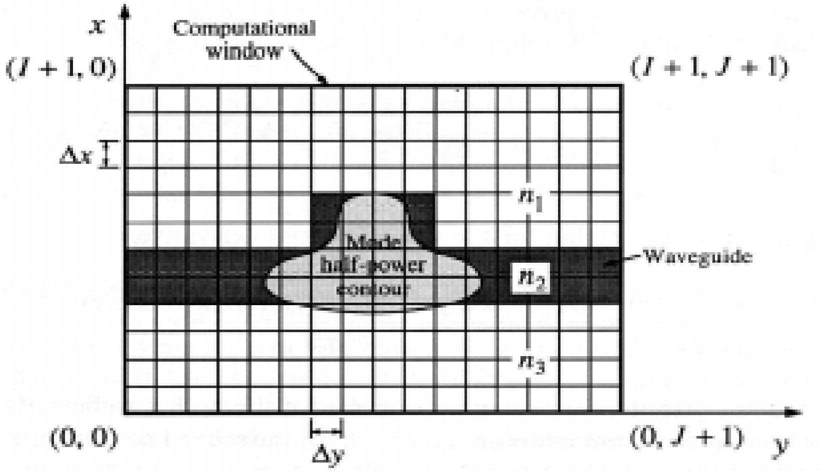

Fig. 2.3 Computational window for FTD [3].

Given the index n^i_j at each point (i,j) of an IxJ grid of spacing Δx, Δy imposed on the waveguide profile (as shown in Figure 2.3), the effective refractive index n_{eff} and the TE fundamental mode profile $\mathbf{U}$ can be found from:

$$\begin{bmatrix} \mathbf{A}^1 & \mathbf{B} & & \mathbf{0} \\ \mathbf{B} & \mathbf{A}^2 & \ddots & \\ & \ddots & \ddots & \mathbf{B} \\ \mathbf{0} & & \mathbf{B} & \mathbf{A}^I \end{bmatrix} \begin{bmatrix} \mathbf{U}^1 \\ \mathbf{U}^2 \\ \vdots \\ \mathbf{U}^I \end{bmatrix} = (n_{eff})^2 \begin{bmatrix} \mathbf{U}^1 \\ \mathbf{U}^2 \\ \vdots \\ \mathbf{U}^I \end{bmatrix} \tag{2.6}$$

where $\mathbf{A}^i$, $\mathbf{B}$ are JxJ matrices composed of n^i_j, Δx, Δy, and the wavelength λ.

$\mathbf{U}^i$ is the transpose of the i^{th} row of the mode profile $\mathbf{U}$ in which U^i_j is the mode intensity at (i,j):

$$\mathbf{U}^i = \begin{bmatrix} U_1^i \\ \vdots \\ U_J^i \end{bmatrix} . \tag{2.7}$$

An iterated sparse matrix program for which eigenvalues and eigenvectors were found by inverse iteration was incorporated to allow faster computations with more grid points [4].

2.1.4 Coupled Mode Theory

Coupled mode theory (CMT) allows the calculation of the coupling of light between two guides as a function of propagation distance, guide dimensions and composition, waveguide separation, and wavelength [3]. It provides a general solution for the top and bottom guide power flow, $|a_{top}|^2$ and $|a_{bottom}|^2$, of a four-port co-directional coupler in the form:

$$\begin{bmatrix} a_{top}(z+dz) \\ a_{bottom}(z+dz) \end{bmatrix} = \begin{bmatrix} f_{11} & f_{12} \\ f_{21} & f_{22} \end{bmatrix} \begin{bmatrix} a_{top}(z) \\ a_{bottom}(z) \end{bmatrix} \tag{2.8}$$

where f_{ij} are functions of z, dz, β_{top}, β_{bottom}, and coupling coefficient κ (Figure 2.4).

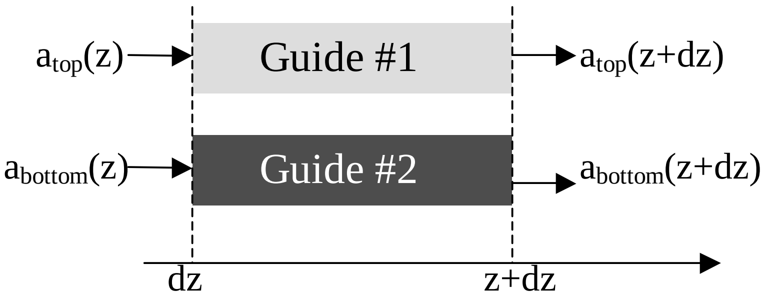

Fig. 2.4 Directional coupler including normalized amplitude coefficients “a” equal in magnitude to the square root of the power flow.

The coupling coefficient κ is given by an integral over the cross-sectional area of waveguide perturbation that includes the dot product of the mode profiles. The mode profiles are calculated with the FDM. Since κ is dependent on the waveguide separation, and the waveguide separation changes with z for all of the devices studied in this thesis, κ is a function of z. To evaluate $a_{top}(z)$, $a_{bottom}(z)$ it is necessary to iterate (2.8) from $a_{top}(0)$, $a_{bottom}(0)$ because of the z-dependence of κ. Arbitrary waveguide layout shapes can be analyzed in this manner.

Limitations to CMT include the assumptions that coupling is weak, the coupling coefficient is small, and the waveguide effective indices are constant along the device. Thus, CMT is applicable for all of the devices detailed in later chapters because there is weak modal overlap between the top and bottom guides. Constant waveguide effective indices may not always be achieved if growth or processing problems occur, however.

2.1.5 Ricatti Coupled-Mode Equation Integration

If κ is approximated to be non-wavelength-dependent, the device output as a function of wavelength can be determined very quickly by numerically integrating the coupled mode equation. Though the FDT/CMT approach may be more accurate because it accounts for the wavelength dependence of κ, the numerical integration approach was used to compare layout shapes because it is faster.

Let R and S be defined as the complex amplitudes of the incident and coupled waves in the device. The relationship between R and S for co-directional coupling takes the form of a single nonlinear Ricatti equation where S and R are expressed in terms of a variable ρ (defined as their ratio multiplied by a phase factor) [5, 6]:

$$\frac{d\rho}{dz} = -j\left(2\delta + \frac{d\phi}{dz}\right)\rho + j\kappa(\rho^2 - 1)\ , \tag{2.9}$$

where

$$\rho = \frac{S}{R}e^{-j\phi}\,. \tag{2.10}$$

Here ϕ is a measure of the spatial variation in the phase matching condition, and δ is a measure of the deviation of the wavelength of operation from the center wavelength for which the device was designed to couple 100%:

$$\delta = \frac{2\pi}{\lambda}(n_{efftop} - n_{effbottom}) \tag{2.11}$$

The coupled-mode equation (2.9) can be numerically integrated over the device length to find ρ at the device output. A fourth-order Runge-Kutta integration is used because of accuracy and ease of implementation.

When little power is coupled (ρ << 1), the solution of the above Ricatti equation becomes much simpler. For this case, a Fourier transform relation exists between ρ and the coupling coefficient κ [6]:

$$\rho\left(\frac{L}{2}\right) = -je^{-j(\phi+\delta L)}\int_{-\frac{L}{2}}^{\frac{L}{2}} \kappa(z)e^{j(2\delta z+\phi)}dz \quad , \tag{2.12}$$

where L is defined as the device length. Fourier transform simulations were performed to corroborate the Ricatti equation numerical integration solution for low coupled powers.

The filter response in terms of the fraction of input power coupled to the drop port can be found by noting that:

$$\frac{P_{coupled}}{P_{input}} = \frac{\left|S^2\right|}{\left|S^2\right|+\left|R^2\right|} = \frac{\left|\rho^2\right|}{\left|\rho^2\right|+1} \tag{2.13}$$

Thus, we have two methods to relate coupled power to coupling coefficient κ: integration of (2.9) or evaluation of (2.12).

To find the bandwidth, sidelobes, and pass band shape for coupling corresponding to any arbitrary function (such as those in Table 2.1), we set κ(z) proportional to that function [5]. The coupled power can then be calculated over the wavelength deviation (δ) range of interest using (2.9) or (2.12) with this κ(z). κ can be calculated for a particular waveguide spacing in conjunction with the FDT [3]. In this manner, κ can be found for any waveguide spacing and hence the waveguide layout and device length for any κ(z) can be determined.

2.2 Applications of Simulations to Device Design

2.2.1 Structure and Device Coupling Simulation Programs

The above theory was used to simulate device performance with two MATLAB programs: one that uses TMM and EIT to quickly calculate the effective index given a waveguide structure, and the other that uses FDT and CMT to calculate the coupling as a function of length for various waveguide layouts. These programs allow critical approximations without which device design would be impossible to complete in a timely manner. Details of the programs are included in Appendix A. A slower commercial software program that uses the beam propagation method (BPM) was used to confirm the MATLAB program results.

Since all OADM devices exhibit low index contrast guiding, TMM and EIT were used for the design of those devices. All initial modeling of the OADMs was performed with the TMM/EIT MATLAB program to test that the compositions, layer heights, and waveguide widths chosen would couple at or around the desired wavelength of 1550nm. The TMM/EIT program was the fastest program available that calculated the effective refractive indices of the two guides. Figure 2.5 shows a plot of refractive index as a function of wavelength corresponding to the two-channel OADM discussed in Chapter 5, engineered to give coupling at 1550nm.

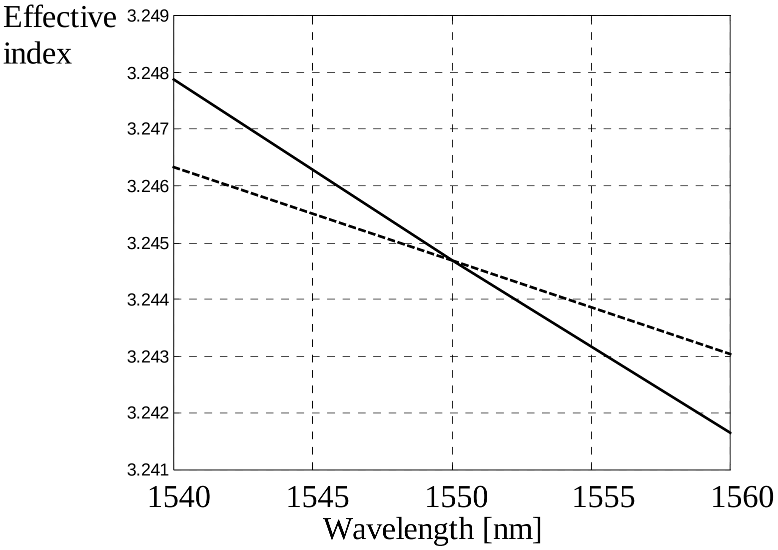

Fig. 2.5 Effective index vs. wavelength for vertically coupled waveguides of OADM, calculated with TMM/EIT program.

Once coupling at the desired wavelength is achieved with the TMM/EIT program, the coupling of light along the length of the device is modeled with the FDT/CMT program. The lengths of the devices simulated with the FDT/CMT program are adjusted until 100% coupling is achieved at the center wavelength. Figure 2.6 shows the coupling along the length of a device calculated with the FDT/CMT. After that, drop port power across a range of wavelengths can be calculated to determine device filtering.

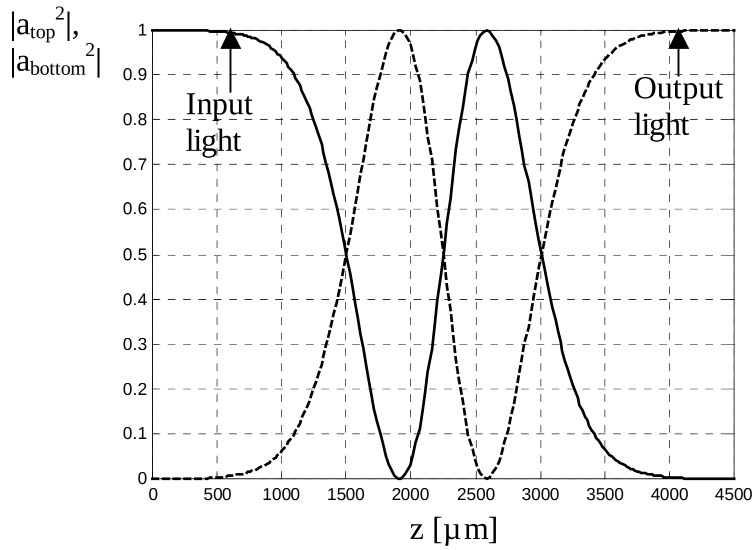

Fig. 2.6 Relative power flow in two coupled guides along device length.

One of the most precise and widely used methods of determining output mode intensities given initial wave amplitudes and waveguide parameters is the BPM. Before the mask is created, as a check that the MATLAB simulations are correct, BeamPROP™ [7] BPM commercial software is used to confirm that 100% coupling will occur with the chosen materials and dimensions. The BPM solves the paraxial wave equation in incremental steps along the propagation direction [3]. An agreement between BeamPROP™ and the FDT/CMT program of within 15% of device length is always achieved. Differences between the programs can be attributed to computer processor limits on the number of points composing the grids imposed on the waveguide cross-sections. Unfortunately, BeamPROP™ was very slow (several hours to days per 3-D device simulation). Thus, it is only used as a back-up resource to confirm the FDT/CMT results. Neither the MATLAB programs nor the commercial software are 100% accurate given the finite grid sizes, and multiple estimates may yield a better design.

2.2.2 Structure Selection Issues

All devices were designed to be composed of single-mode InP/InGaAsP waveguides. Waveguides were single-mode so that 100% of the power could be coupled out. InP was used for compatibility with active InP devices, though none were incorporated in this thesis. Weakly guided ridge waveguides of InGaAsP cores clad with InP were used for low losses when possible. To avoid bending losses with the compact beam splitter however, the InGaAsP cores were etched through. Structures for the two types of devices are shown in Figure 2.7.

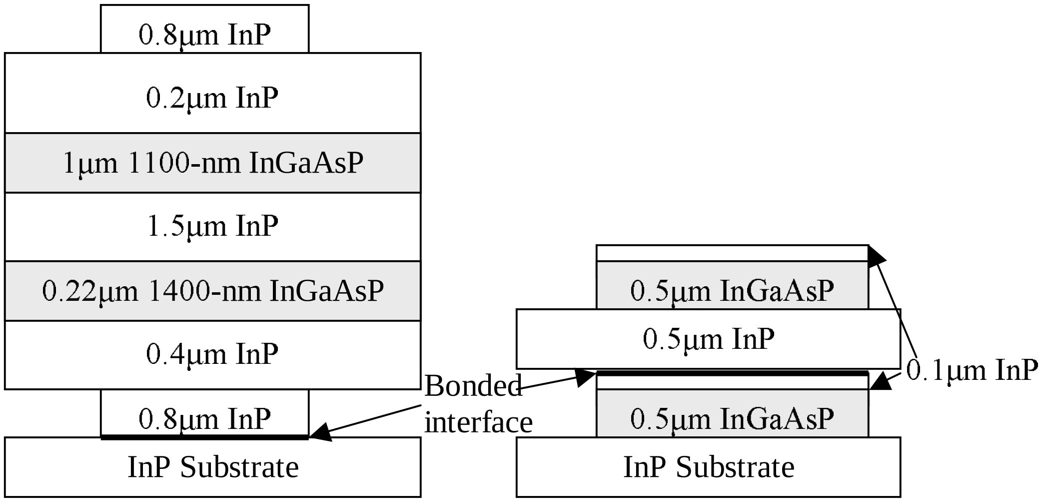

Fig. 2.7 Structure of OADM (left) and bottom and middle waveguides of 3-layer beam splitter (right). Beam splitter cores are 1300-nm InGaAsP.

Structures were chosen based on the desired device functionality. The 3-layer beam splitter was designed to operate over a wide wavelength range. Thus, the waveguides on the various layers were made as similar as possible to avoid wavelength filtering from dispersion effects. The guides were made of the same materials to prevent material dispersion, and were as similar in layer thicknesses as possible to avoid waveguide dispersion.

The structure for all OADM devices was chosen based on the structure successfully used with the previous OADM effort at UCSB [2]. Waveguide and material dispersion of the top 1100-nm, 1-μm thick waveguide core and the bottom 1400-nm, 0.22-μm thick waveguide core provided filtering for the various channels. Materials that gave greater dispersion would have been preferred, but light absorption and index contrast limits prevented the use of InGaAsP of much higher or lower bandgap. Other materials of more dissimilar material dispersion such as GaAs/AlGaAs were considered, but rejected because of lower projected bond yields. In general, bonds between two samples of the same material are more successful than bonds between different materials.

The layer thicknesses were all chosen to be the same as those used previously, but the InGaAsP compositions were altered slightly. Exact structures are shown in Chapter 5. Optimizing the thickness of the InP between the two InGaAsP cores would have increased coupling strength and reduced device length, but was not attempted because too many other variables were altered in each successive processing run.

Initially, Henry et al's [8] index approach was used to calculate the refractive index of all InGaAsP used in the devices. It was discovered that the first several OADMs fabricated coupled at wavelengths which were over 60nm below the design wavelength. For InGaAsP of bandgap around 1100nm, experimental InGaAsP refractive index data [9] proved to be closer to values derived with the Weber index expression [10]. It was found from the TMM/EIT simulations that a lowering of the bandgap wavelength of the ~1100-nm InGaAsP by 30nm would yield 100% coupling near 1550nm without mask or layer height variations.

One of the obstacles that remains, however, is the lack of growth precision. In fact, for the OADMs, the growth of InGaAsP of undesirable bandgaps was a bigger challenge to the creation of successful devices than the wafer bond step. The reason the OADMs are so sensitive to growth is the strong material and waveguide dispersion, as shown in Figure 2.5. Unfortunately, the dissimilarity of the slopes of the effective index vs. wavelength of the two guides leads to a very large change in the coupling wavelengths when the guiding layers deviate slightly from those desired. Increasing the bandgap wavelength of the 1100-nm InGaAsP by 1nm decreases the center wavelength of the device by 4.1nm; similarly, the ratio of wavelength shifts for the 1400-nm InGaAsP is 2.5:1. The growth uncertainty of InGaAsP bandgaps was 10 to 20nm. Roughly one-quarter of the growths were unusable as they produced devices that coupled outside of the 160-nm tuning range of the tunable laser. Comparisons of desired OADM growths versus actual growths that yielded working devices are shown in Chapter 5. Devices of crossing angles or lengths other than the theoretical ideal were used in these cases to allow 100% coupling when the actual growth parameters deviated slightly from those desired. Devices of varying degrees of coupling were a useful precaution even for the perfect growth case, however, because the FTD/CMT simulations never matched the BeamPROP™ simulations exactly.

Another issue in the device design was coupling loss due to the bonded junction. Earlier measurements showed that the excess loss induced by the bond is 1dB/cm when a bonded junction is placed between the InGaAsP guiding layer and the top InP cladding of a waveguide [2]. The main cause of loss at the bonded interface is still not fully understood. No voids are visible at the bonded interface under SEM magnifications as large as 40 x 10^3, so optical scattering loss due to non-uniformities at the junction should not be significant. Crystallographic defect and residual impurity concentration at the bonded interface is high, however. For example, with InP/GaAs bonds, very high levels of oxygen were confirmed to be present at the junction with Second Ion Mass Spectroscopy (SIMS) [11]. These defects and impurities may become charge-trapping centers, which can cause free carrier absorption through charge trapping and recombination/generation processes [2].

Though a 1dB/cm loss may be quite reasonable when compared to all of the advantages afforded by wafer bonding, it is still preferable to avoid it. The 3-layer beam splitter was designed to have coupling across the bonded interface because this cannot be avoided for devices of more than two waveguide layers. Also, the higher waveguide losses due to etching through the InGaAsP cladding already dominated the bonded interface loss. On the other hand, since the OADMs only had two waveguide layers, they were designed to not couple light across the bonded interface. As wafer bonding begins to be used for more complex multi-layer devices, careful planning or algorithms to reduce coupling of light across bonded interfaces may become necessary.

2.2.3 Novel Waveguide Layout Simulations

The optimal design of device mask layout includes the reduction of sidelobe levels. Parallel waveguides have prohibitively high sidelobes that often prevent them from being used as effective filters. Substantial improvement in the drop port sidelobe levels are observed with the transition from parallel to crossed x-shaped waveguides. Further improvement is possible, and this section analyzes the theoretical approach.

Many functions from filter theory [5, 12, 13] were compared in terms of bandwidth, sidelobe level, and length using both the 4-th order Runge-Kutta integration and Fourier transform analysis of the Ricatti coupled-mode equation discussed in 2.1.5. The results are shown in Table 2.1. All devices were designed to completely couple light back and forth three times between the input and drop waveguides, with at least 10μm separation between guides at the device edges (except parallel waveguides). 10μm was found to be a sufficient separation between guides to reduce the coupling to negligible levels (less than 0.5% per 500μm). The parallel waveguides were simulated to have no lateral separation. These conditions were used instead of a requirement that the devices be the same length because otherwise many devices would be much longer than necessary. It is worth noting that sidelobe levels of less than –32 dB and filter bandwidths over 20% narrower than those of the previous x-crossing devices are possible with certain coupler shapes. Ripples and sidelobes are present with all functions, however, because of the finite device length. A comparison of $\kappa(z)$ set proportional to various taper functions is shown in Figure 2.8. The functions that offer the narrowest device bandwidth ($\leq$ 7.5nm) are very similar. An illustration of the spatial layouts of actual device waveguides with $\kappa(z)$ proportional to selected functions is provided in Figure 2.9.

Name	Taper Function	-20dB half width	Peak first min	Side- lobe	Length	Bandwidth-Length product
Hamming	$1+0.852\cos(2\pi z/L)$	5.9nm	6.8nm	-24.9dB	3960µm	4.67nm-cm
Gaussian	$\exp(-\pi 4.25z^2/L^2)$	6.3nm	7.6nm	-31.5dB	4011µm	5.05nm-cm
Adjusted Hamming	$1+0.93\cos(2\pi z/L)$	6.5nm	7.5nm	-22.3dB	3718µm	4.83nm-cm
X, $\theta=0.3°$	Straight crossing wgs	7.4nm	8.5nm	-26dB	4000µm	5.92nm-cm
Modified Blackman	$1+1.125\cos(2\pi z/L)+0.183\cos(4\pi z/L)$	7.5nm	9.1nm	-32.4dB	4001µm	6.00nm-cm
Blackman	$1+1.19\cos(2\pi z/L)+0.19\cos(4\pi z/L)$	7.5nm	8.5nm	-23.3dB	4000µm	6.00nm-cm
Windowed Sinc, b=3/L	$\sin(2bz)/z\,(1+0.93\cos(2\pi z/L))$	8.1nm	9.3nm	-26.3dB	3653µm	5.92nm-cm
Kaiser $\gamma=10$	$\frac{\gamma}{\sinh(\gamma)} I_0\left[\gamma\sqrt{1-\left(\frac{2z}{L}\right)^2}\right]$	8.5nm	9.6nm	-27.2dB	3793µm	6.75nm-cm
Raised Cos	$1+\cos(2\pi z/L)$	9.1nm	6.5nm	-18.7dB	3390µm	6.17nm-cm
Sinc, b=3/L	$\sin(2bz)/z$	11.4nm	7.1nm	-14.4dB	3126µm	7.13nm-cm
Butterworth N=3 zc=0.185L	$\frac{1}{\sqrt{1+\left(\frac{z}{z_c}\right)^{2N}}}$	11.5nm	12.5nm	-23.9dB	3904µm	8.98nm-cm
Chebychev N=3, $\varepsilon=.2$, zc=0.17L	$\frac{1}{\sqrt{1+\varepsilon^2\left(\cos\left(N\arccos\left(\frac{z}{z_c}\right)\right)\right)^2}}$	18.6nm	12.3nm	-14.2dB	3492µm	12.99nm-cm
Parallel	1	92.9nm	9.2nm	-4.4dB	1927µm	35.8nm-cm

Table 2.1 –20dB half width, first minima of central peak, and magnitude of first sidelobe for various taper functions using 4th order Runge-Kutta numerical integration of coupled-mode Ricatti equation. L denotes device length.

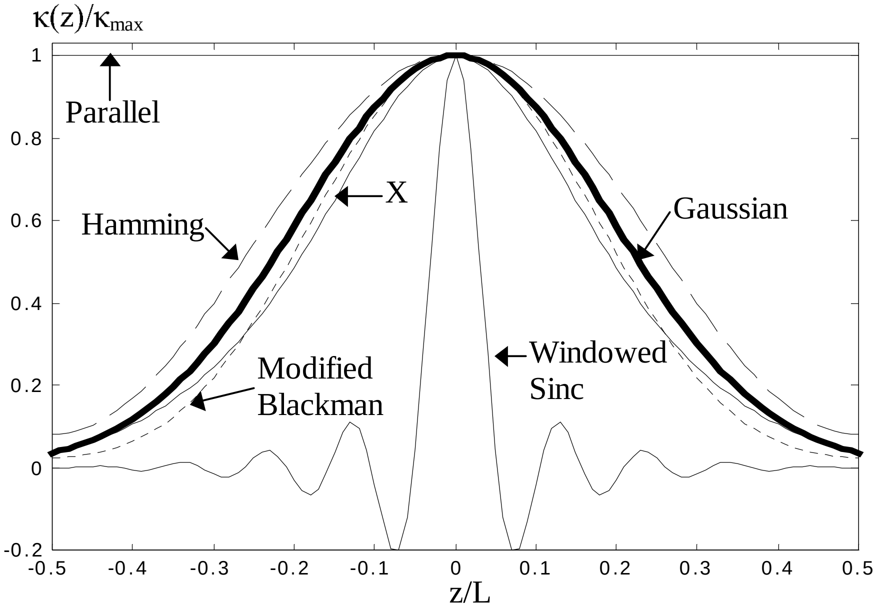

Fig. 2.8 Comparison of κ(z) set proportional to various taper functions.

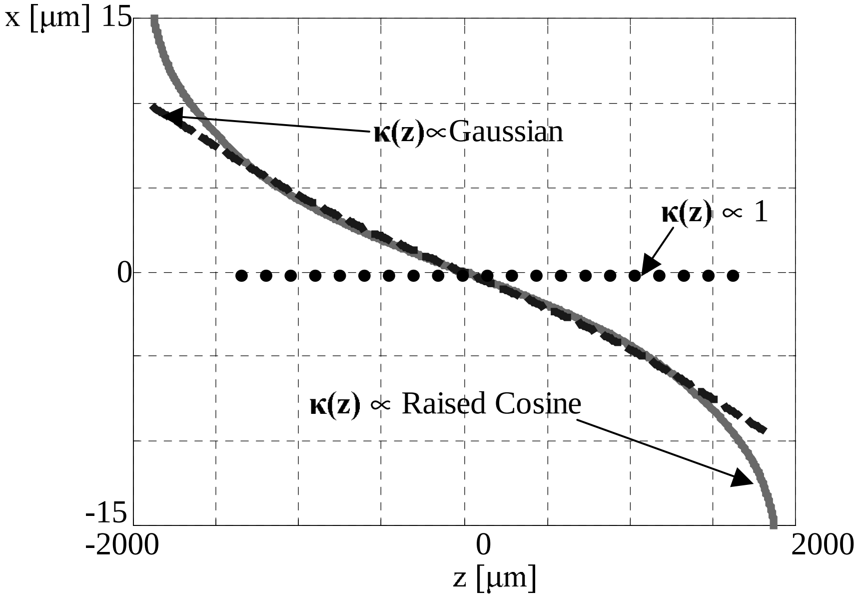

Fig. 2.9 Illustration of waveguide layouts as they would actually appear on mask for devices for which κ(z)∝ Gaussian, Raised Cosine, and 1. The bottom waveguide (not shown) is straight and along x=0.

2.2.3.1 Taper Function Qualities

The Hamming and raised cosine are cosine series apodization functions, often used with discrete Fourier transforms to alleviate spectrum-leakage distortion [13]. The adjusted Hamming allowed an averaging of the qualities between the Hamming and raised cosine: a shorter length than Hamming but lower sidelobes and narrower bandwidth than raised cosine.

The Blackman function is a cosine series apodization function of higher order than Hamming. The modified Blackman was synthesized from Blackman to provide considerable suppression of sidelobes with minimal penalty to bandwidth and length.

Both the Runge-Kutta numeric integration of the Ricatti coupled-mode equation and the Fourier transform approach produce Gaussian filter performance for $\kappa(z)$ proportional to a Gaussian for a very long device. However, the truncation of device length produces ripples in the filter performance for both analysis techniques.

The Fourier transform of a rectangular pulse is given by a sinc function. However, because of the truncation of the function, high sidelobes result. Using an altered Hamming window, the sidelobes and bandwidth can be reduced somewhat at the expense of device length.

Butterworth filter designs are used to approximate ideal RC low-pass filters to obtain flat frequency response in the passband and a steep roll-off at the cutoff frequency. Chebychev functions are also used to approximate ideal filters.

Compared to Butterworth filters of equal order, they exhibit steeper roll-off at the cutoff frequency, but are typically more difficult to make [13].

The Kaiser taper is based on the modified Bessel function of the first kind of zero order (I_o). As the shaping parameter γ increases, the corresponding filter response is one of increased bandwidth but decreased "rippling" effect from the truncation.

Narrow bandwidths and short device lengths can often be opposing qualities, but several functions gave good results on both counts. Since the lengths of all devices with –20dB bandwidths of 9nm or less were similar, device shapes were selected for fabrication based on projected performance. Based on the results of the previous OADMs, the most desired improvement to the OADM performance is a narrowing of the bandwidth. The second-most desired improvement is a reduction in sidelobe levels. Thus, the main criterion for function selection was –20dB bandwidth and the secondary criterion was sidelobe level. Though the Hamming function provides the narrowest bandwidth in Table 2.1, its sidelobes are only moderate. The Gaussian has a bandwidth only slightly wider than Hamming but it sidelobes are significantly lower. The only function with lower sidelobes than a Gaussian, a modified Blackman, has a significantly wider bandwidth. Thus, the Gaussian was deemed the best function in terms of overall device performance. The fabricated device for which $\kappa(z)$ is set proportional to Gaussian is described in Ch. 5. It is evident from Fig. 2.8 that $\kappa(z)$ differs little for Gaussian, Hamming, and modified Blackman. A comparison of the filter performance for devices with κ(z) proportional to these three functions is shown in Figure 2.10.

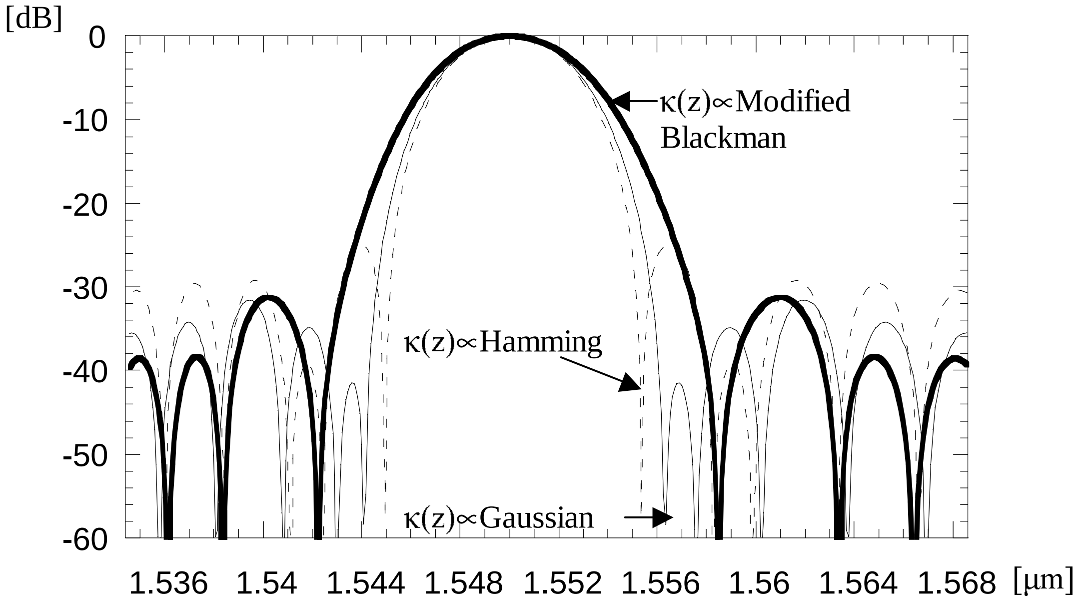

Fig. 2.10 Comparison of relative coupled power vs. wavelength for Gaussian, Hamming, and modified Blackman functions using 4th order Runge-Kutta numerical integration of the Ricatti equation.

A comparison of the filter performance for the 4th order Runge-Kutta integration, Fourier transform, and BPM [7] are shown in Figure 2.11. The three approaches show reasonable agreement for small deviations from the center wavelength. The fast, and easy-to-compute Fourier transform relation is thus considered to work well to obtain a quick approximation for small δ. The BPM and the Runge-Kutta integration approaches are both considered "actual" solutions. The difference between the two “actual” solutions is due to time and memory limitations of grid spacings and step sizes in the computations. The BPM involves a huge number of calculations as the light is simulated to traverse the device step by step with very small step size. Thus, for small coupled powers, a very large number of significant figures must be retained to avoid round-off errors. This is why the BPM curve is not smooth for large wavelength deviations where coupling is low.

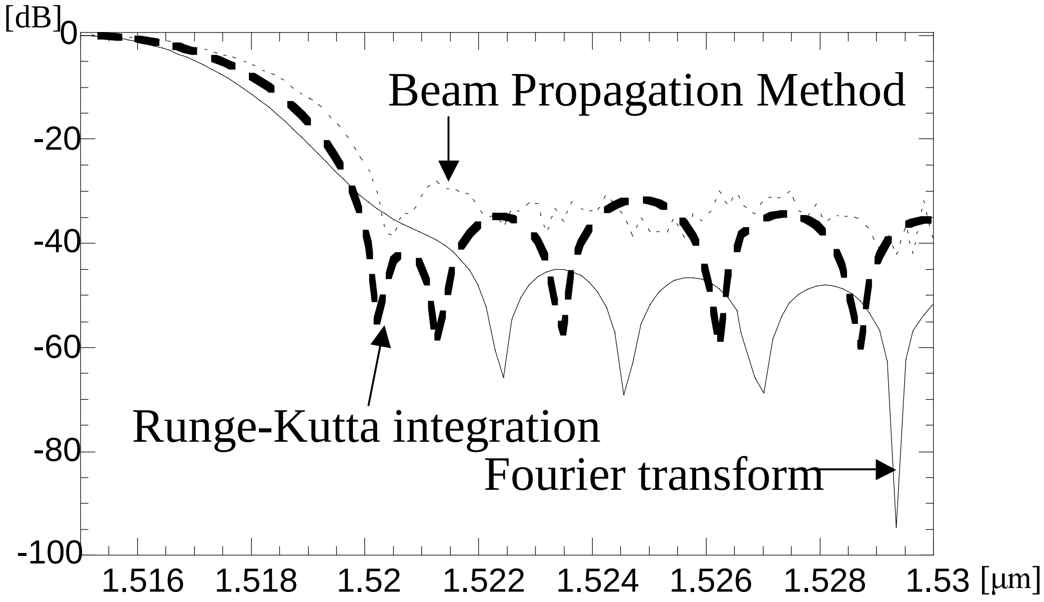

Fig. 2.11 Comparison of OADM performance (relative coupled power vs. wavelength) for coupler for which $\kappa(z)\propto$Gaussian with 4th order Runge-Kutta numerical integration of the Ricatti equation, Fourier transform, and beam propagation method analyses.

2.2.4 Non-Ideal Processing Conditions

One new concern for vertically coupled waveguide devices is waveguide alignment. Traditional horizontally coupled devices are more sensitive to waveguide spacings but also typically require only one mask layer for patterning the guides so alignment has not been an issue. Little has been reported regarding such recent alignment issues [14].

The Gaussian and adjusted Hamming waveguide layouts from above were used in the simulations because they had the most desirable filter characteristics overall. Vertical misalignment is not a concern because one of the two waveguides is assumed to be straight. However, lateral misalignment can lead to filter degradation and can be particularly problematic when aligning a "top" mask layer to layers hidden below the surface after bonding and substrate removal.

To determine the effects of lateral misalignment, the spatial waveguide layout was first determined for a Gaussian $\kappa(z)$. Then, an offset was added to the lateral coordinate of the waveguide layout to "misalign" the guide. $\kappa'(z)$ of this new layout was then calculated. The filter response for lateral misalignment, shown in Figure 2.12, was found by integrating the Ricatti coupling equation using the new $\kappa'(z)$. Though a misalignment by 2μm is rather extreme, it is included to illustrate the degree of misalignment tolerated by vertically coupled waveguide devices. Thus, we note that device performance is not greatly compromised by misalignments on the order of 1μm or less.

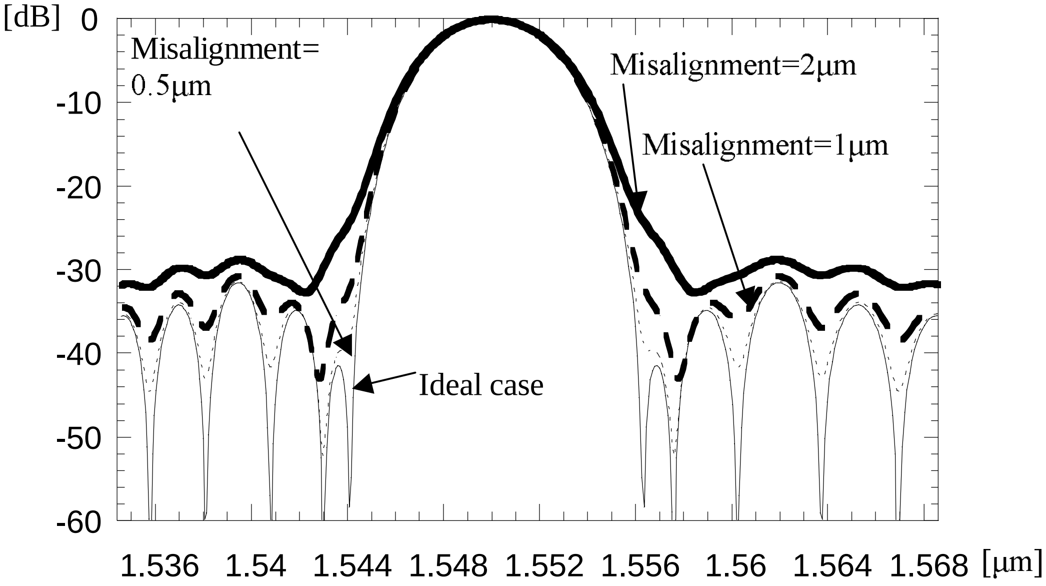

Fig. 2.12 Relative coupled power vs. wavelength for coupler for which $\kappa(z)\propto$Gaussian when laterally misaligned by 0.5, 1, and 2μm. The waveguides are 3μm wide and composed of the theoretical structure of the two-channel OADMs discussed in Chapter 5.

Of course, misalignment is not limited to vertical and lateral positional offsets of the entire mask layer. Rotational misalignment can be a problem when align marks are not sufficiently far apart. Calculation of rotational misalignment is similar to that of lateral misalignment except that instead of simply adding a constant offset to the spatial waveguide layout to determine $\kappa'(z)$, the entire layout is rotated through a coordinate transformation. The results of the rotational misalignment simulation are shown in Figure 2.13.

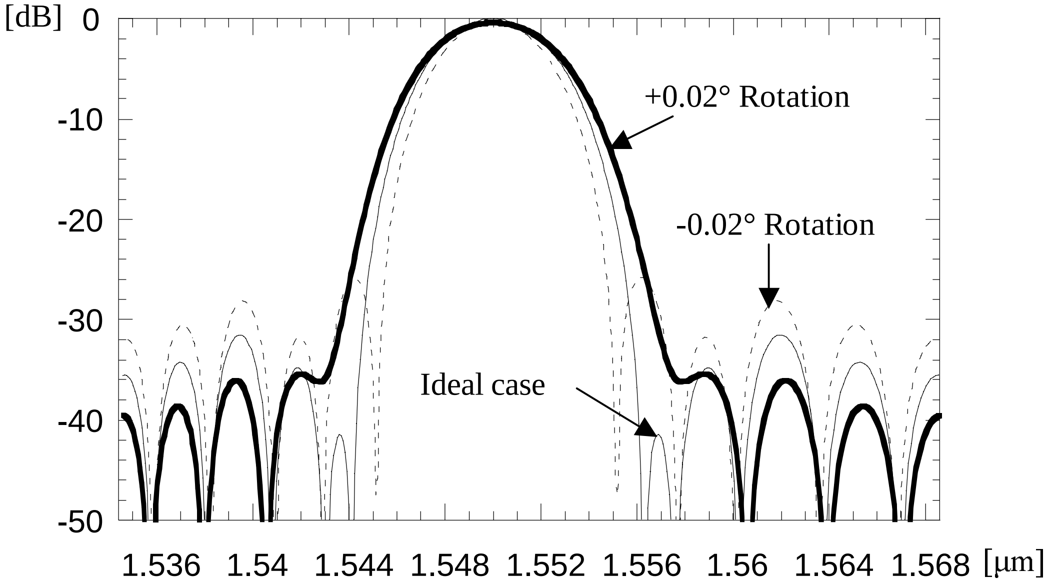

Fig. 2.13 Relative coupled power vs. wavelength for coupler for which $\kappa(z) \propto$Gaussian when misaligned through a rotation about the center of 0.02, and -0.02. The waveguides are 3μm wide and composed of the theoretical structure of the two-channel OADMs discussed in Chapter 5.

Through backside illumination, misalignments of less than 0.5μm can be obtained with IR photolithography. However, it can be difficult to measure the misalignment of the "top" and "bottom" mask layers with this technique after the patterning is completed. A more precise alignment method consists of etching alignment marks through most of the epitaxial layers before bonding such that the marks are visible on the other side of the epitaxial layer after bonding and substrate removal [14]. In this way, verniers to measure misalignment can be included so that the actual effects of the misalignment can be simulated [15].

Another potential obstacle to realizing a device as designed is imperfect epitaxial layer growth. Operating wavelengths and filter bandwidths can change significantly if layers are grown of the wrong thickness or composition. It is useful to simulate from the parameters of a non-ideal growth the required alteration to waveguide widths and heights for desired device operation in order to change them if possible before processing. Mask or etch depth changes are one way to combat the detrimental effects of growth difficulties. Non-ideal growths were simulated by calculating κ as a function of waveguide separation for the poor growth using the FDT and CMT as explained above. The waveguide separation as a function of z for an ideal growth, as would appear on the mask, was then compared to this κ to obtain $\kappa(z)$. Finally, the Ricatti equation with this $\kappa(z)$ was integrated to find the filter behavior for poor growth. Results are shown for a guiding layer grown too thick and too thin in Figure 2.14. One can see that sidelobe levels may increase greatly with only a small difference in waveguide thickness. Devices made from material of undesirable composition can be simulated in a similar manner.

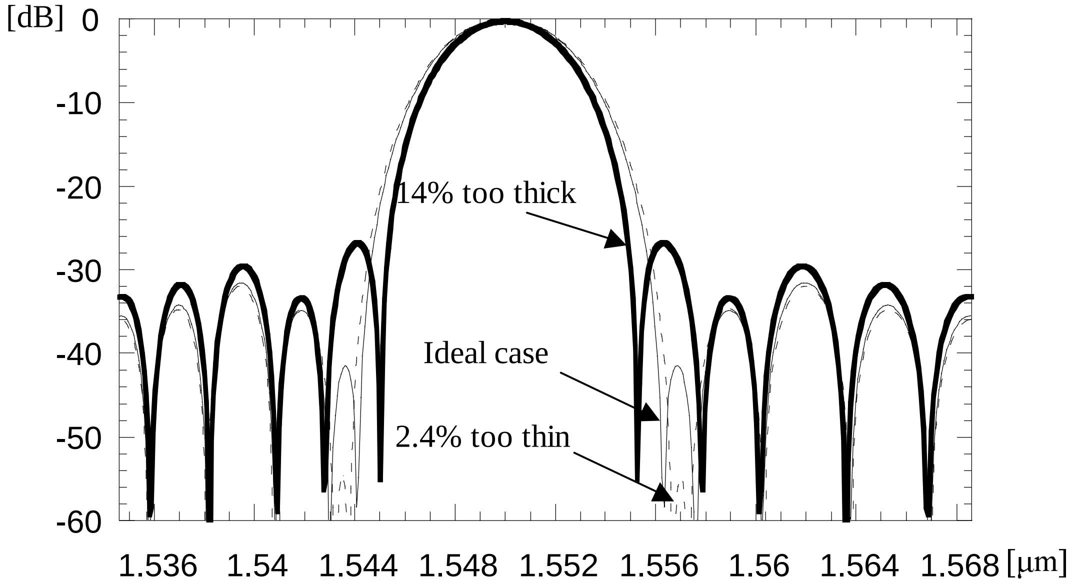

Fig. 2.14 Relative coupled power vs. wavelength for coupler for which $\kappa(z) \propto$Gaussian when the thinner, higher index guiding layer is grown to the wrong thickness. The waveguides are 3μm wide.

For accuracy and speed, the 4th order Runge-Kutta integration of the Ricatti coupled mode equation was used for all misalignment and non-ideal growth simulations.

2.2.5 S-Bend Waveguide Offsets

For all devices with insufficient waveguide separation at the outputs, s-bends were used for lateral separation. Several circular arc s-bends as well as those provided by a conformal transformation analysis were investigated [16]. For the

OADM waveguides, since losses were roughly equivalent for all bend shapes, the simpler circular arc s-bends were used for actual devices. To minimize transmission loss, offsets were used at the junctions between the curved waveguides and the guides to which they connected. 2-D BPM simulations were used to scan over a range of waveguide positions todetermine the offsets for minimum loss [7]. Refractive index differences between the waveguide and surrounding material were around 0.004 for the 1100-nm InGaAsP guides and 0.007 for the 1400-nm InGaAsP guides. For s-bends providing lateral offsets of 19μm, this allowed s-bend lengths of 1500μm and offsets of 0.05~0.15μm between straight and curved guides and 0.1~0.55μm between curved guides for simulated bend losses less than –0.1dB per s-bend.

2.3 Summary

Success in designing vertically coupled waveguide devices has required thorough understanding of the challenges involved. The EIT/TMM, FTD/CMT, and BPM analysis techniques have all been essential to the development of successful devices. These approaches have also allowed devices of more complex layout shape and the potential to understand and overcome processing and growth difficulties.

References:

[1] J. Chilwell and I. Hodgkinson, "Thin-films field-transfer matirx theory of planar multilayer waveguides and reflection from prism-loaded waveguides," *Journal of the Optical Society of America A*, vol. 1, pp. 742-53, 1984.

[2] B. Liu, "Three-Dimensional Photonic Devices and Circuits," in *Electrical and Computer Engineering*. Santa Barbara: U. C. Santa Barbara, 2000.

[3] L. A. Coldren and S. W. Corzine, *Diode Lasers and Photonic Integrated Circuits*, First ed. New York: John Wiley & Sons, INc., 1995.

[4] N. Dagli, "Private Communication,"., 2001.

[5] R. C. Alferness and P. S. Cross, "Filter Characteristics of Codirectionally Coupled Waveguides with Weighted Coupling," *IEEE Journal of Quantum Electronics,* vol. QE-14, pp. 843-847, 1978.

[6] H. Kogelnik, "Filter Response of Non-Uniform Almost-Periodic Structures," *Bell. Syst. Tech. J.*, vol. 55, pp. 109-126, 1976.

[7] "BeamPROP, Version 4.0,".: Rsoft, Inc., 2001.

[8] C. H. Henry, L. F. Johnson, R. A. Logan, and D. P. Clarke, "Determination of the refractive index of InGaAsP epitaxial layers by mode line luminescence spectroscopy," *IEEE Journal of Quantum Electronics*, vol. QE-21, pp. 1887-92, 1985.

[9] B. Broberg and S. Lindgren, "Refractive index of In1-xGaxAsyP1-y layers and InP in the transparent wavelength region," *Journal of Applied Physics,* vol. 55, pp. 3376-81, 1984.

[10] J. P. Weber, "Optimization of the Carrier-Induced Effective Index Change in InGaAsP Waveguides--Applications to Tunable Bragg Filters," *IEEE Journal of Quantum Electronics*, vol. 30, pp. 1801-1816, 1994.

[11] N. Margalit, "High-temperature long-wavelength vertical cavity lasers," in *Electical and Computer Engineering Department*. Santa Barbara: University of California at Santa Barbara, 1998.

[12] A. Kar-Roy and C. S. Tsai, "Ultralow Sidelobe-Level Integrated Acoustooptic Tunable Filters Using Tapered-Gap Surface Acoustic Wave Directional Couplers," *Journal of Lightwave Technology*, vol. 12, pp. 977-982, 1994.

[13] C. L. Phillips and J. M. Parr, *Signals, Systems, and Transforms*, 2 ed. New Jersey: Prentice Hall, 1999.

[14] P. P. Absil, J. V. Hryniewicz, B. E. Little, F. G. Johnson, K. J. Ritter, and P.-T. Ho, "Vertically coupled microring resonators using polymer wafer bonding," *IEEE Photonics Technology Letters*, vol. 13, pp. 49-51, 2001.

[15] R. Grover., 2002.

[16] M. Heiblum and J. H. Harris, "Analysis of Curved Optical Waveguides by Conformal Transformation," *IEEE Journal of Quantum Electronics*, vol. QE-11, 1975.

Chapter 3

Processing and Experimental Setup

Issues related to wafer bonding and the experimental setup are described below. Detailed processing procedures for all devices are provided in Appendix B. The photolithography procedure is described in Appendix C. Wet and dry etching procedures and recipes are detailed in Appendix D. The direct-contact wafer bonding procedure is listed step-by-step in Appendix E. Miscellaneous processing techniques are described in Appendix F. Mask design techniques are noted in Appendix G.

3.1 Wafer Bonding Procedure

Direct-contact 'wafer bonding' describes the phenomenon in which two very clean, flat materials brought into contact will adhere to each other without the use of any adhesives. It has been known for a very long time that optically polished samples will bond to each other, and was studied in quartz glass by Rayleigh in 1936 [1]. However, it was only as recent as 1985 in which researchers at IBM [2] and Toshiba [3] applied heat-assisted wafer bonding techniques for SOI wafer development on a larger scale. The development of the wafer bonding procedure at UCSB is outlined in [4] and [5]. Though many techniques used by others at UCSB have been tried [6, 7], the procedure outlined in Appendix E was found to yield samples with a higher percentage of bonded area.

A graphite bonding fixture is used to apply even pressure to the samples during the anneal. It consists of a rectangular graphite base and lid, a graphite dome, graphite screws, and a 500 to 1000-μm-thick rectangular silicon piece inserted into the base. The soft graphite is thought to provide more uniform pressure on the samples than other harder fixture materials. Torques ranging from 0.2lbf·in to 0.5lbf·in were used. A side view of a graphite bonding fixture including dimensions, the assembled InP samples, and the Si are shown in Figure 3.1. Additionally, the fixture width is 33mm, the height of the curved portion of the dome is 3mm, the dome lip height is 1mm, and the dome diameter is 25mm.

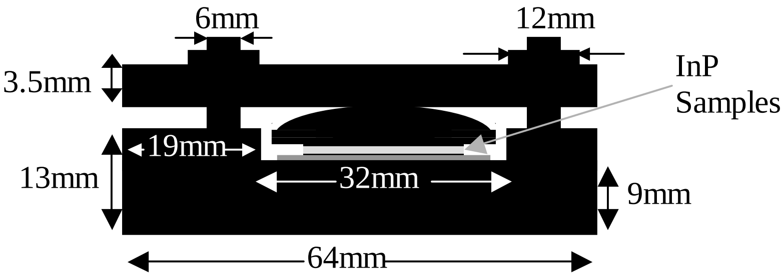

Fig. 3.1 Graphite bonding fixture including assembled InP samples.

After assembly, the samples are annealed. The wafer bonder is a converted liquid phase epitaxy reactor.

Bonded area yield of patterned samples was found to be strongly dependent on the pressure applied by the fixture and sample thickness. As shown in Figure 3.2, higher torques on the bonding fixture screws consistently yield better bonds for samples patterned with bottom-level waveguides and supports. For test samples of the same material, using a torque 0.05lbf·in higher produced a higher yield every time. This consistency shows the importance of carefully selecting bonding parameters for repeatable results. Photoluminescence (PL) maps of finished samples with good working devices did not exhibit any PL non-uniformity (to within 1 nm) from the bond.

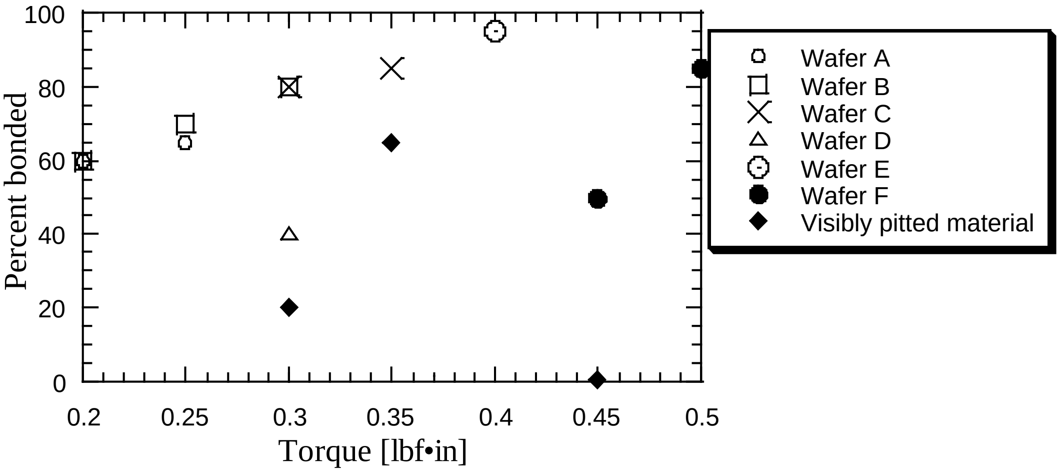

Fig. 3.2 Percentage of bonded area as a function of torque for 14 trial runs from 5 patterned grown InP wafers.

A dramatic improvement of bonded area yield (roughly 55% to 95%) was made over the course of the project. Switching from fixtures that had slightly rough, uneven surfaces to fixtures that were very flat and smooth improved the yield roughly 5 to 10%. Switching from InP host substrates 350-375μm thick to those that were 200μm thick also improved the bonded area yield roughly 20 to 25%. Other factors that appeared to have improved bond yield were the incorporation of a buffered HF dip immediately before bonding, meticulous microscope inspection for particles during the pre-bond clean, removal of visible particles from sample *backsides* after assembly, and careful assembly of the bonding fixtures to ensure uniform pressure on the samples. Care in cleaving samples to avoid portions of the wafer with surface irregularities also improved bond yields. Wafer surfaces were carefully inspected by eye and microscope after cleaving and before bonding.

An SEM of a good bonded waveguide is shown in Figure 3.3. For good bonds, the bonded interface was not visible with an SEM. TEM images show the bonded interface consists of a thin amorphous layer [7].

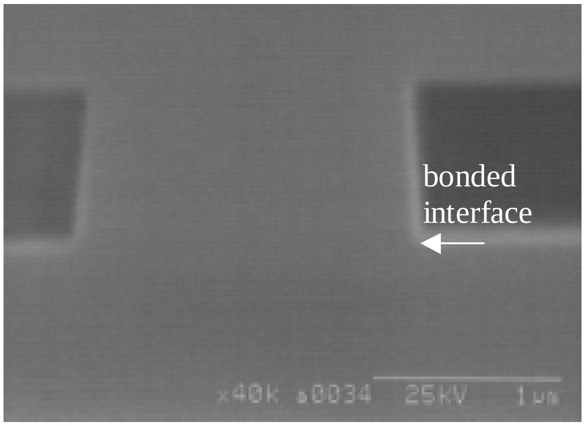

Fig. 3.3 SEM of bonded bottom waveguide ridge including bonded interface.

3.2 Waveguide "Crushing" Problem

In the third year of device processing, a waveguide "crushing" problem was discovered from inspection of the cleaved facets of Gaussian-layout OADM devices. The microscope image suggested damaged bottom waveguides and voids below the waveguides (Figure 3.4), while a more detailed SEM picture suggests the host substrate facet immediately below bottom-level waveguides was of a different height or flatness with respect to the rest of the host substrate facet (Figure 3.5). The "crushing" was present on 50~90% of the bottom waveguides of the Gaussian-layout OADMs. It was only observed below the 3-μm wide bottom waveguides, however, and not near the 10~30-μm wide bottom supports. Multiple cleaves made along the device length of 5 samples showed the fraction of "crushed" bottom waveguides did not exhibit a clear trend of increasing or decreasing towards the sample center. This problem produced noise in device measurements and was not present on facets of previously fabricated devices.

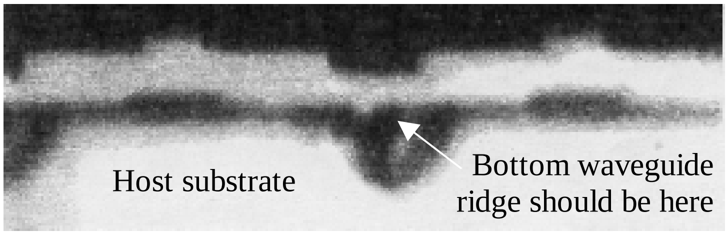

Figure 3.4 Cleaved facet of Gaussian-layout OADM viewed with microscope.

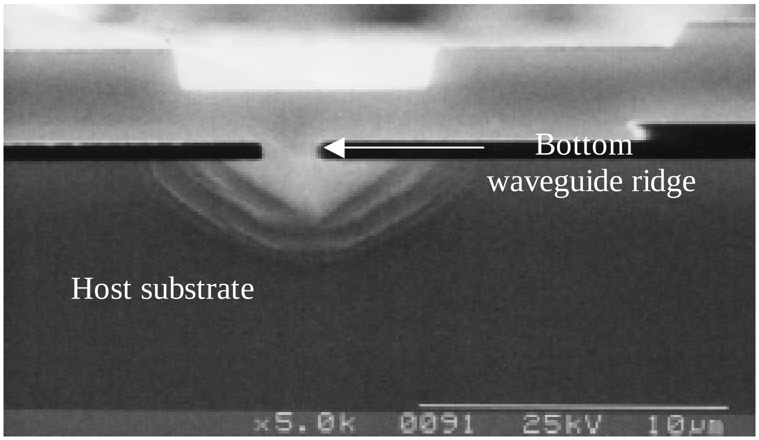

Figure 3.5 SEM image of cleaved facet of Gaussian-layout OADM.

Many attempts were made to discover the causes and solutions of this new problem. It was considered that the "crushing" was due to excessive pressure on the host substrate from the narrow bottom waveguides, because the mask for the Gaussian-layout OADMs had a smaller fraction of supported area than any previous mask. Also, the torque applied to the bonding fixture screws for the Gaussian-layout OADMs was the same as or higher than the torques used for previous devices. Lower torques and a new mask with a much higher fraction of support area were used, but the "crushing" was not alleviated. It was then thought that the problem might be related to post-bond mask aligner pressure. Two samples were cleaved and inspected before and after the top waveguide photolithography step, but even mask contact pressure sufficient to shatter the mask did not affect the waveguide "crushing". 15 bonded, patterned samples of various epitaxial materials, host wafer thicknesses and bond pressures were cleaved and investigated. Plots of percentages of good and bad waveguides versus torque and percent bonded area showed no correlation. 15-second and 3-minute stain etches in 1:1:10 H_2SO_4:H_2O_2:H_2O were performed to see whether they might affect the material around the "crushing" differently, but SEMs showed only uniform etching of the InGaAsP guiding layers. It was considered that more recent wafers might exhibit greater bowing, but both new wafers and those from several years ago exhibited 2μm bowing per cm (8.5 times the bowing of a 4-inch Si wafer). Lapping the host substrate before the cleave did not mitigate the problem either.

It was eventually discovered that the use of thinner samples eliminated virtually all "crushing" effects. The more flexible 200-μm host substrates are thought to prevent the "crushing" exhibited by the 350 to 375-μm host substrates because they conform better to the patterned wafer and reduce pressure non-uniformities. Bonding to lapped samples was attempted but failed, presumably because the particles from the lapping could not be satisfactorily removed during the pre-bond clean.

Another problem not witnessed with previous devices was a material deposit on sample facets after cleaving. It appeared as a round, fringed, brown or multicolored film, or a brown deposit that visibly stood out of the plane of the facet when inspected with a microscope. It could not be removed with acetone or isopropanol, and was only partially removed with buffered HF or oxygen plasma. These material deposits were much more numerous near bottom waveguides and edges of supports. For this reason, they were thought to emerge from the enclosed bottom waveguide and support sidewalls during the cleave. Baking the sample at 200°C for several hours to evaporate trapped liquids before cleaving eliminated this problem.

3.3 Substrate Removal

The samples must be mounted on glass slides to protect the host substrate while the other is being etched. Crystal wax is used for mounting because it etches very little in HCl. It is very important to avoid depositing wax on the top and sides of the substrate to be removed to prevent a non-uniform removal. However, if wax does not protect the sides of the bottom substrate during top substrate removal, the bottom substrate edges will become very jagged. The sample would be prone to breakage from tweezer handling. Thus, it is critical that the correct amount of wax be used, and that it is distributed properly. When the samples are viewed from the side, wax should clearly surround the bottom wafer, but should not be visible on the top wafer, as seen in Figure 3.6. During mounting, the wax is melted at 170°C to achieve the correct viscosity for protecting the bottom substrate only.

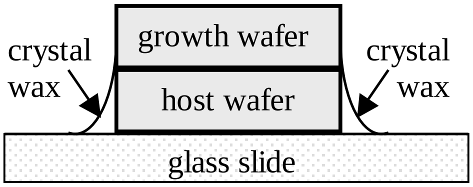

Figure 3.6 Optimal crystal wax distribution for substrate removal.

Before the wax application technique was established, many samples were broken after substrate removal because of jagged host substrate edges. Bonding to a host substrate of a material that does not etch in HCl was considered, but ultimately decided against because of lower projected bonded area yield.

An improvement in bonded area yield was observed when phosphine gas bubbles that form and adhere on the surface during substrate removal were shaken off the sample every couple minutes to allow more uniform, faster, substrate removal. Substrate removal is complete when the exposed surface is mirror-like and no material protrudes above the mirror surface. It is important not to over-etch, and to rinse afterward in H_2O very thoroughly, to avoid trapping acid in the channels between the waveguides for a lengthy period. Any liquid that entered the 0.8-μm high, 12~40-μm wide air gaps surrounding the bottom waveguides and supports was quickly transported throughout the entire sample. The InGaAs etch stop layer is only wet etched away after the sample has been removed from the glass slide to ensure no wax remains on the surface.

3.4 Infrared Photolithography

Infrared photolithography follows the wafer bond and substrate removal to align the buried “bottom”-level waveguides with the “top”-level waveguide mask. Alignment of samples during bonding is not necessary because one of the bonded samples is completely un-patterned—there are no features to align. The host substrate is either cleaved from a commercially double-polished InP wafer or polished to a mirror surface with mechanical lapping material after the bond. This allows for backside infrared illumination to pass through the host wafer and reveal the buried waveguides and alignment marks. Alignment can also be performed by reflecting infrared light off the top surface of the sample, as was done in [6] but this leads to poorer alignment. Alignment within 0.5μm can be achieved with backside illumination.

3.5 Fabrication Tolerances

As noted in Chapter 2 and later chapters, the most challenging fabrication issue for this work was not the wafer bonding, but rather the growth. A better understanding of means to obtain improved growth precision would have a tremendous impact on the ease of realization of these devices. The asymmetric devices in Chapter 5 in particular are so sensitive to the InGaAsP waveguide core compositions and thicknesses that satisfactory growths were nearly impossible to produce with UCSB's horizontal MOCVD reactor. In particular, the thinner InGaAsP core has to be within a few atomic layers of the correct thickness. This limitation was not fully understood at the commencement of this work and is not acceptable for practical manufacturability.

In terms of device yield reduction, the most critical processing step was the wafer bond. High *bonded area* yields can still result in low *device* yields if the devices are very large. Further bond yield improvement beyond 95% is essential for large-scale production of these devices. This could probably be obtained through the use of cleaner, thinner samples of superior surface morphology. However, bond yield improvement techniques were not investigated further in this work because they were greatly outweighed by the growth issues.

The lithographic tolerances of this device are fairly high, however. Variations in waveguide width on the order of a several tens of microns can be easily tolerated for most devices without changing the center coupling wavelength by more than a few nanometers. The devices are also relatively insensitive to misalignments up to 2μm, as noted in Chapter 2.

3.6 Experimental Setup and Techniques

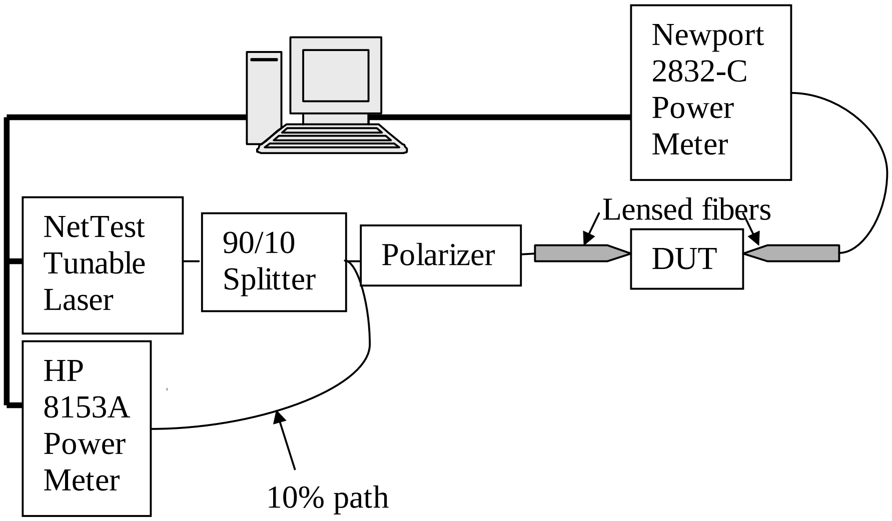

Fig. 3.7 Experimental setup.

The experimental setup is shown in Figure 3.7. The sample is mounted on a copper block with photoresist baked at 110°C for 10 minutes. A TE cooler is incorporated into the device stage for temperature stabilization. Video cameras aimed at the top and side of the device (not shown) are used to align the lensed fibers to the waveguides. The NetTest tunable laser allowed wavelength scans from 1470nm to 1660nm, step size 0.1nm.

The input lensed fiber was aligned using a 10x microscope objective lens and an IR camera at the device output. An 80x microscope objective lens was used for taking IR camera images.

Waveguide losses were measured with a modified Fabry-Perot cavity technique [8].

3.7 Summary

The development of specialized techniques for wafer bonding was integral to successful device fabrication. Device yields were greatly improved as these techniques were incorporated. The measurement setup allowed straightforward wavelength scans to determine device performance.

References:

[1] L. Rayleigh, *Proceedings of Physical Society A*, vol. A156, pp. 326, 1936.

[2] J. B. Lasky, "Waver bonding for silicon-on-insulator technologies," *Applied Physics Letters*, vol. 48, pp. 78-80, 1986.

[3] M. Shimbo, K. Furukawa, K. Fukuda, and K. Tanzawa, "Silicon-to-silicon direct bonding method," *Journal of Applied Physics*, vol. 60, pp. 2987-9, 1986.

[4] J. J. Dudley, "Wafer Fused Vertical Cavity Lasers," in *Electrical and Computer Engineering*. Santa Barbara: U. C. Santa Barbara, 1994.

[5] D. I. Babic, "Double-fused long-wavelength vertical-cavity lasers," in *Electrical and Computer Engineering*. Santa Barbara: U. C. Santa Barbara, 1995.

[6] B. Liu, "Three-Dimensional Photonic Devices and Circuits," in *Electrical and Computer Engineering*. Santa Barbara: U. C. Santa Barbara, 2000.

[7] K. A. Black, "Fused Long-Wavelength Vertical-Cavity Lasers," in *Electrical and Computer Engineering*. Santa Barbara: U.C. Santa Barbara, 2000.

[8] K. H. Park, M. W. Kim, Y. T. Byun, D. Woo, S. H. Kim, S. S. Choi, Y. Chung, W. R. Cho, S. H. Park, and U. Kim, "Nondestructive propagation loss and facet reflectance measurements of GaAs/AlGaAs strip-loaded waveguides," *Journal of Applied Physics*, vol. 78, pp. 6318-6320, 1995.

Chapter 4

Three-Layer Beam Splitter

The previous wafer-bonded vertically coupled InP waveguide device effort at UCSB demonstrated many types of coupling, filtering, switching, demultiplexing, and add-drop multiplexing devices [1]. This work is a continuation of that project. One issue that had yet to be examined in detail is the scalability of these devices. In particular, how many bonded layers are possible? The realization of a device with more than one bonded layer is described below.

A 1:8 beam splitter for 1550-nm light was made from cascaded 3-dB vertical couplers (Figure 1.4). The couplers were incorporated in three layers with two InP-to-InP bonds. To the best of our knowledge, this was the first reported vertically coupled waveguide device of more than two routing layers.

4.1 Beam Splitter Design

The coupled waveguides were designed to be as similar as possible to avoid waveguide and material dispersion effects for a broad device bandwidth (Fig. 4.1). Waveguide composition and dimensions were also optimized for minimal device length. Using the BPM [2], the performance was simulated for various materials, s-bend lengths, and waveguide heights. 1.3-μm InGaAsP (n=3.37 at 1550nm) was chosen as the waveguide core layer rather than InGaAsP with a larger index of refraction because lower index waveguide layers result in shorter coupling lengths;

this can be explained from the coupled-mode point-of-view as an increase in the overlap integral of the two adjacent waveguide modes. InGaAsP of a significantly smaller refractive index, on the other hand, would not have allowed guided modes for compact waveguide dimensions. Thinner waveguide core layers, by providing less modal confinement, also increase the overlap integral between modes of adjacent waveguides and thus reduce the coupling length. The waveguide cores were chosen to be 0.5-μm thick. For strong coupling, the InP below the cores for modal confinement and support of the upper layers was chosen to be as thin as thought certain to withstand the bond pressure. These InP cladding and support beams were made 0.5-μm thick.

The 0.1-μm InP upper cladding above the cores was not only for modal confinement, but also to allow for all bonds to be InP-to-InP. The InGaAsP cores could have been bonded directly to InP, but bonds between the same materials generally provide higher yields. To prevent a coupling asymmetry due to the lack of a 0.5-μm InP support layer above it, the top layer waveguide had a taller upper cladding (0.9μm) than the bottom and middle layer waveguides. Waveguides were 3μm wide for single-mode propagation. Figure 4.1 and 4.2 show the structure of the three grown wafers and side views of the finished device.

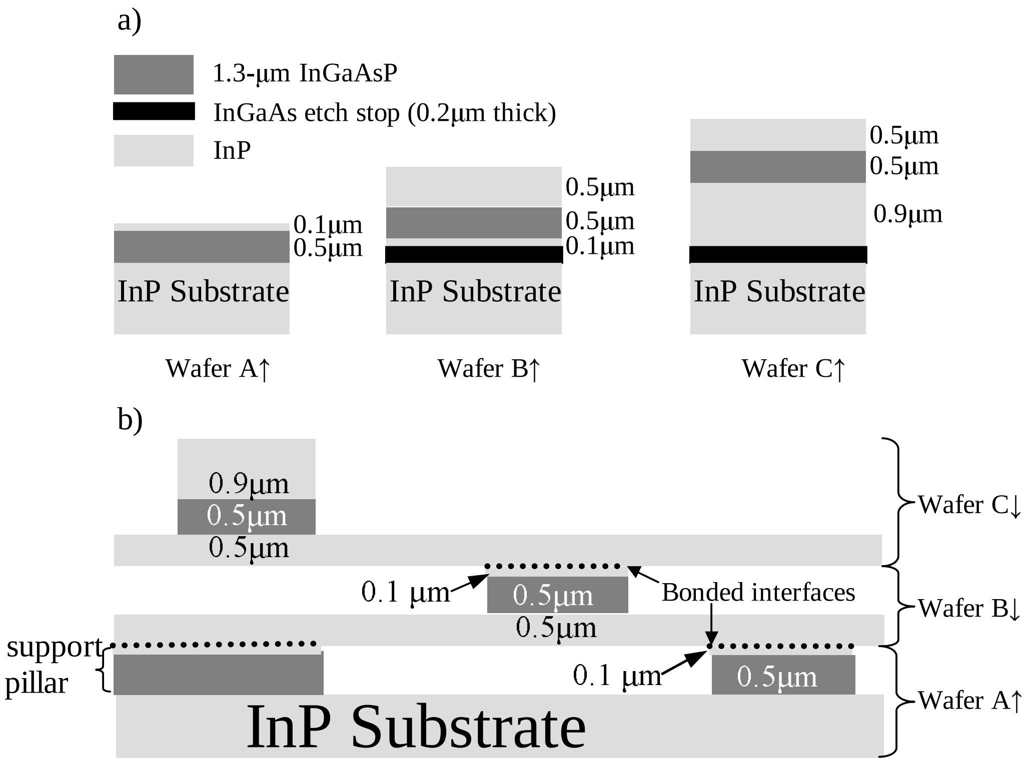

Fig. 4.1. a) Structures of three grown wafers and b) side view of finished device.

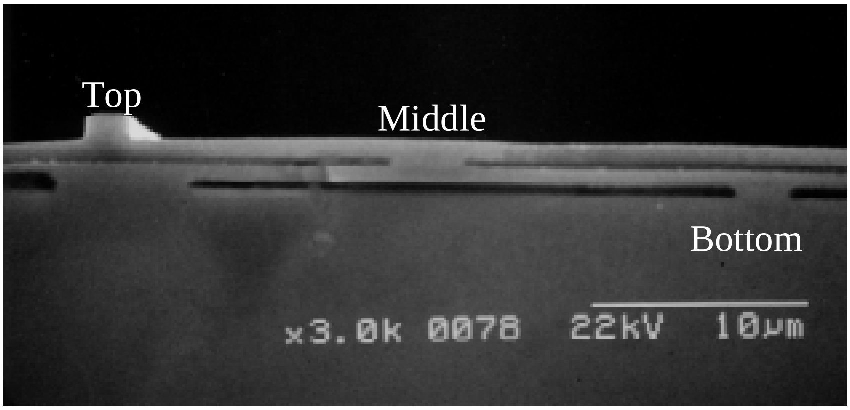

Fig. 4.2. SEM of 3 of the 8 output waveguides. From left to right, top, middle, and bottom waveguides are shown. Bonded region below top waveguide is for support.

With the material and waveguide dimensions used above, the 3-dB coupling lengths for the first (2 outputs), second (4 outputs), and third (8 outputs) stages of the 1:8 splitter are 37µm, 39µm, and 47µm, respectively. The differences in coupling lengths reflect different radii of curvature for the s-bends of the three stages for different output guide separations. The total device length is 580µm.

By contrast, a 1:2 beam splitter made from horizontal couplers using the same waveguide composition and dimensions as with the bottom layer (Wafer A), with a minimum 1 µm separation between waveguides, would be 4.73cm excluding the s-bends. For a 1:8 splitter including s-bends long enough to allow the same output waveguide spacing as the bonded splitter, the total device length would be approximately 14cm. Although a smaller waveguide separation would allow a shorter coupling length, the difficulty in making reproducible and uniform narrow-gap horizontal couplers have hindered their development for ultra-short splitting and switching devices [3]. Thus, vertical couplers offer a great advantage in terms of device compactness.

4.2 Multiple-Layer Bond Yields

Though the thinness of the 0.5-µm InP cladding beams (top layers of Wafers B, C Fig. 4.1a) allowed for shorter couplers, it also caused difficulties with achieving successful second bonds. A torque on the fixture screws of 0.45lbf·in was satisfactory for the first bond, but caused the 0.5-µm thick second layer InP beams to collapse during the second bond. It was found that torques of 0.35lbf·in allowed a successful second bond without collapse.

Despite the improvements to the second bond, overall device yields were low. This was largely because the many improvements to the bonding technique noted in Chapter 3 had yet to be discovered. Of the 14 total first-bond runs, 11 had at least one 580μm x 120μm device intact after the bond. Of those 11, the bonded area yield averaged 70%. 7 second-bond processing runs were attempted, but only 3 were successful because the pressure was not optimized for the first several runs. The overall bond yield for the 3 successful second-bond runs averaged to 65% of the total sample surface. However, when the restriction of good bonded area from the first bond was taken into account, the bond yield for the second bond was 85%. Though perhaps not statistically significant, this improvement in bonded area yield of the second bond compared to the first corroborates the results in Chapter 3 that bonds of thinner, more membrane-like layers lead to higher yields. The improvement is likely due to the conformance of the waveguides on the thin, flexible middle layer InP support beam (from Wafer B, Fig. 4.1) to the un-patterned top layer sample (Wafer C).

4.3 Beam Splitter Measurement Results

The device output at λ=1483nm as captured by an infrared (IR) camera and the corresponding waveguide positions are shown in Figure 4.3. The output beams have slight height differences corresponding to the waveguide vertical positioning.

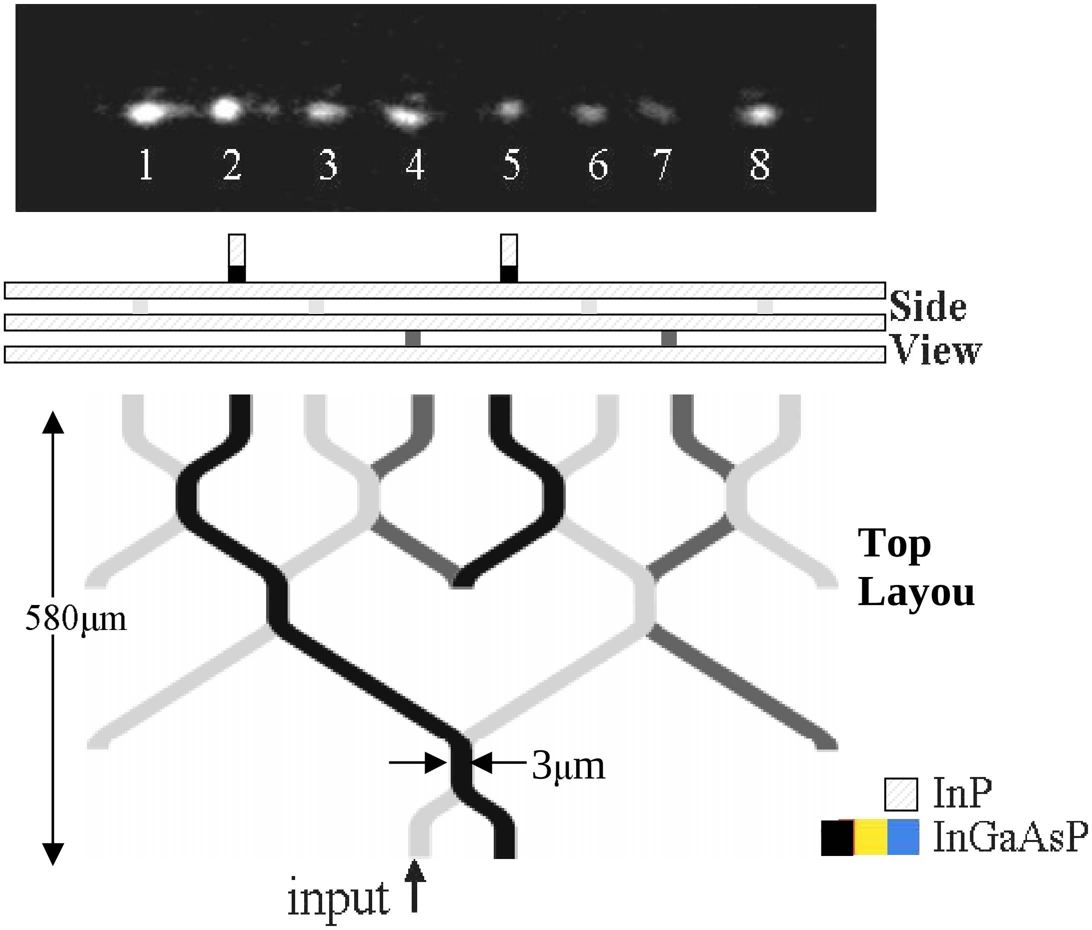

Fig. 4.3. Device output as captured by IR camera and corresponding waveguide layout.

The differences in output intensities is likely due to imperfect alignment between the waveguide layers. Parallel waveguide couplers are particularly sensitive to misalignment compared to many other layout shapes. The degree of misalignment can be seen in the IR camera image as the unevenness in output mode spacings. The separation between all adjacent input and output waveguides was designed to be 15μm for low crosstalk. It was simulated that a lateral misalignment as small as 0.5μm produces 31:69 splitting rather than 50:50. With a misalignment of 0.25μm, the splitting is 42:58. Misalignment may also be the reason the splitting appeared to be more uniform at 1483nm rather than 1550nm when viewed with the IR camera. Better alignment precision through the use of a stepper mask aligner rather than a contact aligner could alleviate the problem.

To measure the polarization and wavelength sensitivity of the device, the output lensed fiber was mounted on a computer-controlled adjustable xyz stage, vertically aligned to the middle waveguide layer, and laterally scanned across the output waveguides at different polarizations and wavelengths. The fiber was not vertically re-positioned for each waveguide during the lateral scan because the waveguides are very close together in the vertical direction (1.1μm). As shown in Figure 4.4, although the splitter can operate at different wavelengths and polarizations, the ratios of light intensity coupled to the various output waveguides changes. The wavelength dependence could be lessened by altering the waveguide structure to allow even shorter couplers, for which the s-bends provide all of the coupling. The device was designed to couple TE light and was not optimized for TM modes. Polarizationindependence could be achieved through a modification of the waveguide structure to allow coupled TM modes to have modal overlaps equivalent to those of TE modes [4].

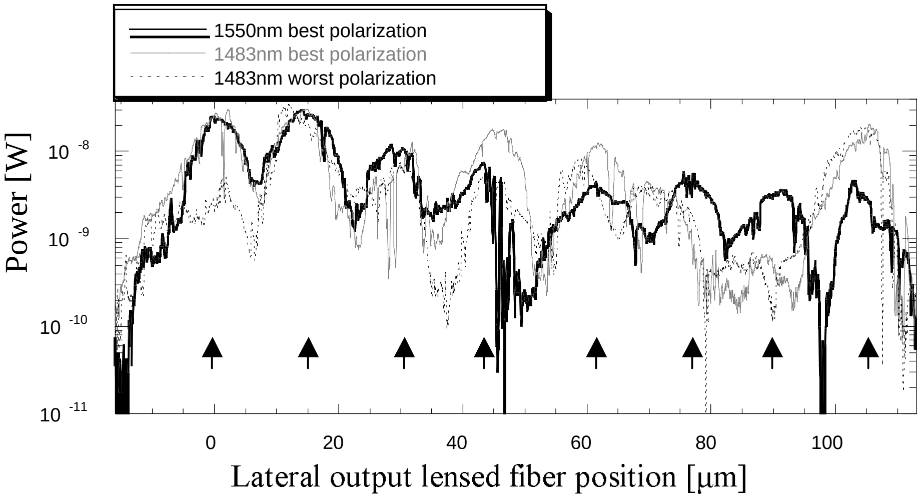

Fig. 4.4. Line scan of device output at 1483nm and 1550nm for best polarization and at 1483nm for worst polarization. Lateral positions of waveguides indicated by arrows.

A Fabry-Perot resonance technique was used to measure the waveguide optical loss [5]. Straight waveguide regions were cleaved off of the sample and tested to give 1dB of loss per 580-μm 1:8 splitter length, or 17dB/cm. Total s-bend bend losses were calculated using BPM [2] to be 0.9dB. Fiber-to-fiber losses, however, were over 30dB owing to poor coupling between the lensed fiber and the non-anti-reflection coated facets, and the several-millimeter long lossy waveguides attached to the device inputs and outputs for cleaving.

4.4 Summary and Conclusions

Multiple layer devices are an exciting possibility with bonding technology. An optical device of more than two waveguide layers that allowed lateral waveguide separation was demonstrated for the first time. Vertical integration of the couplers allowed for a beam splitter length over 100 times shorter than a horizontally integrated counterpart. Splitting non-uniformity, wavelength and polarization sensitivity, and device loss can be reduced through alterations to the waveguide structure and better aligning and packaging techniques.

However, bonding technology must be improved for higher yields before devices with multiple wafer bonds become commercially viable. Double-bonded device yields improved from zero for the first several processing runs to around 50% of all devices on the mask (65% bonded area yield) for the last few runs. Perhaps a careful optimization of the bonding procedure in an industrial research setting would eventually allow yield improvements sufficient for commercialization. Recent industrial results have not been promising for the integration of multiple layers of large III-V devices. However, as material and processing technologies continue to improve, the long-term future of multiple layer wafer bonding does hold promise.

References:

[1] B. Liu, "Three-Dimensional Photonic Devices and Circuits," in *Electrical and Computer Engineering*. Santa Barbara: U. C. Santa Barbara, 2000.

[2] "BeamPROP, Version 4.0,".: Rsoft, Inc., 2001.

[3] A. Shakouri, B. Liu, B. G. Kim, P. Abraham, A. Jackson, A. Gossard, and J. E. Bowers, "Wafer-Fused Optoelectronics for Switching," *IEEE Journal of Lightwave Technology*, vol. 16, pp. 2236-2242, 1998.

[4] B. Liu, A. Shakouri, P. Abraham, Y. J. Chiu, and J. E. Bowers, "Fused III-V vertical coupler filter with reduced polarisation sensitivity," *Electronics Letters*, vol. 35, pp. 481-2, 1999.

[5] K. H. Park, M. W. Kim, Y. T. Byun, D. Woo, S. H. Kim, S. S. Choi, Y. Chung, W. R. Cho, S. H. Park, and U. Kim, "Nondestructive propagation loss and facet reflectance measurements of GaAs/AlGaAs strip-loaded waveguides," *Journal of Applied Physics*, vol. 78, pp. 6318-6320, 1995.

Chapter 5

Passive Crossing Optical Add-Drop Multiplexers

Optical Add-Drop Multiplexers (OADMs) are key channel routing components in Wavelength-Division Multiplexed (WDM) systems. OADM implementation methods include fiber or polymer gratings with circulators [1], arrayed waveguides [2], and cascaded unbalanced Mach-Zehnder structures [3].

The three OADM devices described below were chosen in order to explore the operational limits of near-parallel waveguide filtering devices. Such devices had already proven to be possible candidates for 3D optical integration [4]. To allow a better comparison of the merits of 3D routing technologies, a more thorough investigation of the previously developed devices was performed. The focus of this investigation was scaling and optimal performance.

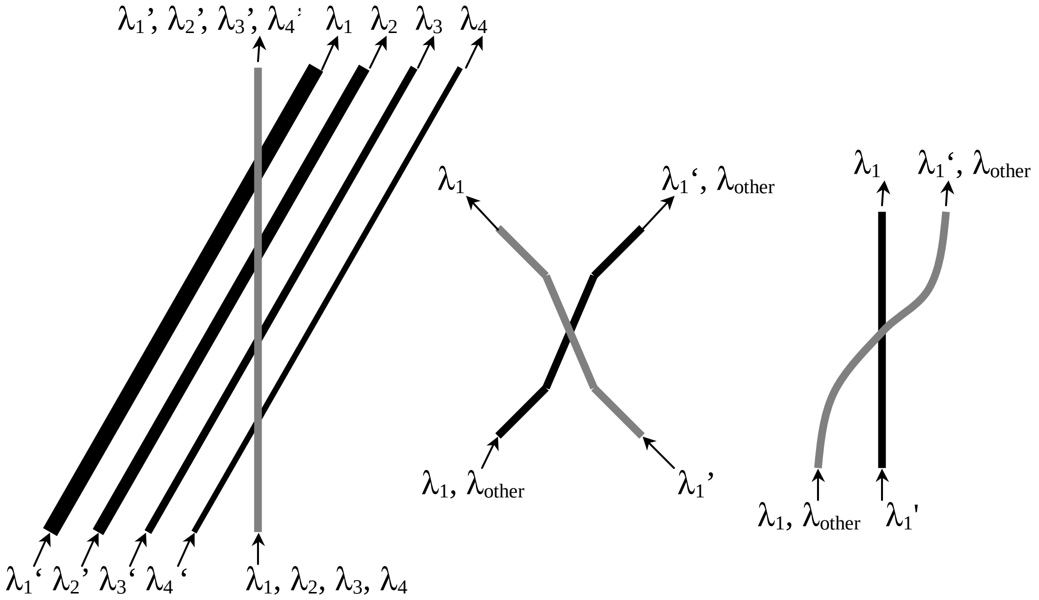

a) b) c)

Fig. 5.1 a) Multiple Channel OADM, b) Dual-angle OADM c) Optimized waveguide layout OADM.

First, an OADM supporting a single add/drop channel had been developed previously [5]. The significance of this device rested on whether it could be easily scaled for multiple channels. A multiple channel OADM, based on the previous single channel device, was thus demonstrated (Fig. 5.1a).

Second, the multiple channel device proved to suffer limitations from device length. An X-crossing waveguide OADM with improved length (as well as lower sidelobe levels) was created by including additional waveguide bends (Fig. 5.1b).

Finally, successive improvements to device performance were found from modification to waveguide shape. These improvements suggested the existence of ideal shapes for device operation. Both an optimization of the waveguide shape and a determination of the best possible performance were attempted through analysis and fabrication of diverse waveguide layout shapes (Fig. 5.1c).

5.1 4-Channel OADM

The multi-channel OADM consists of straight waveguides that cross to form X's. One "in/through" top waveguide is vertically coupled to, and crossed at a shallow angle with, four parallel "add/drop" bottom waveguides (Fig. 5.2). Only one growth was required for the structure because waveguides were etched on both surfaces of the epitaxial material. The different widths of the four add/drop waveguides correspond to separate channels, as the top in/through waveguide will have an effective index matched to that of each bottom guide at a distinct wavelength.

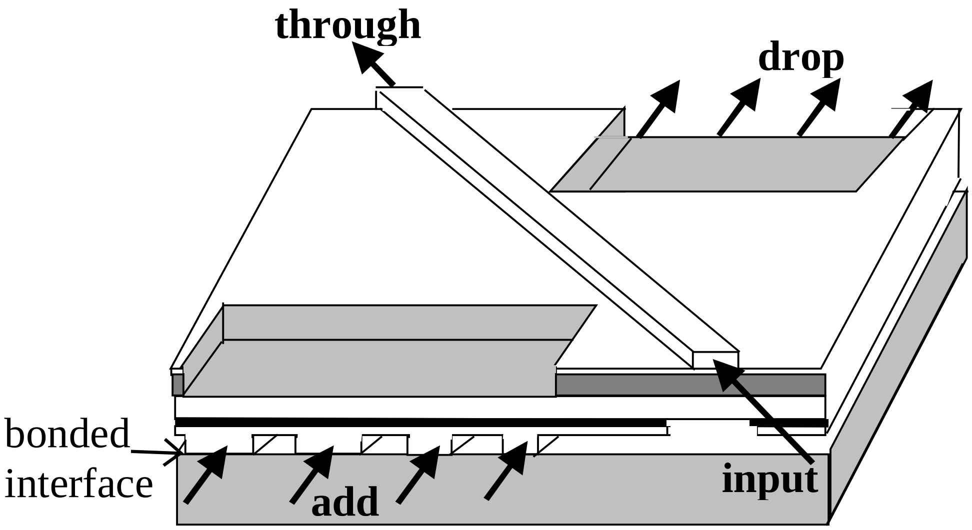

Fig. 5.2 Layout of the OADM.

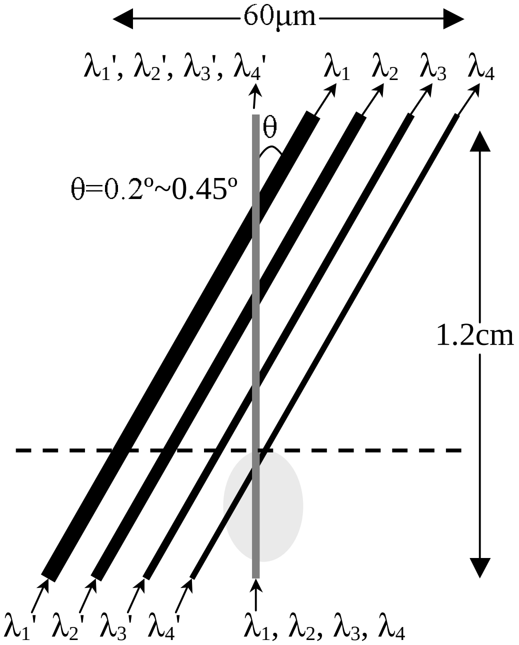

Fig. 5.3 Top view of waveguide layout. Dotted line and gray oval represent cleaved facet and un-bonded region, respectively, as explained below. Note the aspect ratio.

The finished OADMs were 60μm wide and 1.2cm long (Fig. 5.3). Crossing angles between the top waveguide and the four bottom waveguides ranging from 0.2° to 0.45° were attempted because growth variations cause changes in the fraction of light coupled. Thus, all waveguides were nearly parallel. Each device has one top in/through waveguide of width 3μm crossed with four parallel bottom add/drop waveguides of width 2, 3, 4, and 5μm, separated laterally by 10μm for coupling into lensed fibers (Fig. 5.3, 5.4). The X-crossing arrangement allowed by the bonding also provides lateral separation of the top waveguide from the four bottom waveguides, and reduces coherent coupling of sidelobes as well [5].

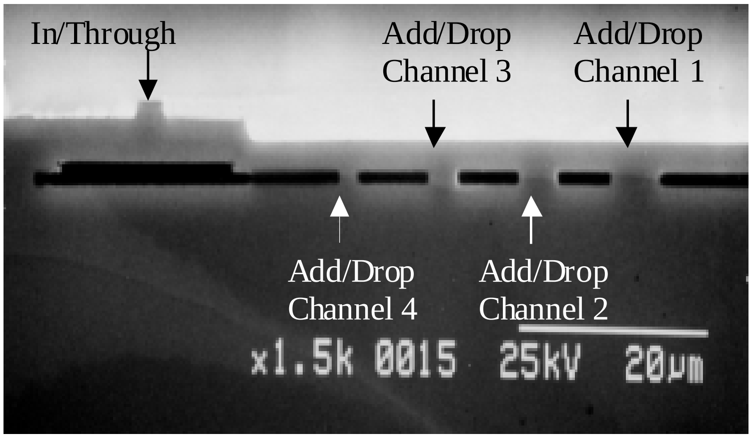

Fig. 5.4 SEM of sample resulting from cleaving of output facet, including in/through waveguide and four add/drop waveguides.

This 4-channel OADM does not have a simple horizontally coupled equivalent, as the waveguides cannot be rearranged or bent in such a manner that they yield an in-plane device with the same capabilities without excessive losses or crosstalk. The dissimilarity between the top and bottom waveguides further complicates any approach to reduce the number of dimensions. Thus, this device illustrates the wonderful flexibility in device layout afforded by wafer bonding.

One of the biggest difficulties with realizing this OADM was device yield. The results of the 14 processing runs are listed in Table 5.1. All of the first 12 samples were of growth material of undesirable InGaAsP bandgaps that would have coupled outside the range of the tunable laser. This was because of the use of an unsatisfactory model for the bandgap versus refractive index relationship of the lower-index InGaAsP as noted in section 2.2.2. It was not until the 2 otherwise good samples were processed and tested from amongst the first 12 runs that the undesirability of the growth was discovered.

Processing result	Failure due to poor bond	Failure due to breakage	Failure due to poor etch	Intact finished device
Incorrect growth	**4**	**5** (one destroyed pre-bond)	**1**	**2** (both with a set of 6 contiguous devices)
Correct growth	**1**	**0**	**0**	**1** (no devices with >50% coupling of all 4 channels)

Table 5.1 Results of all 14 multi-channel OADM processing runs. Failure refers to termination of processing because all devices on sample are destroyed.

Bonded area yield was also a problem for such large devices. Several of the improvements to bonding mentioned in Chapter 3 had been incorporated by this point (the use of BHF, meticulous microscope inspection for particles after acetone/isopropanol swab, careful assembly of fixtures), but other important steps had not (use of thinner samples, flatter fixtures).

The 75 to 80% average bond area yield of 13 total bond runs would have provided a satisfactory device yield for smaller devices but was insufficient for these 4-channel OADMs. Due to processing and growth non-uniformities, comparisons of the 6 crossing angles should be made on contiguous devices from a single processed sample. The bond area yield was much too low to achieve reliable bonding for 6 contiguous devices (3% 6-device-set yield of 13 bonds).

Even for the samples with “good” bonds (9 of 13 had 75% to 95% bonded area) *device* yield per bond varied wildly depending on the location of the un-bonded regions, from 0% to 100%. The device yield was higher than the bonded area yield in cases where the un-bonded area resided on the 2-mm input and output waveguide sections (see Appendix E). The average device yield of the 9 “good” bonds was 40%.

The device consisted of only straight waveguides, with outputs 10μm apart. Less than 0.1% of the coupling of these devices occurs after the waveguides are more than 8μm apart, however. The device could have been made significantly shorter if s-bends or wider crossing angles were incorporated where waveguides were less strongly coupled, as explained in section 5.2.

The bandgaps of the InGaAsP regions of the actual growth (λ_g=1.066μm, λ_g=1.359μm) deviated slightly from that of the desired growth (λ_g=1.068μm, λ_g=1.370μm) needed for room temperature operation (Fig. 5.5). This offset necessitated the heating of the sample to 104.3°C to shift the indices of the material to allow coupling within the range of the tunable laser. The temperature-induced shift in the center wavelengths of the drop channels was 0.39nm/°C.

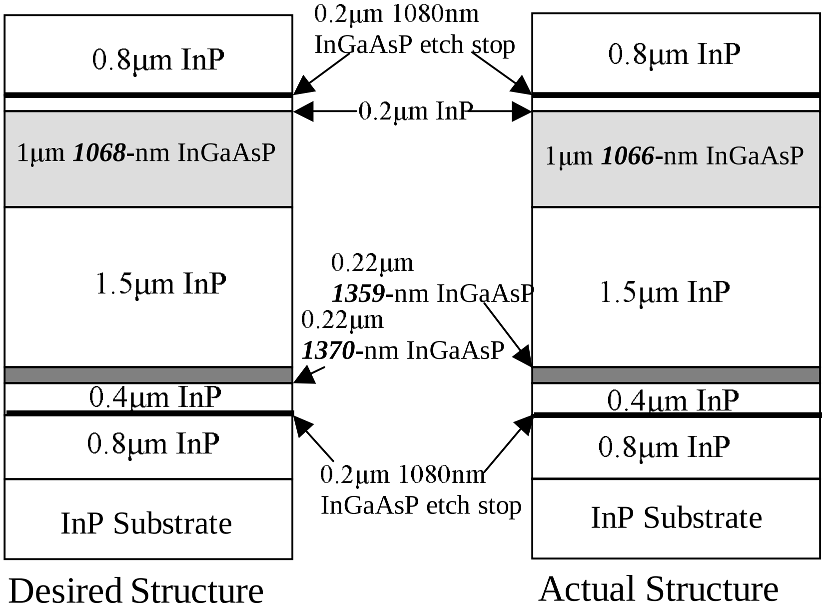

Fig. 5.5 Desired versus actual growths, post-bond.

The center wavelength of the device has a strong dependence on the InGaAsP bandgaps due to the large dispersion difference between the top and bottom waveguides. Increasing the bandgap wavelength of the top waveguide InGaAsP by 1nm decreases the center wavelength of the device by 4.1nm; the corresponding ratio of wavelength shifts for the bottom InGaAsP is 1nm:2.5nm. The growth precision of InGaAsP bandgaps was typically ±10nm.

The device with highest coupling had guides that crossed at 0.3°. The near-field output is shown in Figure 5.6 at the peak wavelength of each channel. The four channels lie at 1482nm, 1498nm, 1517nm, and 1527nm. 2.5mm of the end of the device was cleaved off (total remaining length 9.5mm) because the fourth channel coupling region of the device was not completely bonded, as indicated by the gray oval in Figure 5.3. The fourth channel thus couples much less than the other channels. Figure 5.7 shows a wavelength scan of the OADM throughput and the first three channels. The fourth channel could not be scanned. The high temperature required for device operation aggravated air drafts around the lensed fibers, resulting in noise despite attempts to shield the setup; smoothed data is hence plotted.

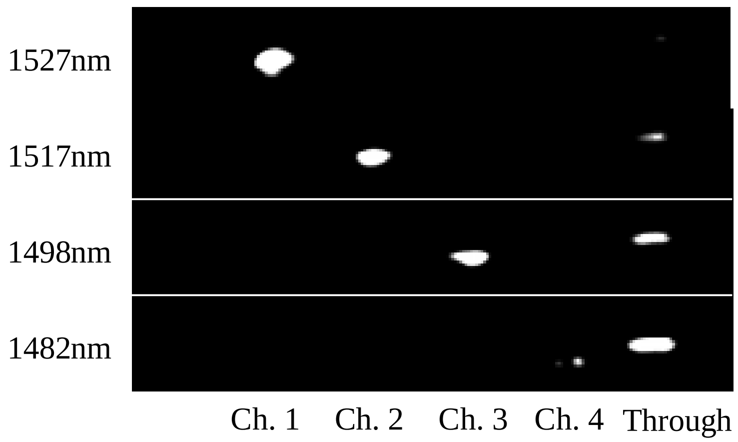

Fig. 5.6 OADM output, captured with IR camera and 80x microscope objective lens.

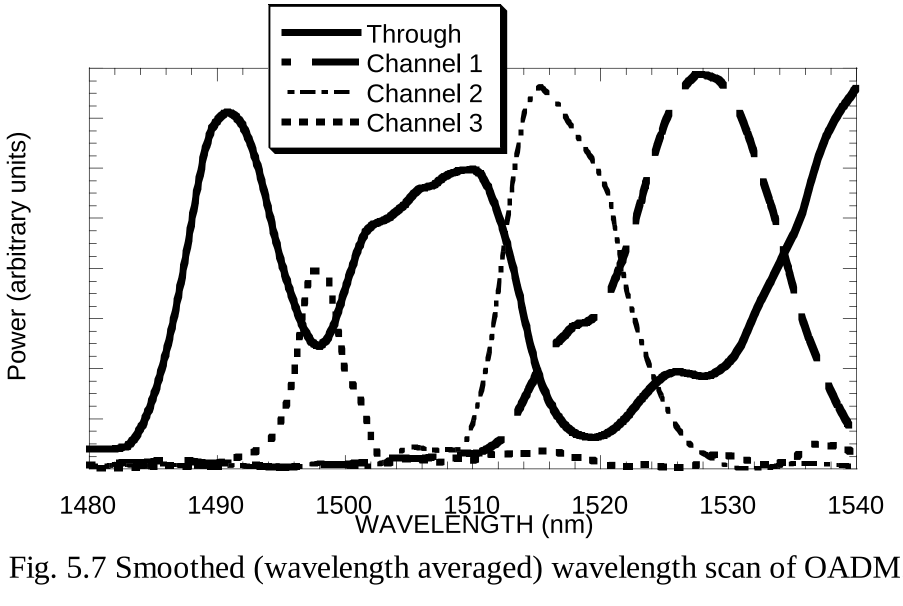

Fig. 5.7 Smoothed (wavelength averaged) wavelength scan of OADM.

The four bottom waveguide widths were chosen such that the four channels would be close in wavelength yet suffer low crosstalk. Though this was not the case for channels 1 and 2 due to the undesirable growth, the crosstalk between channels 2 and 3 was less than –17dB. Increasing the waveguide width differences to allow 20nm channel spacing would give a maximum crosstalk of –15dB for all channels. The bandwidth can be reduced by decreasing the crossing angle, decreasing the thickness of InP between the InGaAsP guiding layers, or using guiding materials with more different dispersion characteristics (e.g. InP/InGaAsP bonded to AlGaAs/GaAs).

82% of channel 1, 93% of channel 2, and 65% of channel 3 are dropped. This device was designed to illustrate the principle that a multiple-channel bonded waveguide OADM could be achieved and was thus not optimized for 100% coupling for each channel. The maximum intensities of all channels can be made equal by using slightly different crossing angles between the in/through waveguide and each add/drop waveguide. The percentage of power dropped can be increased for complete coupling by fine-tuning the crossing angles as well.

The crossing angles of all 4 guides were not fine-tuned for 100% coupling beforehand because of the sensitivity of the device to the growth. The exact waveguide core compositions and thicknesses would have to be known before such a mask could be created. A different mask would be required for each growth. Instead, one mask thought to allow reasonably high (though less than 100%) coupling for several channels over a wider growth range was used.

Another property matching theoretical predictions is stronger coupling for TE polarizations. TE and TM coupling wavelengths were found to differ by 200nm. TM-oriented light resulted in a drop channel intensity 11dB less than that for TE light. The polarization sensitivity results from the strong waveguide geometry asymmetry; large material dispersion differences rather than waveguide dispersion differences (e.g. InP/InGaAsP bonded to AlGaAs/GaAs) could allow TE and TM coupling at the same wavelength.

The fiber-to-fiber device loss was 11.3dB. The in/through waveguide loss was 7.7dB/cm, measured using a Fabry-Perot resonance technique [6].

5.2 Dual-Angle X-Crossing OADM

The design and measurements of the dual-angle X-crossing OADM were primarily performed by Katharina Rauscher from University of Stuttgart. Device fabrication and assistance of design and measurements were performed by the author.

Since large device area was one of the biggest impediments in fabricating the 4-channel OADMs, a means of obtaining shorter devices with equal or better performance was desired. X-crossing waveguides that incorporate bends where the waveguides are further apart, as shown in Figure 5.8, can achieve this. The previously designed X had a crossing angle of 0.3°and a length of 4000μm. The new dual-angle device has a crossing angle of 0.12° for the center 1400μm that changes to a half-angle of 0.38° for the outer 800μm. The total device length was 3000μm, 25%

shorter than the previous X device. A narrower crossing angle where the guides are close together allows most of the coupling to take place with a shorter device length. Broadening the angle between the waveguides where coupling is weaker allows sufficient waveguide separation at the device outputs.

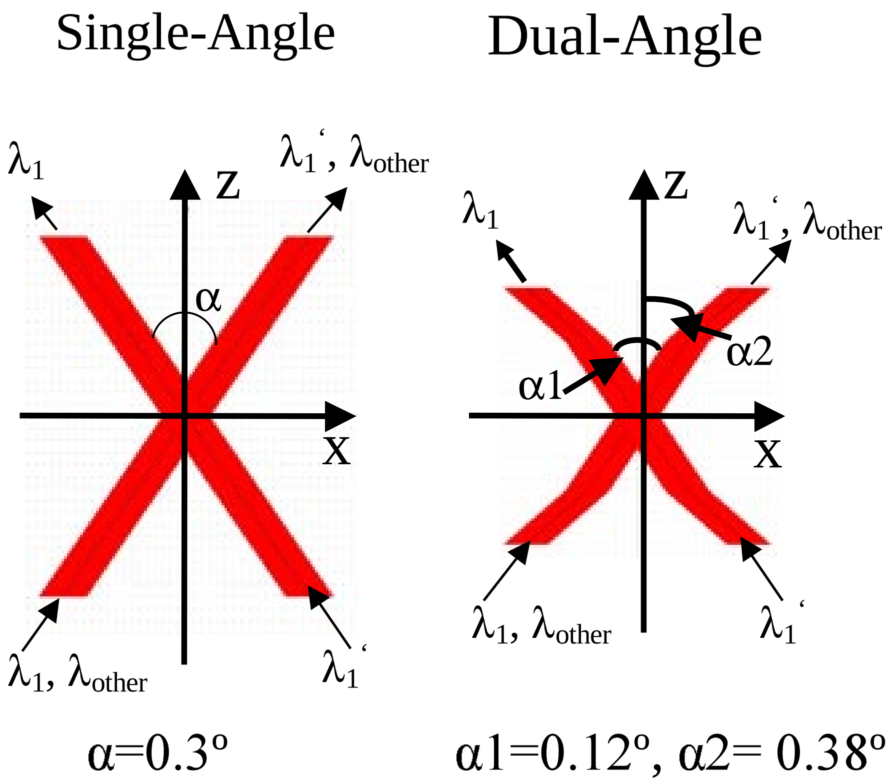

Fig. 5.8 Previous single-angle X-crossing OADM and new dual-angle OADM.

The performance of the device was simulated with BeamPROP™ [7]. A reduction in –20dB bandwidth from 15nm to 12nm was predicted. Sidelobes were simulated to be –16dB rather than –26dB for the previous x-crossing device, however. This was considered to be a small penalty given the 1000-μm device length reduction.

The experimental and theoretical device drop port performance are shown in Figure 5.9. The experiment and theory show good qualitative agreement of null positions.

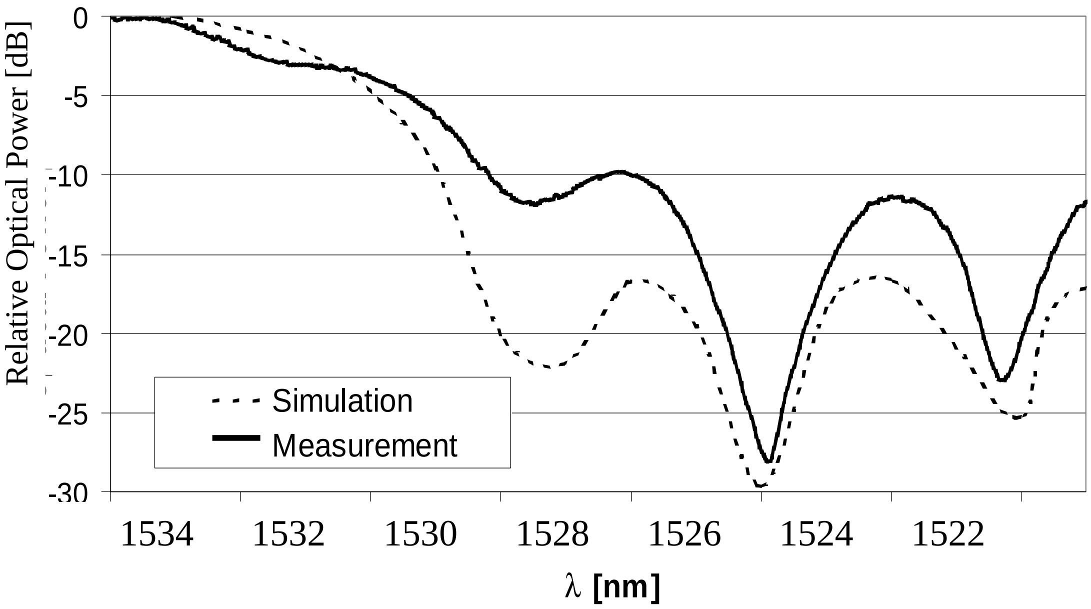

Fig. 5.9 Experimental and theoretical drop port performance of dual-angle x-crossing OADM.

The waveguide "crushing" problem detailed in section 3.2 was observed on the facets of every dual-angle device fabricated. A strain-associated index change may have occurred. This may be responsible for some of the difference between the theory and experiment. Better bonding techniques might reduce the difference.

The growth structure of this device is identical to that of the 4-channel OADM in Figure 5.5 above, but the InGaAsP core bandgap wavelengths were designed to be 1080nm and 1400nm. The actual growth was 1084nm and 1404nm, very close to the desired values. However, this small difference along with simulation inaccuracies due to the large grid spacing required for BeamPROP™ [7] may have further contributed to the discrepancy between theoretical and experimental drop port performance.

Propagation losses for this device were measured to be 1dB/cm [6].

5.3 Truncated Gaussian-Layout OADM

Section 2.2.3 covers the theoretical analysis of improvements to filter bandwidth and sidelobe levels for several novel waveguide layout shapes. From Table 2.1, the Gaussian, Hamming, and modified Blackman were considered to have the best overall performance. OADMs of all three layouts were fabricated and tested. The Gaussian device showed the best performance overall and is examined here in more detail.

The processing of this device incorporated all the techniques used to improve the bond quality. Bonded area yield was roughly 95%. The waveguide “crushing” problem mentioned in section 3.2 was eliminated everywhere except the outermost 1mm of the sample (Fig. 5.10). These bonding non-uniformities may be expected on the outer sample edges from wafer curvature.

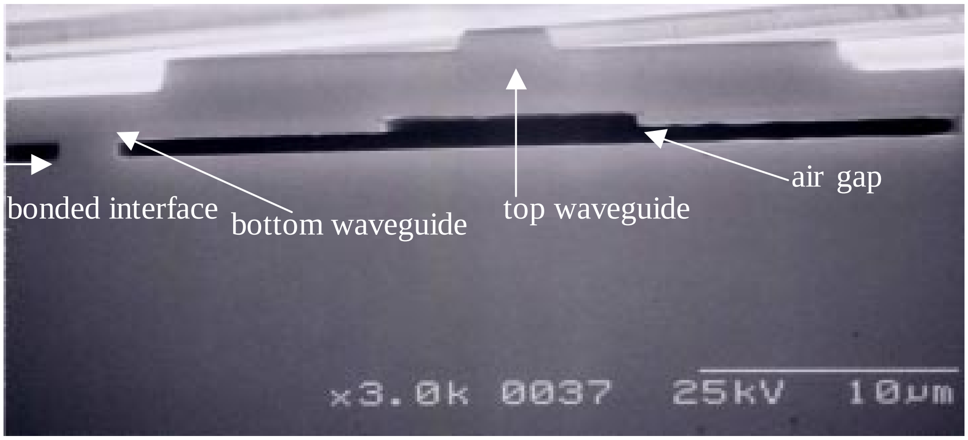

Fig. 5.10 SEM of cleaved output facet of truncated Gaussian-layout device.

All previous devices, save a couple of the dual-angle OADMs, exhibited undesired ripples in the waveguide intensity outputs as a function of wavelength. The periodicity of these ripples varied from 0.2nm to 0.8nm and were up to 20dB in magnitude. The ripples were greatly diminished for all of these Gaussian-layout OADM devices that were bonded to thin host substrates and AR-coated.

The drop and through port performance of the device with the highest coupling is shown in Figure 5.11. The –20dB bandwidth of the measured data is 28.8nm, over twice as wide as the 12.5-nm –20dB bandwidth predicted from the integration of the coupled-mode equation (Table 2.1).

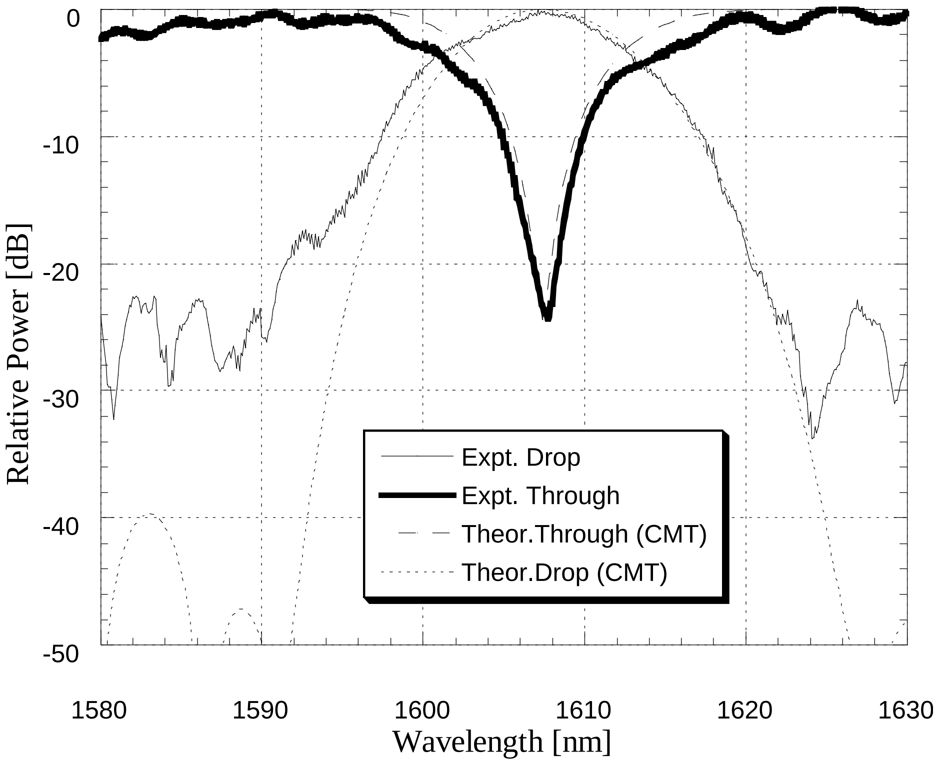

Fig. 5.11 Experimental and theoretical drop and through waveguide outputs vs. wavelength.

The desired and actual growths are shown in Fig. 5.12. All layer thicknesses were bigger than those desired. The coupling of the device is particularly sensitive to the thicknesses of the InGaAsP cores and the center InP between the cores. The larger thicknesses translate to tighter mode confinement in the cores and greater separation of the modes, both of which lead to reduced modal overlap and weaker coupling. This shift in thicknesses (and the bandgap wavelength shift of the lower-index InGaAsP) is likely the cause of the bandwidth broadening and shift in filter center from 1550nm to 1606.75nm.

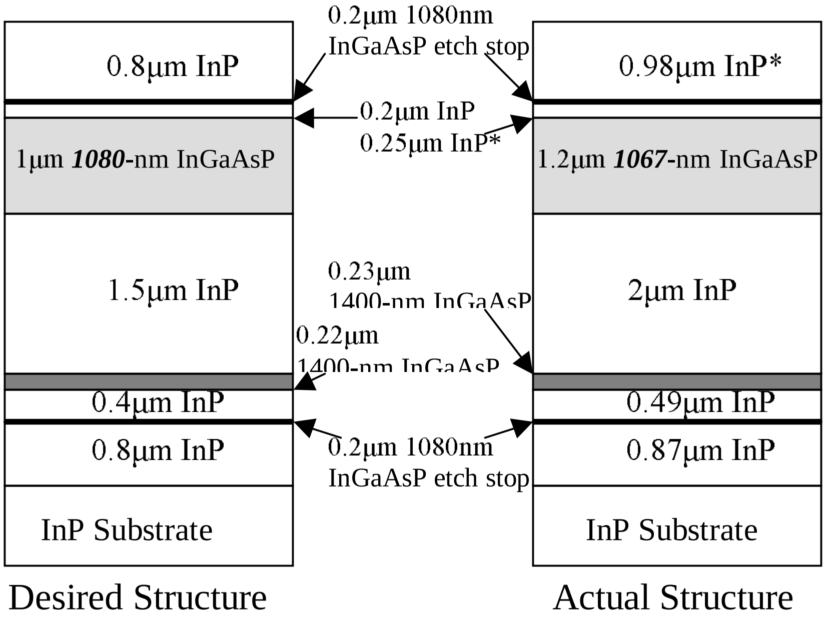

Fig. 5.12 Desired vs. actual growths, post-bond. *Top two InP layer thicknesses of actual structure are estimates. They were etched down to 0.83μm and 0.1μm for the working device.

The performance of the device with the above actual structure was simulated using the finite difference technique (FDT) and coupled mode theory (CMT). The final top and bottom waveguide widths were measured to be 2.4μm and 1.8μm, respectively, from SEM pictures. The top two InP layer thicknesses shown in Fig. 5.12 are estimates. Both of the top two layers were dry etched approximately 0.15μm (right after the device processing was initially completed) because the top waveguide did not support a guided mode when the device was first tested. The top waveguide ridge of the final operational device was dektaked to be 0.83μm and the top waveguide cladding was measured from the SEM picture of a stain-etched facet to be roughly 0.1μm.

CMT simulations show that the light is coupling from input gui

de to output guide one time instead of three times, as the device was designed. This is probably the reason for the broadening of device bandwidth. The Fourier transform of the drop port experimental data was taken to determine the coupling coefficient along the device length [8, 9]. The coupling coefficient versus waveguide separation as determined from the experimental data is shown in Figure 5.13. Also included for comparison are the theoretical coupling coefficients of the desired structure (three times coupling), for a range of high-index InGaAsP bandgaps. Figure 5.13 confirms that the coupling in the device is much weaker than that required for three times coupling from input to output.

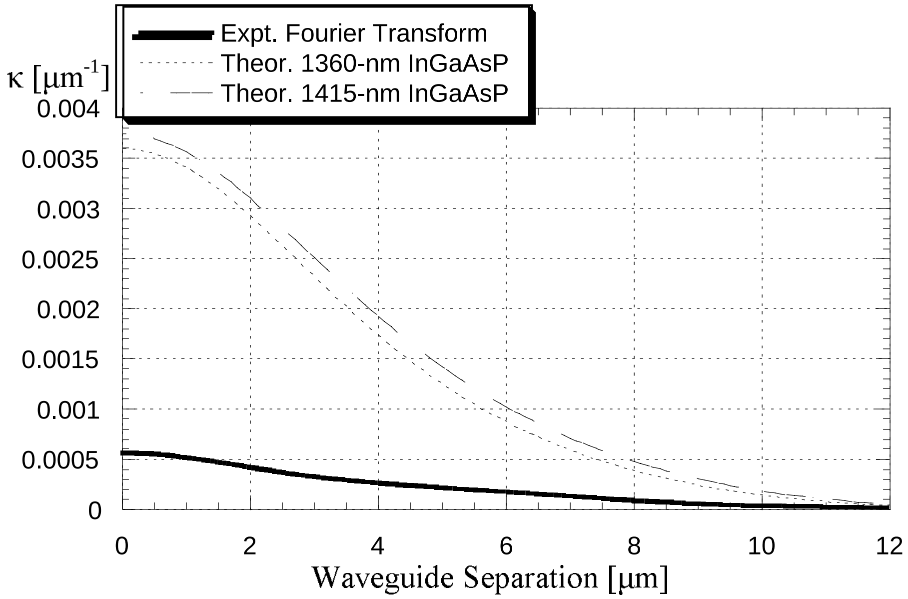

Fig. 5.13 Coupling coefficient κ vs. waveguide separation. Experimental κ was determined through a Fourier transform of the data in Fig. 5.11. Theoretical values were for desired growth (with slight alteration to the high-index InGaAsP bandgap) calculated using the FDT and CMT.

This device has the highest coupling efficiency of any InP vertically coupled waveguide device ever made at UCSB (99.4% versus 97%)[5]. The previous vertically coupled waveguide device effort at UCSB did include an OADM with lower sidelobe levels (-26dB), however [5].

Propagation losses for this device were measured to be 1.1dB/cm [6]. The fiber-to-fiber device loss was 11dB.

5.4 Summary

Three InP/InGaAsP vertically coupled near-parallel waveguide OADM devices were designed and tested. A multiple channel X-crossing OADM was demonstrated but suffered a low yield from device length. 25% shorter OADMs were then made by including additional waveguide bends. In an investigation of waveguide shapes for optimal performance, a Gaussian layout provided the best results. Though a high coupling ratio was achieved, the theoretical 12.5nm –20dB half-width and sidelobes of less than –30dB were not witnessed experimentally. This was probably because the refractive indices of the InGaAsP cores deviated significantly from the desired values. Further work with the devices in this chapter would strongly benefit from higher growth precision as well as an analysis of the waveguide bonding effects on the bandgaps.

References:

[1] H. Mavoori, S. Jin, R. P. Espindola, and T. A. Strasser, "Enhanced thermal and magnetic actuations for broad-range tuning of fiber Bragg grating-based reconfigurable add-drop devices," *Optics Letters*, vol. 24, pp. 714-716, 1999.

[2] C. R. Doerr, L. W. Stulz, J. Gates, M. Cappuzzo, E. Laskowski, L. Gomez, A. Paunescu, A. White, and C. Narayanan, "Arrayed waveguide lens wavelength add-drop in silica," *IEEE Photonics Technology Letters*, vol. 11, pp. 239-241, 1999.

[3] B. J. Offrein, G. L. Bona, F. Horst, W. M. Salemink, R. Beyeler, and R. Germann, "Wavelength tunable optical add-after-drop filter with flat passband for WDM networks," presented at IEEE Optical Fiber Communication Conference and the International Conference on Integrated Optics and Optical Fiber Communications, 1999.

[4] B. Liu, "Three-Dimensional Photonic Devices and Circuits," in *Electrical and Computer Engineering*. Santa Barbara: U. C. Santa Barbara, 2000.

[5] B. Liu, Shakouri, A., Abraham, P., Bowers, J. E., "Optical add/drop multiplexers based on X-crossing vertical coupler filters," *IEEE Photonics Technology Letters*, vol. 12, pp. 410-412, 2000.

[6] K. H. Park, M. W. Kim, Y. T. Byun, D. Woo, S. H. Kim, S. S. Choi, Y. Chung, W. R. Cho, S. H. Park, and U. Kim, "Nondestructive propagation loss

and facet reflectance measurements of GaAs/AlGaAs strip-loaded waveguides," *Journal of Applied Physics,* vol. 78, pp. 6318-6320, 1995.

[7] "BeamPROP, Version 4.0,".: Rsoft, Inc., 2001.

[8] H. Kogelnik, "Filter Response of Non-Uniform Almost-Periodic Structures," *Bell. Syst. Tech. J.,* vol. 55, pp. 109-126, 1976.

[9] R. C. Alferness and P. S. Cross, "Filter Characteristics of Codirectionally Coupled Waveguides with Weighted Coupling," *IEEE Journal of Quantum Electronics,* vol. QE-14, pp. 843-847, 1978.

Chapter 6

Conclusions and Future Work

6.1 Summary

The development of 3D PICs is a critical direction for the advancement of powerful and compact optoelectronics. One way to achieve 3D routing of light is through wafer bonded waveguide couplers. Several vertically coupled wafer-bonded InP/InGaAsP waveguide devices have been demonstrated in this work.

A 3-layer 1:8 beam splitter was realized. It was over 100 times shorter than an equivalent 2D splitter with a minimum waveguide spacing of 1μm. To the best of our knowledge, this is the first ever vertically coupled optical device of more than two waveguide layers.

A multiple-channel X-crossing OADM was demonstrated. This device had no simple 2D equivalent. This device was also one of the first vertically coupled waveguide OADMs ever reported with spatial separation of more than one add/drop channel.

Multiple waveguide layout shapes were analyzed through an integration of the coupled-mode Ricatti equation. Such an analysis had never been previously published for vertically coupled waveguide devices. A truncated Gaussian layout was found to give the best theoretical performance. The fabricated truncated Gaussian layout device achieved the highest coupling ratio ever for the UCSB InP vertically coupled waveguide effort. Ripples in the light intensity versus wavelength scans present for all previous devices were finally eliminated with these Gaussian layout devices as well.

The work described above complements the general progress of the field of vertically coupled waveguide devices. While this work demonstrates generally novel waveguide layouts and numbers of vertical layers, other groups have made great strides with filtering device switching and tunability. For example, tunable vertically coupled asymmetric waveguide grating OADMs have been demonstrated through InP MOCVD regrowths [1]. Vertically coupled InP micro-disk electro-absorptive switches have been recently created with wafer bonding [2]. The work performed in this work could be combined with the switching and filtering techniques developed by outside groups for further functionality.

An investigation of bonding techniques has also been performed in this work. Wafer bonding technology is still far from maturity. Large-scale implementation of PICs with devices like the ones in this work will not be practical without better bonding technology and higher-quality wafers. It is too early to predict whether direct-contact wafer bonding of III-Vs, and III-Vs to other materials, will ever be used commercially for entire multi-layer PIC chips and large non-hero devices. This development may occur in the next couple of decades as general semiconductor technologies continue to progress. A patient, thorough investigation of optimal pressures for bonding thinner, more membrane-like samples of superior surface morphology appears most likely to lead to success.

A reasonably high and reproducible bonded area yield of 95% was achieved for the 3-cm^2 InP samples. There are many drawbacks to bonding, such as the 5% of material that does not bond, extra processing steps, and difficulty of through-the-epitaxial-layer alignment during photolithography. However, the present yield is high enough that wafer bonding remains an attractive investigative technology for small-scale device integration. This is particularly true for novel devices that are not practical to fabricate without wafer bonding.

The biggest challenge with the devices in this work was not the bonding, but rather the lack of control over the InGaAsP core material. To further develop filtering waveguide devices strongly dependent on dissimilar material composition, more precise control of the core bandgaps and thicknesses is essential. For the OADMs discussed in Chapter 5, InGaAsP bandgap wavelength control to within ±0.5nm and thickness control to within 1% would be required for >99% coupling at the desired wavelength. These are serious limitations that render these devices impractical for growth in many reactors used today. In-situ monitoring of growth would aide strongly in achieving these restrictive parameters, though. In-situ monitoring was not available with the horizontal MOCVD reactor used for the growths. Fortunately, though, it is commonly available with vertical reactors.

Devices less sensitive to growth parameters are essential for continuation of this work. It may be easier to achieve the correct refractive indices by using materials other than InGaAsP. Ternary compounds (or binary if possible) may allow more control over the growth indices. Such materials will suffer from fluctuations of fewer elements during growth. InP/InGaAs waveguides could be vertically coupled to waveguides of GaAs/AlGaAs or Si/SiO_2. If more than one combination of compounds can be used, the degree of refractive index fluctuation likely for each material should also be taken into account.

The devices analyzed in this work are not suitable for dense wavelength division multiplexing (DWDM), but rather a much coarser technology. For these long waveguide devices, it would be very difficult to achieve such fine wavelength

sensitivity through material and waveguide dispersion effects alone. DWDM performance may be achieved by incorporating compact micro-resonators or gratings, as suggested for future work.

6.2 Future Work

Masks with large devices can still suffer low *device* yields despite high *bonded area* yields. Until near-100% bonding can be achieved reliably, smaller devices are better suited for this technology. Micro-resonators are an example of a type of device that enjoy many benefits from wafer bonding. Not only are micro-resonators very small, but vertical coupling generally provides superior device performance [3]. Also, the free spectral range of such devices can be greatly increased by combining waveguides of different materials [4].

Bonding of different materials together to get 3D PICs with enhanced functionality is one of the most exciting directions in which to take this research.

Silicon optoelectronics is very promising as a platform for future very large scale integration (VLSI) photonic devices. Lasers, light-emitting diodes (LEDs), detectors, modulators, switches, and gain regions could be included on silicon PICs through the bonding of other materials such as InP and GaAs. Materials with desirable bandgaps can thus be combined with inexpensive, compact, high index contrast, low-loss Si waveguide devices for superior performance. For example, the direct integration of multiple lasers of different wavelengths with a Si arrayed waveguide grating (AWG) multiplexer would be much less costly than coupling all the lasers to fibers individually. A complete integration of emitting, modulating, routing, and detecting devices could be achieved on one chip.

If better control over the InGaAsP growth bandgaps could be achieved, the performance of the OADMs discussed in Chapter 5 would significantly improve. Further enhancements to the OADMs would also become feasible. For example, the multiple-channel X-crossing OADM would benefit greatly from wavelength tunability. The carrier injection effect was simulated to allow channel tuning of over 10nm with the structure below (Fig. 6.1) [5]. One of the difficulties worth noting with such a design is migration of p-dopants during the growth and bonding steps. SIMS analyses have shown that Zn dopant may migrate to the InGaAs and InGaAsP layers when several microns of material are grown above the p-type layers.

A grating could be added to enhance the tuning range. Gratings would also be useful for narrowing the device bandwidth of both tunable and passive OADMs.

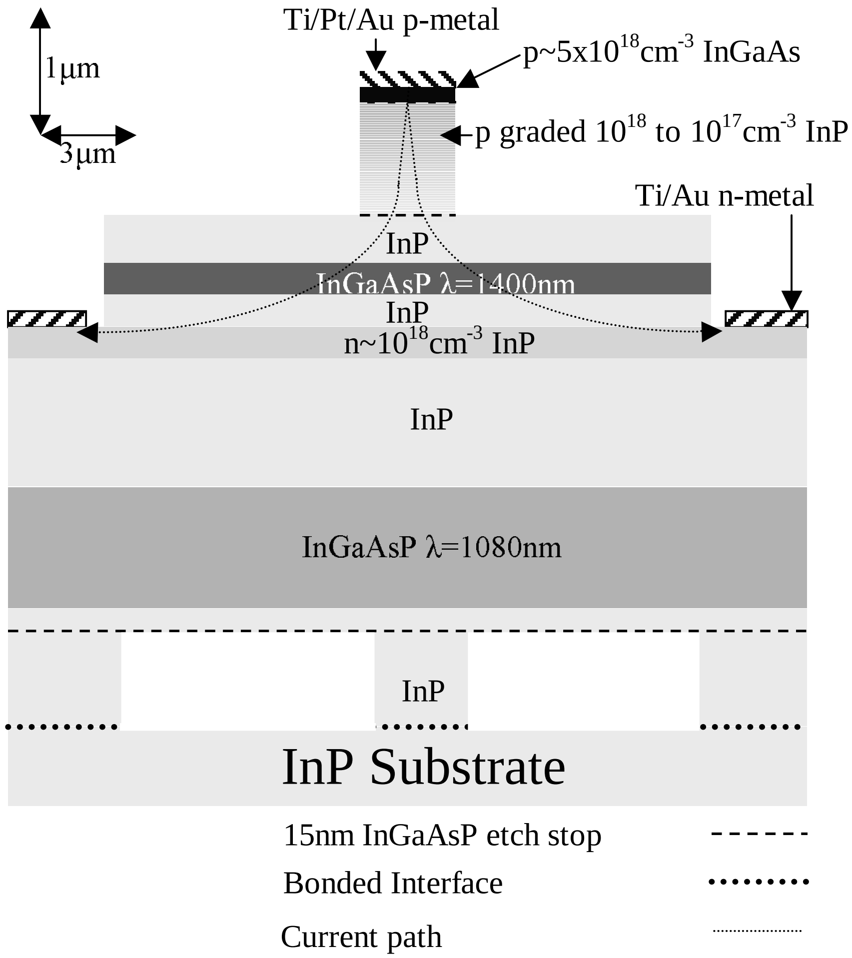

Fig. 6.1 Cross-sectional view and structure of tunable OADM.

Another valuable enhancement to the OADMs only practical with very precise growth control is polarization-independent operation. One means of achieving this through a cascaded-OADM scheme is outlined in [6]. This device would be particularly sensitive to growth indices because the two OADMs must have precisely matched add/drop wavelengths. Electrodes to tune the OADMs' add-drop wavelengths would probably be necessary.

Another direction to be investigated is the transformation of the 3-layer beam splitter into a demultiplexer by exploiting the wavelength dependence of the coupling. Couplers can be chosen to have lengths such that each channel is split to a unique output waveguide [6]. An improvement of the waveguide alignment will be essential for good device performance, however. One technique for better alignment is the use of a stepper aligner in conjunction with a method of etching align marks through the epitaxial layer [7].

All of the devices in this work except the multi-channel OADM incorporated s-bends to laterally separate the waveguides at the inputs and outputs. Lateral waveguide separation could be achieved with a shorter device length if total internal reflection (TIR) mirrors were used instead. TIR mirrors can be fabricated by etching through the waveguide cores to form smooth, near-vertical facets [8]. S-bend length could also be reduced if the waveguide were more deeply etched in the s-bend regions to allow smaller radii of curvature. The smallest radii of curvature would be achieved with “floating” s-bends for which all material adjacent to the waveguide has been removed.

References:

[1] M. Horita, T. Yazaki, S. Tanaka, and Y. Matsushima, "Extension of Operation Range of Semiconductor Optical Add-Drop Multiplexer," presented at 2001 International Conference on Indium Phosphide and Related Materials, Nara, Japan, 2001.

[2] K. Djordjev, S.-J. Choi, S.-J. Choi, and P. D. Dapkus, "Vertically Coupled InP Microdisk Switching Devices with Electroabsorptive Active Regions," *IEEE Photonics Technology Letters*, vol. 14, pp. 1115-1117, 2002.

[3] D. V. Tishinin, I. Kim, C. Lin, A. E. Bond, and P. D. Dapkus, "Novel fabrication process for vertical resonant coupler with precise coupling efficiency control,",, 1998.

[4] C. Ozturk, Y. J. Chiu, and N. Dagli, "Polymer/compound semiconductor hybrid micro resonators with very wide free spectral range," presented at Lasers and Electro-Optics Society 2002, 2002.

[5] B. R. Bennett, R. A. Soref, and J. A. Del Alamo, "Carrier-Induced Change in Refractive Index of InP, GaAs, and InGaAsP," *IEEE Journal of Quantum Electronics*, vol. 26, pp. 113-122, 1990.

[6] B. Liu, "Three-Dimensional Photonic Devices and Circuits," in *Electrical and Computer Engineering*. Santa Barbara: U. C. Santa Barbara, 2000.

[7] P. P. Absil, J. V. Hryniewicz, B. E. Little, F. G. Johnson, K. J. Ritter, and P.-T. Ho, "Vertically coupled microring resonators using polymer wafer bonding," *IEEE Photonics Technology Letters*, vol. 13, pp. 49-51, 2001.

[8] G. Fish, "InGaAsP/InP Based Photonic Integrated Circuits for Optical Switching," in *Electrical and Computer Engineering*. Santa Barbara: University of California, Santa Barbara, 1999.

Appendix A: MATLAB Programs

The following programs are included on the data disks filed with the thesis.

EITTMM

The effective index technique and transfer matrix method are used to plot the effective indices of top and bottom waveguides as a function of wavelength.

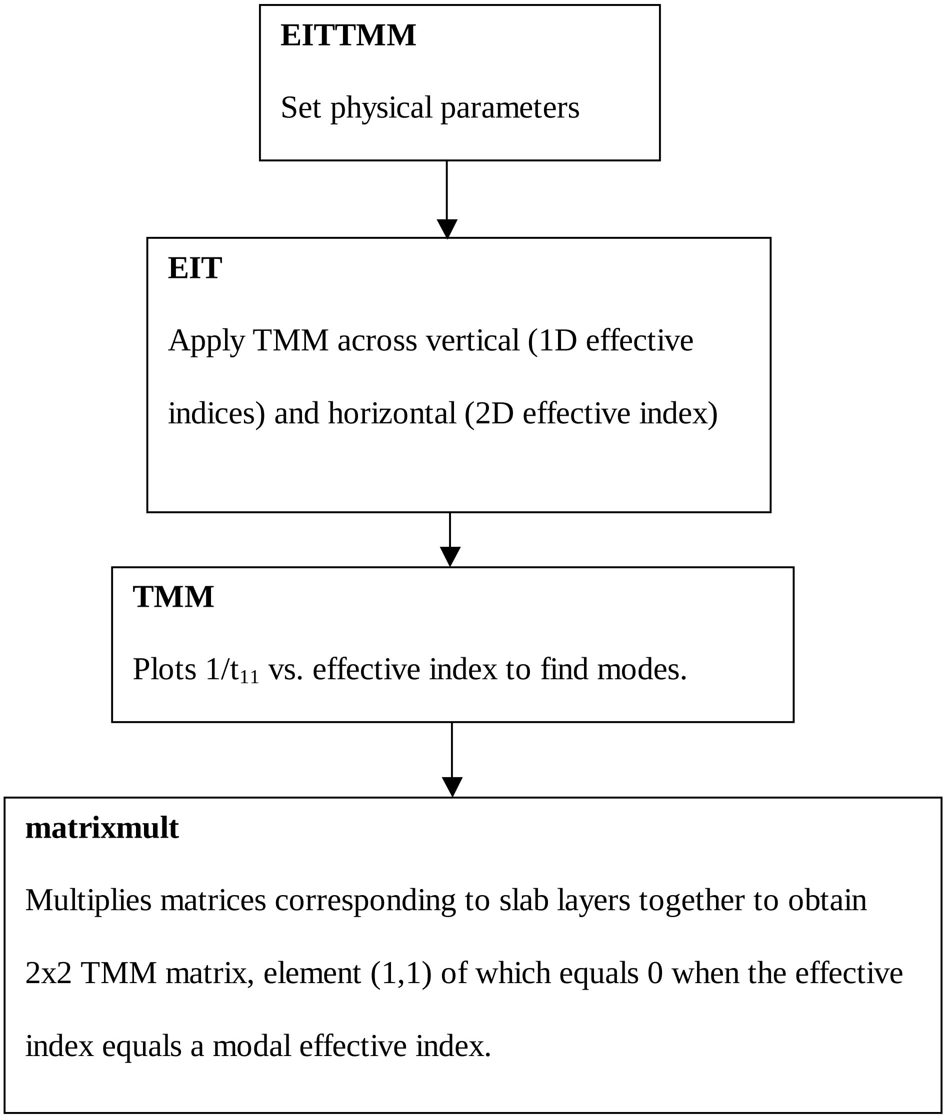

EITTMM

Set physical parameters

EIT

Apply TMM across vertical (1D effective indices) and horizontal (2D effective index)

TMM

Plots $1/t_{11}$ vs. effective index to find modes.

matrixmult

Multiplies matrices corresponding to slab layers together to obtain 2x2 TMM matrix, element (1,1) of which equals 0 when the effective index equals a modal effective index.

FDTCMT

The finite difference technique and coupled mode theory are used to plot terms proportional to power in each guide as a function of distance or wavelength.

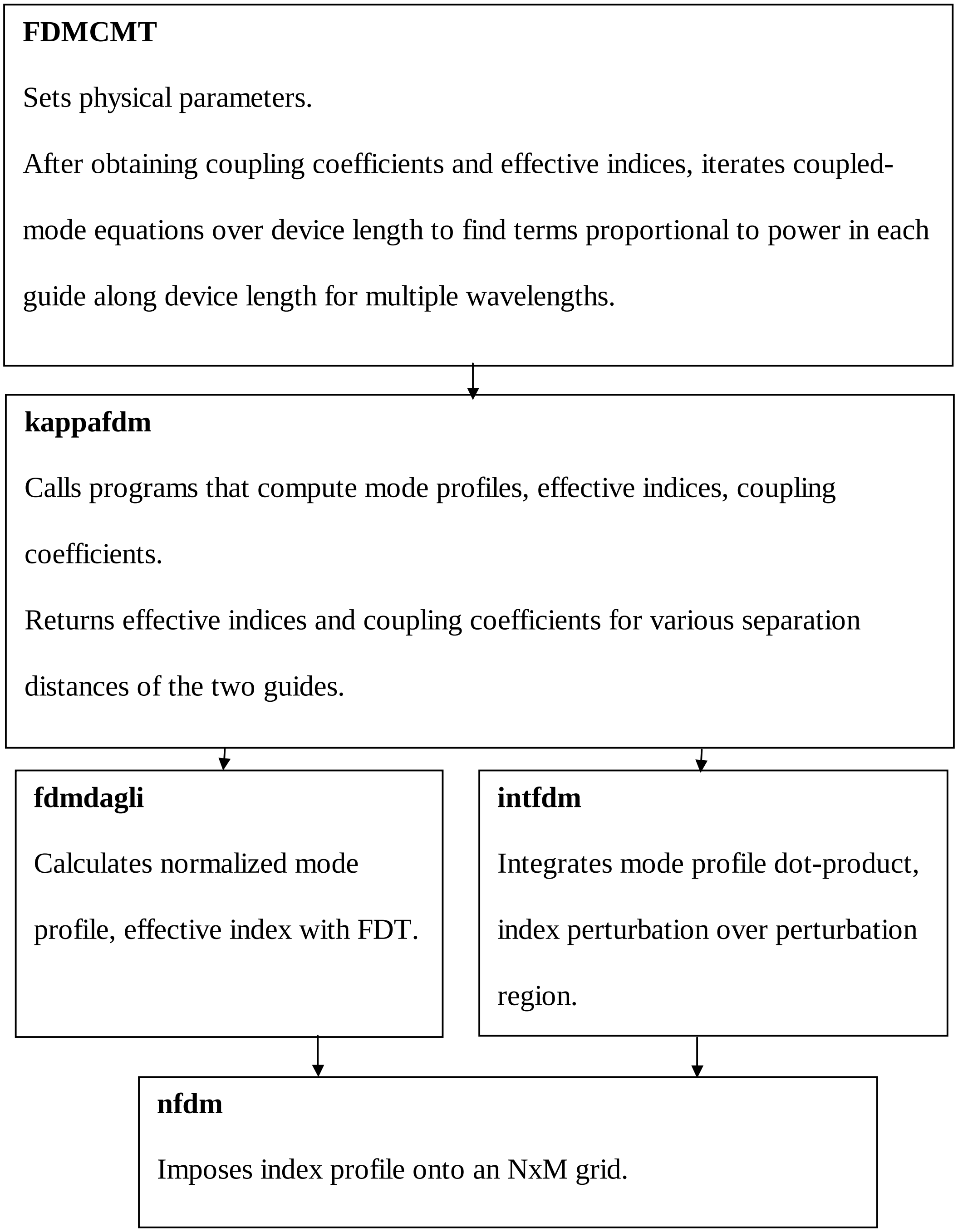

FDMCMT

Sets physical parameters.

After obtaining coupling coefficients and effective indices, iterates coupled-mode equations over device length to find terms proportional to power in each guide along device length for multiple wavelengths.

kappafdm

Calls programs that compute mode profiles, effective indices, coupling coefficients.

Returns effective indices and coupling coefficients for various separation distances of the two guides.

fdmdagli

Calculates normalized mode profile, effective index with FDT.

intfdm

Integrates mode profile dot-product, index perturbation over perturbation region.

nfdm

Imposes index profile onto an NxM grid.

RK, RKmisalign*, RKmisrot*, RKmisstruct*, RKx*

Given taper function w, and assuming coupling coefficient is constant with respect to wavelength, performs 4th order Runge-Kutta integration of single non-linear Ricatti coupled-mode equation to plot drop port power vs. deviation from center wavelength.

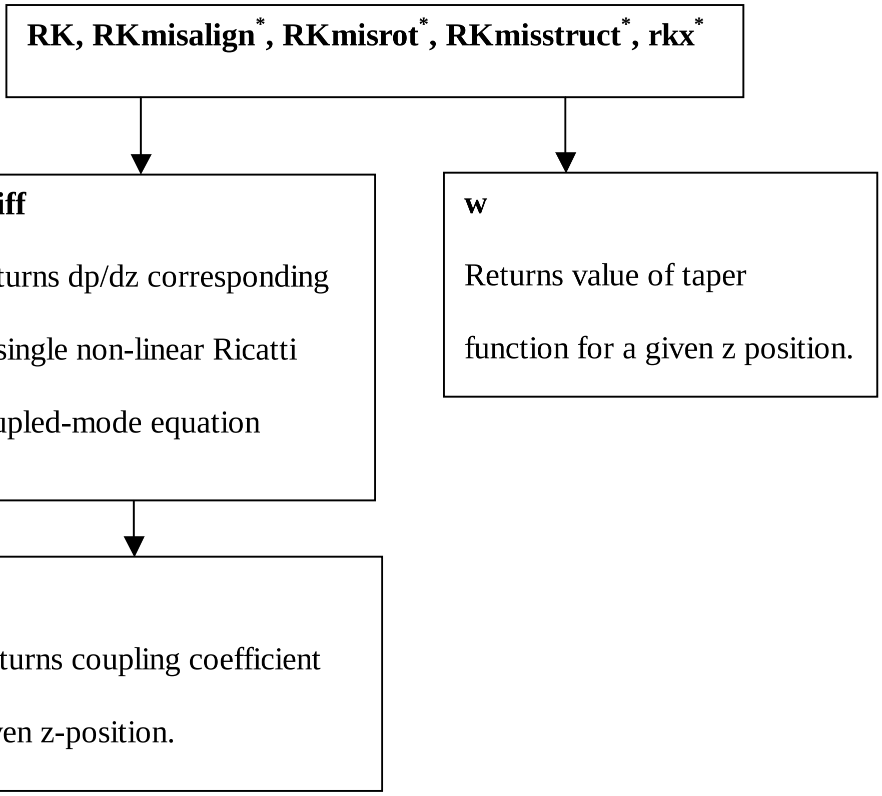

RK, RKmisalign*, RKmisrot*, RKmisstruct*, rkx*

pdiff

Returns dp/dz corresponding to single non-linear Ricatti coupled-mode equation

w

Returns value of taper function for a given z position.

K

Returns coupling coefficient given z-position.

***RKmisalign** uses coupling coefficient values calculated previously to plot for various lateral mask misalignments.

***RKmisrot** uses coupling coefficient values calculated previously to plot for rotational mask misalignment.

***RKmisstruct** solves for coupling coefficient as a function of propagation distance z given growth mistakes to plot for non-ideal growth structure. It also calls **kappafdm**, which calls **fdmdagli** and **intfdm**, which both call **nfdm**, as with the **FDMCMT** program above.

***RKx** uses coupling coefficient values calculated previously to plot for x-crossed waveguides. It does not call **w**.

Fourier, Fourierx*

Solves Fourier transform relation (assumes low coupled power) of Ricatti coupled-mode equation to determine drop port power vs. deviation from center wavelength for various waveguide shapes w.

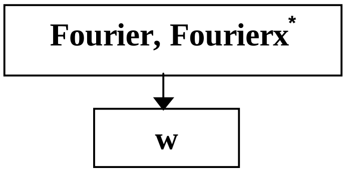

***Fourierx** solves for the case of x-crossed straight waveguides and does not call **w**.

Appendix B: Processing Procedures

Processing for all devices is similar. Samples are cleaved, patterned with SiN-masked photolithography and wet or dry etched, and wafer bonded. The growth substrate is removed, followed by more patterning and etching. Finally, the waveguide facets are cleaved and anti-reflection (AR) coated. Photolithography is covered in appendix B. Wet and dry etches are covered in Appendix C. A detailed description of the wafer bonding process is given in Appendix D. Some useful miscellaneous processing techniques are described in Appendix E.

3-Layer Beam Splitter

1. Cleave one sample from bottom-layer wafer 1.2cm (perpendicular to major flat, parallel to waveguides) x 1.0cm, solvent clean.
2. Deposit 1400Å SiN on bottom layer with PECVD.
3. Mask 1 photolithography: Shipley 4110, O_2/CF_4/remove resist.
4. RIE etch 0.1μm InP plus 0.5μm InGaAsP (~12 min), dektak.
5. Clean, fuse to newly cleaved middle layer sample. (Same as Appendix D except between buffered HF dip and transportation of samples to bonding furnace, a 30 minute ozone oven bake is performed.) 0.5lbf·in torque used.
6. Mount sample bottom-layer-down on glass slide with crystal wax.
7. Remove substrate, remove sample from slide, remove InGaAs etch stop.
8. Repeat 2~5 for middle layer waveguides. Use IR aligner to view align marks.

9. Clean, fuse to newly cleaved top layer sample as in 6.
10. Repeat 2~5 for top layer waveguides, but etch 0.9μm InP and 0.5μm InGaAsP. IR aligner is used to view buried align marks.
11. Cleave by hand.

4-Channel X-Crossed OADM

1. Cleave one sample 1.7cm (parallel to waveguides) x 1.4cm, solvent clean.
2. Deposit 1400Å SiN with PECVD.
3. Mask 1 photolithography: Shipley 4110, O_2/CF_4/remove resist.
4. RIE etch 0.7μm InP, dektak, sidewall smooth wet etch for remaining 0.1μm.
5. Deposit 1400Å SiN.
6. Mask 2 photolithography: Shipley 5214, O_2/CF_4/remove resist.
7. Wet etch etch stop, 0.4μm InP, 0.22μm InGaAsP, dektak.
8. Clean, fuse patterned sample to newly cleaved host sample. (Same as Appendix D procedure except between buffered HF dip and transportation of samples to bonding furnace, a 30-min ozone oven bake is performed.) 0.5lbf·in torque used.
9. Mount on microscope slide host-substrate-down with crystal wax.
10. Remove substrate, remove sample from slide, remove InGaAs etch stop.
11. Repeat steps 2~6 with masks 3 and 4, using IR camera for mask 3.
12. RIE etch 0.2μm InP, 1-μm thick InGaAsP.
13. Cleave by hand.

Gaussian-layout OADM

1. Cleave one sample 1.8cm (parallel to waveguides) x 1.6cm, solvent clean.
2. Deposit 1000Å SiN with PECVD.
3. Mask 1 photolithography: Shipley 4110, O_2/CF_4/remove resist.
4. RIE etch 0.7μm InP, dektak, sidewall smooth wet etch for remaining 0.1μm.
5. Deposit 1000Å SiN.
6. Mask 2 photolithography: Shipley 5214, O_2/CF_4/remove resist.
7. Wet etch etch stop, 0.4μm InP, 0.22μm InGaAsP.
8. Fuse according to Appendix D, torque=0.45lbf·in.
9. Mount on microscope slide host-substrate-down with crystal wax.
10. Remove substrate, remove sample from slide, remove InGaAs etch stop.
11. Repeat steps 2~6 with masks 3 and 4, using IR camera for mask 3.
12. RIE etch 0.2μm InP, 1μm InGaAsP.
13. Cleave by hand.
14. AR-coat both facets: E-beam deposit SiO at 3~5Å/s, total thickness ~2550Å.

Solvent clean=3 squirts acetone, 3 squirts isopropanol moved to fresh spot on cleanroom wipe each time, blow with N_2 afterwards holding sample at angle so that isopropanol leaves surface as a sheet rather than beading.

O_2/CF_4/remove resist=oxygen plasma descum (25s, 100W, 300mT), CF_4 plasma etch (75s for 1400Å SiN or 60s for 1000Å SiN, 100W, 300mT), solvent clean.

Appendix C: Photolithography

All masks are light field for ease of viewing the sample. Contact aligners were used because all mask features were at least 2μm. The spinner chuck is cleaned with acetone before use for proper sample adherence and to prevent photoresist from being deposited on the back of the sample. Any photoresist on the backside of the sample is removed with an acetone-soaked q-tip to ensure the sample sits flat during mask alignment.

1. Solvent clean, bake samples on 110˚C hot plate 2 minutes.
3. Blow with N_2 while spinning sample at 6000rpm.
4. Drop 2~3 drops hexamethyldisilazane (HMDS), let sit 15s, then spin at 6000rpm 1min.
5. Drop 2~3 drops Shipley 4110 or 5214 in center of sample, immediately spin at 6000rpm 1 min.
6. Bake 90s at 95˚C.
7. Align sample to edge bead mask with ~1mm overhanging mask edge on Karl Suss aligner, expose 1min.
8. Develop edge bead in 1:4 AZ400-K: H_20 1min.
9. Align sample to waveguide mask, soft contact
    a. IR photolithography requires double-side polished samples and backside illumination for alignment within 0.5μm.
10. Expose, develop, bake:

a. 4110 resist (used for waveguide definition)
    i. Expose 8.5s at 7.5mW/cm^2, develop in 1:4 AZ400-K: H_20 for 5s after development visually complete, bake at 105˚C 1min.
b. 5214 resist (used for definition of narrow sidelobe-suppression trenches)
    i. Expose 17s with blue filter at 7.5mW/cm^2, bake at 105˚C 1min, flood expose 1min with blue filter, develop in 1:5.5 AZ400-K: H_20 for 5s after development visually complete.

Appendix D: Dry and Wet Etches

Wet etching is used instead of dry etching wherever possible because of the speed and convenience, particularly on device trial runs. Chemical etchants can be mixed up and brought to the desired temperature within ten minutes. Reactive ion etching (RIE) can require up to an hour in chamber cleaning, priming, and pump-down time.

If waveguides are straight and oriented perpendicular to the major flat of the wafer, in the [110] direction, near-vertical InP sidewalls with HCl/H_2O etches are possible. HCl etching was used for all [110]-oriented waveguides in the previous PIC efforts at UCSB [1]. However, it was found that even when the waveguides are oriented correctly, an HCl/H_2O etch may slightly over-etch laterally. Etching all but the last 1000Å with H_3PO_4/HCl and following with a brief HCl/H_2O etch were found to prevent lateral over-etching, but were difficult to control given the very short etch times. For fabrication of sensitive devices, RIE etching was used instead. Dry etching is also required to create waveguides and trenches after wafer bonding to avoid trapping of acids in the air gaps between the bonded layers.

InP Wet Etching:

InGaAsP and InGaAs serve as etch stops for all InP wet etching.

2:1 HCl:H_20 etches roughly 750Å per second at room temperature and is used for etching InP waveguides and cladding, and for the 10s post-RIE bottom waveguide sidewall smooth etch.

3:1 HCl:H_20 is used for InP substrate removal. Removal of 350~375-μm substrates requires roughly 50~70min.

InGaAsP and InGaAs Wet Etching:

InP serves as an etch stop for all InGaAsP and InGaAs etching.

1:1:10 H_2SO_4:H_2O_2:H_2O is used to etch InGaAs and InGaAsP of bandgap wavelength 1.3μm or higher. The H_2O_2 is added only after the H_2SO_4 and H_2O have been mixed and allowed to cool. 1min is plenty for the 0.2-μm InGaAs etch stops. This etch etches InGaAsP of bandgap wavelength ≥1.3μm roughly 1000Å/min.

Removing InGaAsP with bandgap wavelengths of 1.1μm or lower was not straightforward because all attempted etchants, including many ratios of H_2SO_4:H_2O_2:H_2O (1:1:10, 4:1:1, 10:1:1, 1:8:1), etched these compositions very slowly. In many cases, the SiN mask was critically damaged before all of the 1.1-μm InGaAsP was removed. Dry etching was used instead. However, the 15-nm thick 1.1μm InGaAsP etch stops were thin enough to be etched away in 1:1:10 H_2SO_4:H_2O_2:H_2O in 30s.

$CH_4/H_2/Ar$ RIE Etching:

A 980-nm laser is used as a monitor because etch rates vary greatly. One period of the monitor output corresponded to 1420nm of etched InP. Samples etch more quickly near the edges and must be surrounded by scrap InP to reduce non-uniform etching. Even with this precaution, etch depths near sample edges are typically 10 to 20% greater than those near the sample center. Dry etching of waveguides is performed to within 1000Å of the desired height in the sample center and any remaining InP is removed with a sidewall-smoothing wet etch. Polymer deposits can be a problem with $CH_4/H_2/Ar$ etching, but are alleviated with shorter etches, thoroughly removing photoresist from samples beforehand, and thoroughly cleaning the inside of the chamber with isopropanol and oxygen plasma before using. Sometimes for long etches, a 3-min polymer clean was used every 10min of etching to prevent polymer build-up.

Processing Step	Gas	Flow [sccm]	Voltage [V]	Pressure [mT]	Duration [min]
Chamber Clean	O_2	20	500	125	20~40*
Chamber Precoat	$CH_4/H_2/Ar$	4/20/10	500	75	10
Etch	$CH_4/H_2/Ar$	4/20/10	500	75	Varies**
Descum	O_2	20	300	125	1/3 of etch time

All etches performed at 50°C.

*Depends on cleanliness of chamber.

**For two 1.6x1.9cm^2 samples surrounded by 8 roughly 1cm^2 samples, InP etch rate was approximately 350~400 Å/min.

References:

[1] B. Liu, "Three-Dimensional Photonic Devices and Circuits," in *Electrical and Computer Engineering*. Santa Barbara: U. C. Santa Barbara, 2000.

Appendix E: Direct-Contact Wafer Bonding

The thorough sample cleaning is very important for good bond yields. Particles and films must be removed assiduously. Assembly of the samples is also performed very carefully, as uniform pressure is critical for good quality wafer bonds. Uneven fixture assembly can result in samples that are only bonded on one side.

There is no pattern alignment during bonding assembly: patterned samples are always bonded to blank, un-patterned samples. However, it is important that the samples' edges appear parallel to the naked eye because otherwise a poor facet cleave will result.

1. Cleave a blank, un-patterned sample to the same size as the patterned sample.
    a. If double-sided epitaxial layer processing is used, host sample should be commercially thinned ≤200-μm thick double-polished InP.
2. Make a very small, faint mark in corner of one sample with cleaving tool.
    a. If double-polished host substrate is used, mark its backside to be certain correct side is bonded.
    b. Do not make mark opposite any good devices.
3. Remove SiN from patterned sample with 1min CH_4 plasma for every 1000Å SiN.
4. Swab sample with an acetone-soaked synthetic q-tip for 1min and solvent clean with acetone and isopropanol.

5. Carefully inspect sample surfaces with microscope for particulate matter.
6. If particles are present, start over at 4.
7. 1-min oxygen plasma clean.
8. 25s NH_4OH dip.
9. 5 to 10min buffered HF dip.
10. Transport to bonding furnace in NH_4OH.
11. Transfer samples to crystal dish half-filled with methanol, assemble with 2 pairs of tweezers so desired surfaces are in contact and sample edges are aligned, and press down on center to drive out liquid between the samples.
12. Remove assembled samples to a cleanroom wipe, align so edges look as parallel as possible if slightly rotated. Press down on center with one pair of tweezers while holding with other pair, flip over, repeat on other side.
13. Inspect both sample sides for particles, remove with tweezers if necessary.
14. Assemble fixture:
    a. Blow off all fixture pieces with N_2, preferably before sample assembly steps.
    b. Place one drop methanol on fixture bottom surface for adherence, position silicon in center of fixture.
    c. Place one drop methanol on silicon, center samples on silicon.
    d. Center dome on top of silicon by hand, inspect fixture from side to check position.

    e. Position graphite fixture top, screw in screws until light resistance, adjust screws so fixture top is parallel to bottom when viewed from sides. Tighten screws with torque wrench, moving from screw to screw multiple times rotating wrench only partway each time to ensure evenness.

15. Load fixture into bonding furnace, evacuate to 1psi, fill with N_2 to 15psi, open exhaust fan such that glycerine bubbles at 1~2 bubbles/s.
16. Set furnace to 630ºC, return in 50min and set furnace to 0ºC, return when furnace temperature reads 400ºC (roughly 25min) and move furnace away from fixture.
17. Fixture and samples may be removed when the furnace temperature is less than 80ºC.

Appendix F: Miscellaneous processing

Sample Cleaving:

Samples are cleaved to be 1 to 3mm longer than the mask pattern. This is because most of the material 1 to 2 mm from the edge is severely damaged during the substrate removal wet etch step. After the initial nick, meticulously blowing off the top surface with N_2 before turning the sample over to make the cleave was found to be critical to avoid scratches from the small InP particles sprayed by the nicking. Even very small scratches had deleterious effects on the bond.

SiN Masking:

SiN is deposited immediately after each new epitaxial layer (or epitaxial layer side, in the case of double-sided epitaxial layer processing) because the semiconductor etches damage photoresist. This is also done to protect the top surface for wafer bonding. This initial layer of SiN is not removed from regions that come into contact during bonding until just before the bonding step. Avoidance of scratches or any other damage to these regions is critical, as tiny scratches lead to large un-bonded areas. Deposition is performed using a Plasma-Therm PECVD. 1000-Å layers of SiN are used because they are thick enough to withstand all etches and yet sufficiently transparent to view any lateral over-etching of material below.

SiN etching:

CF_4 plasma etching is used when the features are not so critical, as the plasma etcher occasionally leaves some polymer deposit on the sample that is very difficult to remove. The entire mask etch requires only a few minutes including pump-down time.

$SF_6/Ar/O_2$ reactive ion etching (RIE) leaves no polymer deposit on the sample, but due to the 20-min chamber pre-clean it is only used when it is critical that the SiN is etched cleanly. The $SF_6/Ar/O_2$ RIE SiN etch rate is roughly 330Å/min.

Sidelobe Suppression Trenches:

To avoid coupling of the guided mode to the slab mode of the slab waveguide above or below it, slab waveguide material is removed wherever the coupled waveguides are more than 10μm apart (Figure 1.5) [1].

Waveguide Facet Cleaving:

The waveguide facets are cleaved by hand. A 2-mm-long straight waveguide region for cleaving is included on the mask. Thinning the sample to 90μm before cleaving, and cleaving with a micrometer-stage-controlled setup was attempted, but the cleave showed no improvement.

Anti-Reflection (AR) Coating:

Anti-reflection (AR) coatings are performed on both facets to reduce losses and noise. SiO is deposited at 3~5Å/s at thicknesses varying from 2200 to 2500Å. The refractive index of SiO at this deposition rate is roughly 1.7. The reflectivity was less than 0.6% over 150nm. Calibration was performed with a Lamda-9 spectrophotometer. Though deposition at 30-50Å/s was found to produce a coating of superior index for AR purposes (0.1% reflectivity around 1550nm), a very non-uniform coating near the waveguides resulted, possibly from a reaction of the SiO with the SiN masking material that remained on the top surface of the device. Fixing undesirable coatings required a fresh cleave. Despite facet cleaning attempts with oxygen plasma and buffered HF, re-depositing SiO on a facet that appeared to have been cleaned of SiO always resulted in a very non-uniform coating.

References:

[1] B. Liu, "Three-Dimensional Photonic Devices and Circuits," in *Electrical and Computer Engineering*. Santa Barbara: U. C. Santa Barbara, 2000.

Appendix G: Mask Issues

On all masks, devices that deviated somewhat from those simulated were included in case the growth or simulations were undesirable. The 5 to 12 additional devices generally provided a range of 30% under-coupling to 30% over-coupling relative to the simulated ideal.

Support regions were placed 10μm away from all waveguides to ensure that neither deformation of the structure nor unwanted coupling to the supports would occur.

It was found that device inputs and outputs must be at least 20μm apart to avoid crosstalk above the background noise level of the measurements.

Waveguides with 7° facet tilts were used to reduce undesired reflections [1]. The slab waveguide removal regions are also tilted 7° at the end facing the device center to reduce undesired reflections of the slab mode [2].

A 2-mm-wide "frame" around the waveguide mask providing a solid bonded region with 5-μm wide vapor trenches forming a grid of 200-μm squares was found to reduce damage to the waveguides near the edges during substrate removal. The trenches are essential for allowing gaseous products to escape during the bond.

Other useful tricks to avoid sample damage through minimizing sample handling include align mark patterns that allow determination of which end of the sample is "up" without magnification and easily distinguishable marks for the post-bond IR-photolithography step.

References:

[1] D. Marcuse, "Reflection Loss of Laser Mode From Tilted End Mirror," *Journal of Lightwave Technology*, vol. 7, pp. 336-339, 1989.

[2] N. Dagli., Personal Communication, 2002.